A thesis entitled

THE MBE GROWTH AND ELECTRICAL CHARACTERISATION OF NARROW GAP III-V SEMICONDUCTORS

by

Ravindranath Droopad

Submitted to the University of London
for the degree of Doctor of Philosophy
and Diploma of Imperial College.

Solid State Experimental Group
The Blackett Laboratory
Imperial College
London SW7 2BZ

October 1989

ABSTRACT

This thesis describes the growth by molecular beam epitaxy and the electrical properties of narrow bandgap III-V semiconductors, namely InAs, InSb and InAsSb. Electrical characterisation is carried out mainly by low field Hall measurements and high field Shubnikov-de Haas experiments.

An investigation of RHEED intensity oscillations during the growth of InSb(001) is undertaken to determine the effects of varying the flux ratio and substrate temperature. This study reveals a comparatively narrow range of growth conditions under which RHEED oscillations can be observed. RHEED oscillations are used to optimise the growth conditions and facilitate the measurement of growth rates during the growth of InSb and its ternary alloy InAsSb. Consequently epilayers of InAs and InSb are grown with excellent surface morphology.

The initial stages of the heteroepitaxial growth of InSb on GaAs(001) are investigated using RHEED. The results suggest that growth initially occurs via InSb islands with sloping sides which then coalesce before a layer-by-layer growth mode has started.

The role of silicon as a possible n-type dopant in InSb is investigated by growing $\approx 1\mu m$ thick InSb layers which are slab-doped on GaAs substrates. The electrical data are analysed using a model for ionised impurity scattering modified for non-parabolicity and degeneracy. At low growth temperatures ($\approx 340^{\circ}C$) silicon acts predominantly as a donor and can produce electron concentrations up to $3 \times 10^{18} cm^{-3}$ with 77K mobilities identical to those found with bulk material. At higher growth temperatures ($\approx 420^{\circ}C$) silicon acts as an amphoteric dopant producing compensation ratios (N_A/N_D) as high as 0.5. By varying the position of the slab between the interface and the epilayer surface, it is shown that the interface between GaAs and InSb (lattice mismatch $\approx 14\%$) has only a small effect on the electrical properties of the epilayer provided the slab is located at a distance ≥ 0.3 μm from the heterointerface. Pronounced two-dimensional Shubnikov-de Haas effects are observed with the doping slabs and analysis of the oscillations indicates the occupation of at least seven subbands.

InAs layers of very high electrical quality are grown on GaAs. The Hall mobilities are found to decrease with decreasing thickness. This is shown to

be due to parallel conduction from a low mobility 2-dimensional electron gas either at the surface or the InAs-GaAs interface. $InAs_xSb_{1-x}$ epilayers are grown on GaAs substrates at a temperature of 370°C for a range of alloy compositions 0<x<1. The electrical data from these samples however, indicates higher than expected carrier concentrations and very low mobilities. Possible reasons for this degraded electrical quality are that the growth conditions are not optimised and alloying ordering effects are becoming significant.

Following the successful use of silicon as an n-type dopant in InSb, delta-doped structures and doping superlattices are grown. Quantum transport studies confirm the occupancies of multiple subbands for delta-doped layers in InSb. These results also suggest the presence of significant diffusion away from the dopant plane even at growth temperatures as low as 340°C.

CONTENTS

Abstract 2
Contents 4
List of Tables 7
CHAPTER 1 INTRODUCTION 8
CHAPTER 2 MOLECULAR BEAM EPITAXY 12
2.1 Introduction 12
2.2 Basic Concepts of MBE Growth 12
2.3 Theory of Epitaxial Growth 13
2.4 Kinetics in MBE Grown GaAs 15
2.5 Advantages of MBE 17
2.6 Homo- and Heteroepitaxy 17
2.7 Narrow Gap III-V Semiconductors Grown by MBE: A Literature survey 19
CHAPTER 3 A REVIEW OF RHEED AND RHEED INTENSITY OSCILLATIONS 25
3.1 Introduction 25
3.2 Fundamentals of RHEED 26
3.2.1 The Reciprocal Lattice 27
3.2.2 Diffraction from a 2-D Structure 28
3.3 Surface Reconstruction 29
3.4 Interpretation of RHEED Patterns 32
3.5 RHEED Intensity Oscillations 33
3.5.1 Nature of Diffraction Process 34
3.5.2 Origin of RHEED Intensity Oscillations 35
3.5.3 Applications of RHEED Intensity Oscillations 37
CHAPTER 4 MBE GROWTH EQUIPMENT AND PROCEDURES 39
4.1 System Configuration 39
4.2 The Deposition Chamber 39
4.2.1 Molecular Beams: Generation and Monitoring 41
4.2.2 Source Materials 43
4.2.3 The Substrate Holder 45
4.3 The Preparation Chamber 46
4.4 The Load Lock 47
4.5 Analytical Facilities 47
4.6 Pumping Arrangement 48
4.7 Attainment of UHV Conditions 49
4.8 Substrate Preparation 51

4.8.1 *Ex-situ* Cleaning 51
4.8.2 *In-situ* Cleaning 51
4.9 Calibration of Substrate Temperature 52
CHAPTER 5 THE GROWTH OF NARROW GAP SEMICONDUCTORS BY MBE 55
5.1 Introduction 55
5.2 Experimental 55
5.2.1 Flux Ratios and Calibration of Dopant Fluxes 56
5.2.2 Thickness Determination 57
5.2.3 Data Recording 58
5.3 RHEED Intensity Oscillations During the MBE Growth of InSb(001) 58
5.4 Layer Growth 61
5.4.1 InSb 61
5.4.2 Initial Stages of InSb/GaAs growth: A RHEED Study 62
5.4.3 InAs 66
5.4.4 InAsSb 67
CHAPTER 6 ELECTRICAL CHARACTERISATION OF SEMICONDUCTORS: THEORETICAL AND PRACTICAL CONSIDERATIONS 91
6.1 Introduction 91
6.2 Carrier Transport in Semiconductors 92
6.2.1 Derivation of the Conductivity Tensor 93
6.3 The Hall Effect 94
6.4 Magnetoresistance 96
6.5 Parallel Conduction 97
6.6 Scattering Mechanisms 98
6.6.1 Acoustic Phonon Scattering 99
6.6.2 Optical Phonon Scattering 100
6.6.3 Ionised Impurity Scattering 100
6.6.4 Dislocation Scattering 104
6.6.5 Alloy Scattering 105
6.7 Effect of Magnetic Field on Electrons in a Semiconductor 105
6.8 The Shubnikov-de Haas Effect 108
6.9 Experimental 111
CHAPTER 7 RESULTS AND DISCUSSION 113
7.1 Undoped InSb 113
7.2 Investigation of Silicon as an n-type Dopant in InSb 116
7.2.1 Hall Results for Samples Grown at Low Temperatures 116
7.2.2 Hall Results for Samples Grown over a Range of Temperatures 120

7.2.3 Low Field Magnetoresistance 123
7.2.4 The Shubnikov-de Haas Effect in Slab Doped and Homogeneously Doped InSb 125
7.3 P-type Doping in InSb 126
7.4 Electrical Properties of InAs Grown on GaAs 127
7.5 Hall Results of InAsSb 129
CHAPTER 8 DELTA DOPING AND DOPING SUPERLATTICES 142
8.1 Introduction 142
8.2 Some Basic Ideas on Delta Doping 143
8.3 Delta Doping Studies in InSb and InAs 145
8.4 Doping Superlattices 147
CHAPTER 9 CONCLUSIONS 156
Appendix A: List of Publications 159
Acknowledgements 160
References 161

LIST OF TABLES

Table 1.1 Some relevant band parameters and physical properties for InSb and InAs 9

Table 7.1 Electrical properties of undoped InSb epilayers 114

Table 7.2 Growth parameters and electrical properties of Si slab-doped InSb epilayers on GaAs 117

Table 7.3 Comparison between free carrier concentrations obtained from Shubnikov-de Haas measurements and low field Hall measurements 118

Table 7.4 Values of the transverse and longitudinal magnetoresistance for some Si slab-doped InSb/GaAs samples 124

Table 7.5 Hall mobilities and carrier concentrations of undoped and homogeneously doped InAs/GaAs samples 128

Table 7.6 Electrical properties, obtained from low field Hall measurements, for $InAs_xSb_{1-x}$ layers grown using a substrate temperature of $370^{\circ}C$ 129

Table 8.1 Growth parameters and electrical properties of delta doped InSb layers 146

CHAPTER 1 INTRODUCTION

A great deal of interest has been generated in narrow bandgap semiconductors because of their potential uses for infrared detectors and, as a direct result of their high mobilities, in high speed electronic devices [1-3]. Their small effective mass also makes them ideal for studying two-dimensional electron gas systems since quantisation can be observed for larger well widths as compared to large bandgap materials such as GaAs [4]. Although II-VI compound semiconductors such as HgCdTe are well established as important intrinsic semiconductor systems for infrared detectors there are inherent problems in material stability [5,6]. New technologies such as infrared imaging have increased the demand for high quality and uniform materials which would operate over long periods of time. Consequently III-V narrow bandgap compound semiconductors have, in recent years, received increasing attention as potential applications for the next generation of infrared detectors and very low loss optical fibre communication systems [7,8].

InSb has the smallest bandgap of the III-V binary semiconductors. It is a direct gap material with the minimum of the conduction band situated at the centre of the Brillouin zone. Near this minimum, the energy-wavevector relation is isotropic but, as shown by Kane [9] in his famous paper of 1957, E(k) differs from that of the simplest parabolic relation $E = \hbar^2k^2/2m^*$. As a result of this non-parabolic nature of the conduction band, the effective mass of the electrons depends strongly on the electron concentration. The valence band shows the structure common to all zincblende semiconductors, i.e. two bands degenerate at the valence band maximum and one spin orbit split band [10]. InAs is also a direct gap semiconductor having a band structure which closely resembles that of InSb. The energy gap of InAs is larger than that of InSb but the spin orbit splitting of the valence band is smaller. Near the conduction band minimum E(k) is also isotropic and non-parabolic. Figure 1.1 shows a schematic band structure representative of both InSb and InAs and table 1.1 lists some relevant band parameters and physical properties [11].

Warm or hot objects emit a substantial amount of infrared energy with wavelengths up to 12μm. At ambient temperature however, the emitted radiation is in the spectral region above 3μm. The atmosphere transmits poorly in the infrared with the exception of the 3-5μm medium-wave and the

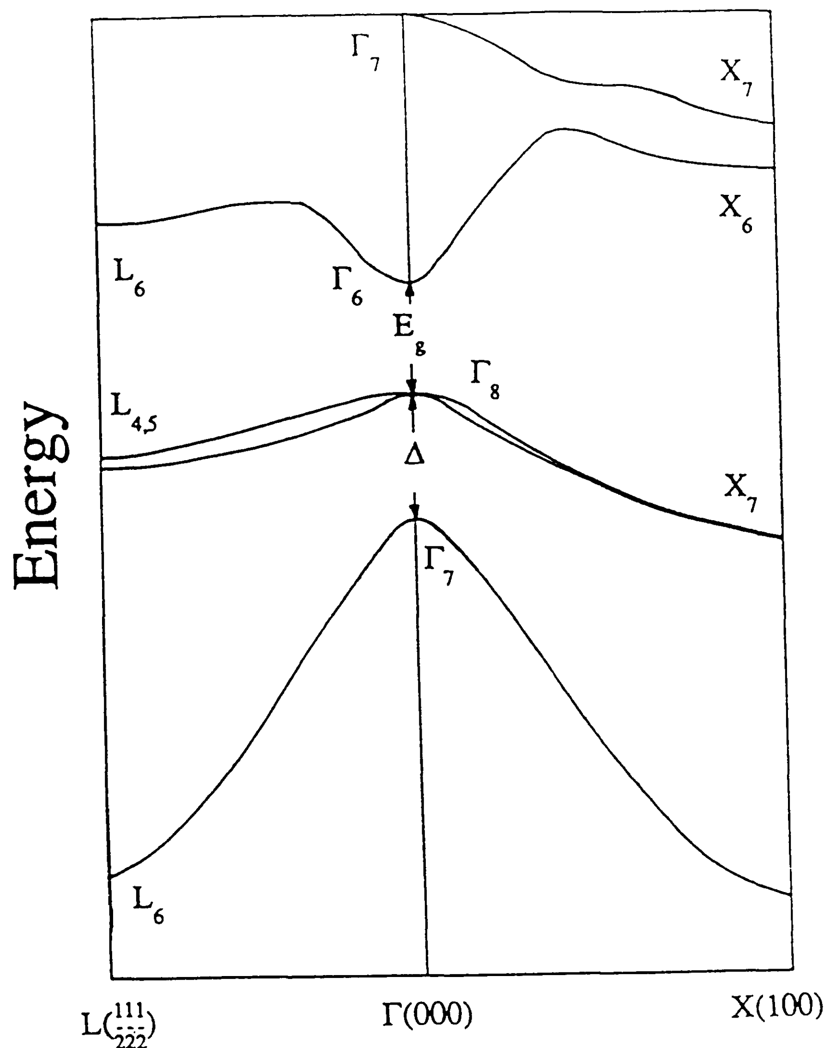

Figure 1.1 Schematic representation of the band structure for InAs and InSb.

	InAs	InSb
Lattice Parameter, a_o(Å)	6.058	6.479
Energy Gap, E_g(eV) -300K	0.354	0.18
- 77K	0.414	0.23
Spin Orbit Splitting, Δ(eV)	0.41	0.98
Effective Mass at the bottom of Conduction Band, (m^*/m_o)	0.027	0.0145
Dielectric Constant ε(0)	15.15	16.8
ε(∞)	12.25	15.68
Melting Point (°C)	942	527

Table 1.1 Some revelant band parameters and physical properties for InAs and InSb.

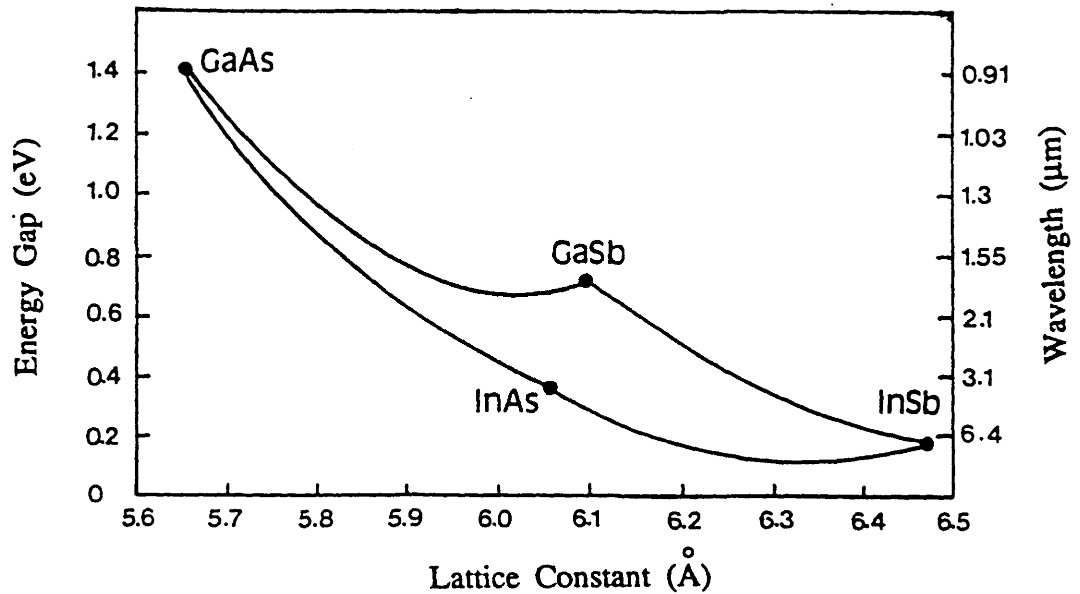

Figure 1.2 Lattice parameters, energy gaps and the corresponding wavelengths for InAs, InSb and In(AsSb) together with those for GaAs and GaSb

8-12μm long-wave infrared regions. Because of their small bandgap InAs, InSb and InAsSb are potentially capable of operating in these spectral regions. Figure 1.2 shows the lattice constants, energy gaps and corresponding wavelengths of InAs, InSb and their alloy InAsSb, together with those of GaAs and GaSb which are used as substrates in this study. InAs can be used for operating at wavelengths around 3.5μm whereas InSb can operate at wavelengths around 6μm. In addition, the alloy $InAs_xSb_{1-x}$ with a composition x = 0.4 and an energy gap of 0.136eV [12] can operate in the long wavelength region out to 9μm at 77K which represents the smallest bandgap of the III-V semiconductor alloys. By growing these materials on GaSb substrates a lower operating wavelength limit of ~2.0μm can be achieved. Strained-layer superlattices (SLS) involving InAsSb [12] and doping superlattices [13] can be potentially useful as detectors operating in the longer wavelength 8-12μm 'atmospheric window'.

The work described in this thesis is concerned with the growth and electrical characterisation of InAs, InSb and their alloy, InAsSb. Growth is

carried out by molecular beam epitaxy (MBE) and electrical characterisation utilises low field Hall measurement, magnetoresistance and Shubnikov-de Haas techniques.

A brief description of the MBE growth process together with a review of the existing literature on the growth and electrical properties of narrow gap III-V semiconductors is given in chapter 2. Chapter 3 describes the reflection high energy electron diffraction (RHEED) and the RHEED intensity oscillation techniques. RHEED has proven to be the most useful diagnostic equipment to be incorporated into MBE systems. It allows for the continuous monitoring of the semiconductor surface throughout the growth sequence. The variation of the intensity of the RHEED features provides information on the growth dynamics and enables the growth parameters to be optimised.

In chapter 4 the growth equipment and some of the routine procedures adopted in the preparation for layer growth are described. Chapter 5 presents a summary of the results on RHEED intensity oscillations which, during this study, were observed for the first time during InSb growth. The results of a RHEED study on the initial stages of the heteroepitaxial growth of InSb on GaAs are also presented. In addition, the surface morphology of the layer grown will briefly be discussed in terms of the growth conditions.

The range of techniques used for the electrical characterisation are reviewed in chapter 6 and the experimental results on InAs, InSb and InAsSb for the complete range of alloy composition are presented and discussed in the following chapter. In particular, the use of silicon as an n-type dopant in InSb is investigated.

Chapter 8 describes the growth and presents some of the results on some other structures grown during the course of this study. These include delta doped and doping superlattices. Finally chapter 9 summarises the results and the conclusions drawn from this study.

CHAPTER 2 MOLECULAR BEAM EPITAXY

2.1 Introduction

Molecular Beam Epitaxy (MBE) evolved from the work of Günther during the 1950s in which he used a "three temperature" method to grow polycrystalline, but stoichiometric films of InAs and InSb on glass substrates [14]. In his "three temperature" method he used a group V source kept at a temperature T_1, a source of the group III-V material kept at a higher temperature T_3, and a substrate held at an intermediate temperature T_2. However, it was not until a decade later that Davey and Pankey demonstrated the epitaxial growth of single crystal GaAs using Günther's method [15]. At the same time Arthur was investigating the surface kinetics of the interaction of Ga and As_2 beams with GaAs substrates which provided the basis for the understanding of the growth mechanism [16]. In the 1960s, Joyce and co-workers used a molecular beam system to investigate the nucleation of homoepitaxial Si films produced by the pyrolysis of SiH_4 [17]. They also studied the influence of the substrate surface on nucleation and the subsequent behaviour of layer growth. These investigations led to the development of MBE as a practical thin film growth technique when Cho applied a similar technique to grow thin films for device purposes [18-20].

2.2 Basic Concepts of MBE Growth

MBE is an evaporation technique which can be used to grow thin films of high quality single crystal semiconductors. In this technique neutral atomic and molecular beams, generated thermally from heated Knudsen cells are directed onto a heated substrate under ultra high vacuum (UHV) conditions. UHV conditions are essential to minimise the incorporation of impurities during growth.

During the growth of III-V compound semiconductors, the substrate is maintained at a high temperature so that in the absence of the group III flux, no group V molecules stick onto the surface, i.e an equilibrium is established whereby the number of group V molecules incident on the surface is equal to the number leaving. However, the temperature is usually low enough to ensure that virtually all the impinging group III atoms stick to the growing surface. It should however be noted that above a certain temperature, III-V compounds are temperature unstable in that the group V

species is preferentially desorbed and, at even higher temperatures, the group III element tends to evaporate more readily. Therefore, for stoichiometric growth at substrate temperatures normally used for III-V semiconductors the group V molecules are supplied in excess. Typical growth rate used in MBE is one monolayer per second which corresponds to around one micron per hour.

During growth, the free group III atoms react with the incident group V molecules to form III-V compound molecules which are then incorporated into the growing lattice. Any unreacted group V molecules rapidly desorb and hence do not accumulate on the surface. Although MBE is capable of producing single crystal material at low growth temperatures [21,22], it is clear from Hall measurements and photoluminescence spectroscopy that most III-V compound semiconductor grown at such low temperature using growth rates of around 1 μm/hr are severely degraded. For example, if GaAs is grown at 480 °C it is highly resistive and gives little, if any, near-band-edge photoluminescent intensity [23-25]. However, it was shown that by reducing the growth rate, GaAs with improved electrical properties could be grown at temperatures as low as 380 °C [26]. It was suggested that this reduced growth rate results in a reduction of the concentration of defects by allowing adsorbed Ga and As atoms sufficient time to reach the appropriate lattice sites before incorporation into the growing film. Low growth temperature is also necessary for delta doping in GaAs as this reduces the amount of diffusion of the dopant atoms away from the doping plane [27]. Consequently the need to produce device quality III-V semiconductors without the need for very low growth rates has resulted in the use of high growth temperatures.

2.3 Theory of Epitaxial Growth

The various theories used to investigate crystal growth have mostly been based on statistical thermodynamics and kinetic rate equations [28,29] which have been successfully employed to the understanding of equilibrium phase diagrams for growth from solutions and vapour phase. These and other experimental studies [30,31] on epitaxial growth have established three distinguishable growth modes:-

(i) Layer-by-layer growth through two-dimensional nucleation. The deposited atoms or molecules are more strongly bonded to the substrate and so nucleation takes place to form monolayer islands. These islands grow to form a complete continuous monolayer. Subsequent layer growth

takes place in a similar way with nucleation taking place on each completed monolayer to form islands.

(ii) Volmer-Weber mode in which the deposited atoms are more tightly bonded between themselves than to the substrate atoms. In this case, nucleation takes place in the form of discrete three-dimensional islands on the substrate surface. These islands increase in number and size until they merge to form a continuous film.

(iii) Stranski-Krastanov mode: in this growth mode a finite number of monolayers are produced by two-dimensional nucleation as in (i). Subsequent growth occurs by the three-dimensional nucleation of critical size clusters as in (ii).

A fourth growth mode where growth proceeds at steps and kinks on the surface was suggested by Burton, Cabrera and Frank [32]. These steps and kinks are due to thermodynamic fluctuations at high temperatures and thus the need for nucleation is avoided.

During MBE growth it has generally been assumed that various kinetic barriers prevent thermodynamic equilibrium from being achieved. It should be noted that the temperature of the substrate is usually different from the temperatures of the incident beams. However, the substrate temperature and the incident beam fluxes are such that there is a large overpotential for growth, i.e. the rate of incorporation is faster than the rate of evaporation.

Madhukar [33] applied Monte Carlo simulation methods with relevant kinetic (sticking coefficient, surface migration rate and evaporation rate) and growth parameters to study epitaxial growth under conditions which were far from equilibrium such as in MBE. In his model a clear distinction was made between the equilibrium of the entire system, the partial equilibrium between the substrate and the growing film and the local thermodynamic equilibrium between the substrate and growing film. Heckingbottom *et al* [34] examined experimental results on the growth and doping of GaAs in order to identify specific kinetic barriers to reaction rate. They came to the conclusion that during growth any such barriers have very little effect, otherwise crystal perfection of materials and abrupt interfaces could not be consistently achieved by MBE. Singh and Bajaj [35,36] developed a very similar model for the growth of III-V compound semiconductors, also based on Monte Carlo simulation and demonstrated that the group III surface migration rate is the most important parameter in determining the smoothness of the

growing surface. To take account of surface molecular reactions, Madhukar and co-workers developed their Configuration Dependent Reactive Incorporation (CDRI) growth process, [37,38]. It was suggested that for low rates of dissociation of the As_2 molecule in its precursor physisorbed state the CDRI growth process leads to a Reaction Limited Incorporation (RLI) growth mechanism in which clusters of two or more Ga atoms are required before layer growth can proceed. For fast dissociative reaction kinetics a Configuration Limited Reactive Incorporation (CLRI) growth mechanism was postulated in which the arsenic incorporation rate can be limited by the availability of appropriate Ga configurations. It was also shown that both led to a layer-by-layer growth mode with an oscillatory growth rate behaviour.

Clarke and Vvedensky recently examined the kinetics of MBE growth, using Monte Carlo simulations, by calculating the evolution of the surface step density [39]. Their model has shown a remarkable correspondence between the evolution of the step density and the measured RHEED intensities for the specular spot during the growth of III-V semiconductors. The success of their model has opened up the possibility of using such theoretical models as computer-aided design tools. This would allow the growth of a new material to be simulated to determine the optimum growth conditions for high quality material.

2.4 Kinetics in MBE grown GaAs

Of the III-V compound semiconductors grown by MBE, GaAs has received the most attention. The reaction kinetics involved in the growth of GaAs(001) were studied extensively by Foxon and co-workers [40,41] using modulated beam mass spectroscopy (MBMS) for incident beams of Ga with either As_2 or As_4. In this technique, the molecular beams either arriving at or leaving the sample surface are modulated mechanically to eliminate any signals due to the background gases in the growth chamber. Figure 2.1 illustrates the principle of this technique and the information that can be obtained. From these studies models of the growth chemistry of GaAs were proposed. Figure 2.2 shows the model for a source of As_4. The basic feature of this model for the growth of GaAs is that the arsenic tetramers are first adsorbed into a mobile precursor state. In this state they can migrate over the surface and may be desorbed, but some As_4 molecules are chemisorbed onto adjacent Ga atoms when such pairs are available. The dissociation mechanism involves two

Principle of modulated molecular beam measurements

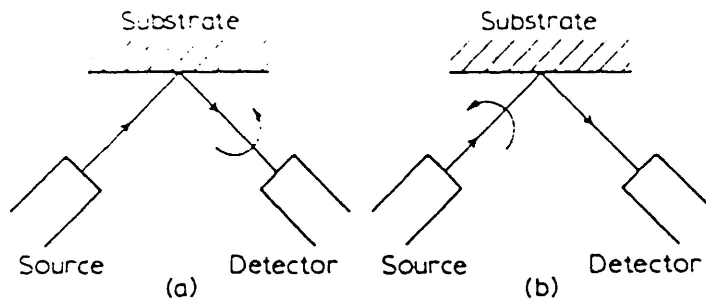

(a) { Identification of desorbed species
Desorption rate
Sticking coefficients
Orders of chemical reactions
Thermal accommodation coefficients }
Surface lifetimes
Binding energies } (b)

Figure 2.1 The principle of the MBMS technique used in the study of growth kinetics. Also shown are some of the information that can be obtained from such a study. (Reproduced with kind permission of B.A.Joyce.)

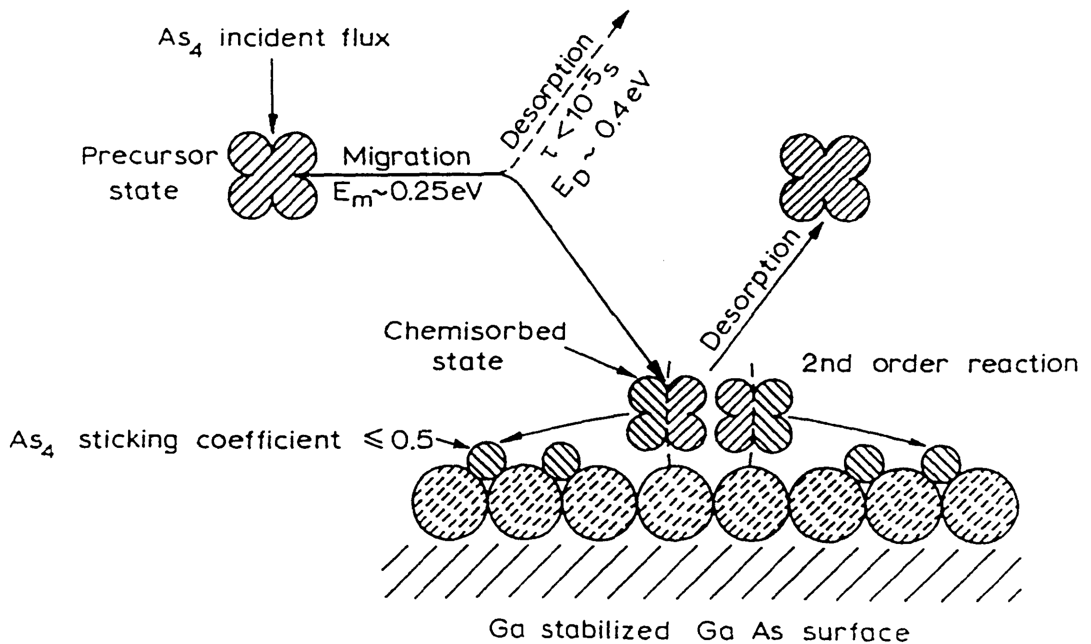

Figure 2.2 Model for the growth of GaAs(001) using a source of arsenic tetramers. (Reproduced with kind permission of B.A.Joyce)

tetramers, with two As atoms from each tetramer incorporated into the growing lattice and the remaining two re-combining and desorbing as an As_4 molecule. In this model the sticking coefficient of As_4 can never exceed 0.5 even under Ga rich conditions which agrees with experimental results.

2.5 Advantages of MBE

One of the most significant advantages of MBE is the ability to incorporate UHV-associated surface analytical equipment directly into the growth and the preparation chambers. Such equipment allows both the chemical and structural properties of the epilayers to be monitored throughout the growth process. They also aid in the optimisation of growth conditions and possible trouble-shooting.

The growth rates in MBE are generally low: around 1 $\mu m h^{-1}$ i.e. ~1 monolayer per second. By using simple mechanical shutters which operate in times much less than one second, control of changes in the doping levels and alloy composition can be achieved to within atomic dimensions. The directionality of the incident beams also allows geometrical control of material structures in three dimensions by the use of simple mechanical masks. Finally since MBE is a non-thermal equilibrium growth technique, the growth of metastable alloys is possible.

2.6 Homo- and Heteroepitaxy

Epitaxy occurs when there is a well defined orientation relationship between the epilayer and the substrate material. The term homoepitaxy refers to the growth of one material onto itself, e.g. an InSb epilayer on an InSb(001) substrate. Heteroepitaxy on the other hand is used to describe the growth of one material onto a substrate of different material, e.g. InSb on GaAs(001).

A critical factor in both homo- and heteroepitaxial growth is the quality of the substrate. During homoepitaxial growth when the surface is free from contamination, growth usually proceeds via a two-dimensional step mechanism. As a result of polishing and *ex-situ* etching the surface of the substrate may consist of 3-D roughness indicated by a spotty RHEED pattern. However, the effects of these are usually minimised by growing a buffer layer of approximately 1/2 μm.

In some cases homoepitaxial growth is not ideal for narrow gap semiconductors, such as those on which this study is based, because these narrow bandgap semiconductors have no semi-insulating form. Consequently any investigation of the electrical properties of, for example InSb epilayers grown on InSb requires the removal of the substrate. Electrical isolation between epilayer and substrate can be achieved using wider bandgap semiconductors as substrates. Such heteroepitaxial systems typically have a lattice mismatch defined as:

$$\text{Lattice Mismatch} = (a_{epi}-a_{sub}/\ a_{sub})\text{x}100\% \qquad (2.1)$$

where a_{epi} and a_{sub} are the lattice parameters of the epilayer and substrate respectively. In this study InSb and InAs are grown heteroepitaxially on GaAs which is available in a semi-insulating form ($\rho > 10^7$ ohm cm). These systems have a lattice mismatch of 14.6% and 7.4% respectively at room temperature. In addition to electrical isolation the use of GaAs substrates opens up the possibility of the fabrication of single chip opto-electronic devices.

At the interface between two lattice mismatched semiconductors the lattice mismatch may be accommodated by the generation of a high density of misfit dislocations. If the lattice mismatch between the substrate and epilayer is small the epilayer will be elastically strained and coherent growth occurs. In this case the interfacial energy is reduced at the expense of strain energy in the film. In an extension of this type of growth Jesser and Matthews [42] demonstrated the pseudomorphic growth of the γ-phase of iron onto the (001) surface of copper at room temperature although this phase of iron is thermodynamically unstable at temperatures below 916°C. Another example of pseudomorphic growth is α-Sn on InSb(001) having a lattice mismatch of about 0.1% [43]. These films grown coherently are metastable phases for which the elastic strain in the film is such that the sum of the interfacial energy and the elastic energy stored in the film is a minimum. Above a certain critical thickness the epilayer lattice relaxes and releases its energy to generate misfit dislocations which tend to propagate through the growing layer. However, there are cases when initial growth proceeds via the nucleation and growth of islands [44,45]. This may be due to the critical thickness being less than a monolayer. It will be shown in chapter 5 that this is the case for the growth of InSb on GaAs, but from the results of transmission electron microscopy (TEM) island growth ceases at a

thickness of around 1000Å [46]. There are three possible ways of reducing the effects of lattice mismatch. These are:-

(a) The growth of a buffer layer whose lattice constant is the average of the substrate and the epilayer.

(b) The growth of a compositionally graded buffer in which the composition and hence the lattice parameter is varied progressively from that of the substrate to the epilayer.

(c) The growth of short period strained layer superlattices.

It has been shown that strained-layer superlattices with layer thicknesses less than a critical value have led to substantial improvements in the defect density of the epilayers as compared to compositionally graded buffer layers [47].

In some heteroepitaxial systems lattice match can be achieved by suitable choice of substrates. An example of this is the growth of $InAs_{0.91}Sb_{0.09}$ on GaSb.

2.7 Narrow gap III-V semiconductors grown by MBE: A Literature Survey

In this section an overview is presented on the work that has appeared in the literature concerning the growth of InSb, InAs, and InAsSb.

The first report of the molecular beam growth of InSb was attributed to Baba *et al* [48] who used a two-source molecular beam technique to grow stoichiometric InSb films on fused quartz substrates, despite the limited volatility of antimony. These polycrystalline films were grown at substrate temperatures in the range of about $225^{\circ}C$ to $425^{\circ}C$ and examination by Auger Electron Spectroscopy suggested that the relative flux intensity of the group V species to the group III atoms was critical for the growth of stoichiometric InSb compounds. This work was followed by the heteroepitaxial growth of InSb on GaAs(001) substrates by Yano *et al* [49,50] who were able to produce single crystal films with fairly flat surfaces in spite of the large lattice mismatch between the substrate and epilayer. They found that the films were generally n-type but the layer within about 1.5 μm from the interface had poor crystalline properties. However, the work presented in this thesis suggests that the electrical properties of InSb layers approach bulk values at a distances $\geq 0.35\mu m$ from the InSb-GaAs interface when Si doping is used.

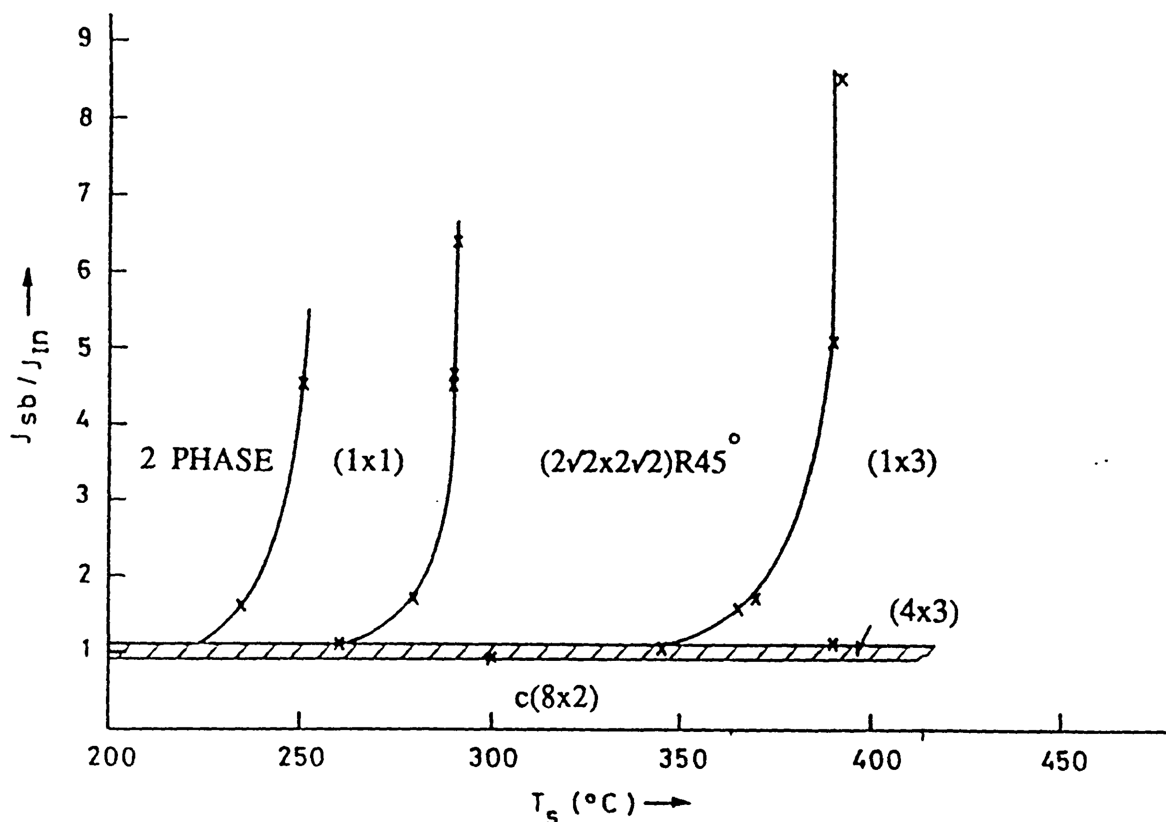

Figure 2.3 Surface phase diagram for InSb showing the various reconstructions as a function of flux ratio and growth temperature. (After ref. 59: Note these authors claimed the (2√2x2√2)R45° to be a (√2x√2))

Detailed RHEED studies were later carried out on InSb films both during homoepitaxial [51,52] and heteroepitaxial [52] growth. The results of these studies are presented in the so-called surface phase diagram of figure 2.3 which shows the various surface reconstructions in terms of the incident flux ratios and substrate temperatures. Such diagrams are extremely useful since they can be used as a guide for ensuring the reproducibility of growth conditions during MBE growth. During their work Noreika and co-workers [52,53] also reported that the heteroepitaxial growth of InSb on GaAs proceeded by a three-dimensional stage followed by facetted two-dimensional growth. Further growth produced surface reconstructions identical to those observed during homoepitaxial growth.

Later work included an investigation of the electrical properties of both

undoped homoepitaxial and heteroepitaxial InSb films [53-56] and the structural properties of the InSb/GaAs layers. In addition, beryllium was successfully used as a p-type dopant in InSb [53,54]. As will be shown in chapter 7 a study of silicon as an n-type dopant in InSb revealed an amphoteric behaviour for high growth temperatures. Nevertheless, by controlling the growth conditions it was demonstrated that doping densities up to $3x10^{18}cm^{-3}$ with virtually no compensation can be achieved. An investigation of the heteroepitaxial growth of InSb on CdTe substrates [57,58] and the growth of CdTe-InSb multilayer structures [59] on InSb(001) was also undertaken. More recently MBE growth of InSb was demonstrated on Si substrates despite the large lattice mismatch (19%) at room temperature between these two materials [60]. However, no values for the defect densities of such system were reported. The motivation for the growth of InSb on Si lies in the possibility of integration with high-speed circuits by the advancing GaAs on Si technology and the use of the highly developed integrated circuit technology based on Si.

Godinho *et al* [61] were the first to use the "three temperature" vacuum deposition technique to study thin films of single crystal InAs. They found that the electrical properties of these films were comparable to those grown by liquid phase epitaxy and vapour phase epitaxy. A few years later Tateishi and co-workers demonstrated that InAs films could be grown epitaxially on GaAs substrates and that the unintentionally doped films were n-type [62]. Yano *et al* then evaluated thin crystalline InAs films grown heteroepitaxially on GaAs using optical microscopy, SEM, RHEED and electrical measurements [63]. They found that layers with good morphological and crystalline properties could be grown, in spite of the large lattice mismatch (7.4%), but the electrical properties of the layers depended on the substrate temperature used during growth. They also demonstrated the successful use of Mg as a p-type dopant. Similar results were reported by Meggit *et al* [64].

Electrical and cross-sectional TEM studies of InAs/GaAs films have shown that the dislocation density at the InAs-GaAs interface is several orders of magnitude higher than in the bulk films, about $3x10^{8}cm^{-2}$ for a 2μm thick InAs layer [65,66]. The nucleation and strain at the interface of the InAs/GaAs heterostructure was investigated by Schaffer *et al* [67] and more recently by Newstead and co-workers [68] and Houzay and co-workers [69]. Growth proceeds via a Stranski-Krastanov mode in which the first few

monolayers are strained and homogeneous, followed by island formation and coalescence. As the thickness of the InAs layer increases the lattice mismatch is accommodated by the generation of dislocations. As a result of the extensive RHEED studies during MBE growth, a surface phase diagram for InAs(001), shown in figure 2.4 was constructed showing the various surface reconstructions.

Detailed investigations have shown that the surface morphology and electrical properties of InAs were critically dependent on the growth parameters [70,71]. In addition, the mobility and carrier concentration were found to decrease and increase respectively as the thickness of the layer was reduced, indicating that the interface was contributing to the electrical properties. Grange *et al* [71] established that the electrical properties of

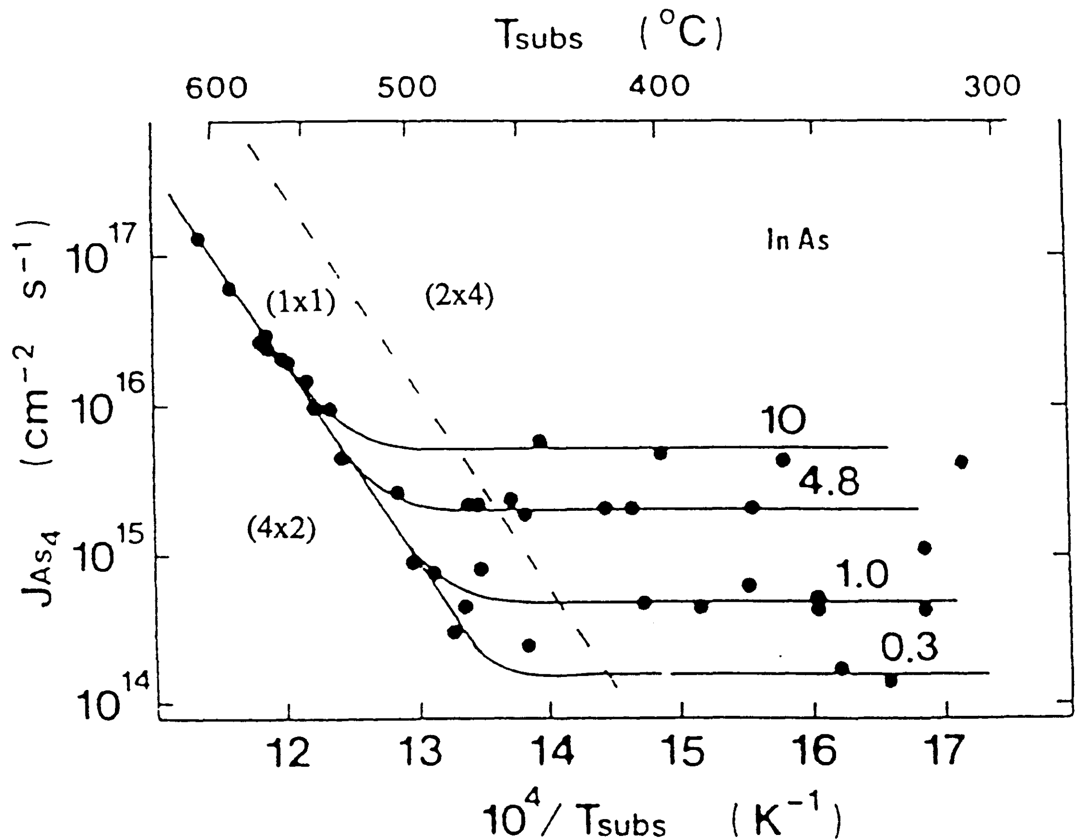

Figure 2.4 Phase diagram for InAs showing the surface reconstructions as a function of arsenic flux, growth rate and temperature. (After ref 68)

thin undoped InAs layers could be described by assuming that an accumulated interfacial region exists with degraded mobility. Chang *et al* [65] and Kalem *et al* [75] attributed the reduction in mobility with decreasing thickness to the dominance of dislocation scattering at the interface. However, it was shown that a degenerate surface accumulation layer is present on vapour phase epitaxial InAs layers and that the transport properties of this surface region become dominant in determining the electrical properties of thin layers [72]. Magneto-optical studies on InAs samples grown during this study revealed the existence of a low mobility accumulation layer together with a bulk region having mobilities of the order 250,000 $cm^2V^{-1}s^{-1}$ [73]. Recently steps were taken to improve the interfacial region by growing a step-graded and a strained-layer superlattice (SLS) buffer [74]. It was shown that a 5 period $In_{0.8}Ga_{0.2}As$/ GaAs SLS led to a reduction of the defect density, to about 10^6 cm^{-2} in a 5μm thick sample. However, the electrical properties of these epilayers were only slightly improved. The same group has also demonstrated the growth of InAs layers on Si substrates [75].

InAsSb has the smallest bandgap among the III-V semiconductor alloys and as such it has enormous potential for infrared detectors. The prediction by Osbourn [12] that the bandgap can be further reduced by the use of tensile strain in strained-layer superlattice (SLS) has attracted considerable interest in this material system. The first report of the MBE growth of InAsSb was concerned primarily with a RHEED and surface morphology study of InAsSb lattice matched to GaSb [76]. This was followed by the growth of $InAs_xSb_{1-x}$ on GaAs and InSb substrates for $0<x<1$ [77] and the growth of InAsSb SLS [77,78]. Although TEM studies on a 200Å $InAs_{0.4}Sb_{0.6}$/200Å $InAs_{0.2}Sb_{0.8}$ SLS revealed the existence of abrupt, planar interfaces there were threading dislocations in the superlattice region which were shown to be due to the large density of dislocations at the substrate/buffer, i.e. InSb/$InAs_{0.3}Sb_{0.7}$ interface. These early work suggested that the composition of these alloys was dependent on the substrate temperature and the antimony flux used during growth. Recently however, it was shown that the composition of $InAs_xSb_{1-x}$ epilayers grown on GaAs(001) substrates was relatively independent of substrate temperature provided dimeric, instead of tetrameric group V sources are used [79]. The fact that antimony was incorporated preferentially to arsenic was useful in determining the the crystal composition, from the Sb_4/In flux ratio.

Since 1986 there has been a spate of publications on InAsSb mainly from the groups at Bell Labs. Chiu *et al* [80] demonstrated the growth of lattice matched InAsSb on GaSb and found that undoped $InAs_{0.91}Sb_{0.09}$ epilayers were n-type with a room temperature carrier concentration on the order of ~$5x10^{16}$ cm^{-3}. P-type doping was achieved using Be. The growth of $InAs_xSb_{1-x}$ grown on InAs(001) substrates was investigated by Yen and co-workers [81,82] who successfully grew epilayers over the complete compositional range of $0<x<1$. Bandgap measurements using optical absorption produced cut-off wavelengths as long as 12.5 μm. In addition, photoluminescence peaks having wavelengths as long as 8 μm have been obtained.

The dislocation density of InAsSb grown on GaAs was found to increase with x, having values of $1x10^7$ cm^{-2} for x=0 and $2.7x10^7$ cm^{-2} for x=39% [83] although it is open to debate whether this represents a significant difference. It was also shown that the background carrier concentration increased with x for values $0<x<\sim0.5$ and the room temperature mobilities decreased with increasing As content suggesting that InSb has the highest mobility among the III-V compound semiconductor materials. Bethea *et al* [84] fabricated and characterised a photodetector using $InAs_{0.02}Sb_{0.98}$ grown on GaAs and achieved an internal quantum efficiency of 47% with a response time of less than 10ns at λ = 5.4 μm. The detector had a cut-off wavelength of 6.4 μm. These workers also fabricated a photoconducting detector using $InAs_{0.22}Sb_{0.78}$ on GaAs [85]. Although this material showed promise as a photodetector operating in the 10 μm spectral region, the photoconductance lifetime was found to be nearly two orders of magnitude less than that determined for the $InAs_{0.02}Sb_{0.98}$/GaAs sample.

Recently the group from Sandia demonstrated the first strained-layer InAsSb superlattice photodiode [86]. Their structure consisted of a p-n junction embedded in an $InAs_{0.09}Sb_{0.91}$/InSb SLS with equal 130Å thick layers. The photodiode cut-off wavelength extended to beyond 8 μm at 77K and the detectivity was found to be within one order of magnitude of the well established HgCdTe detectors at 7 μm. Later these workers showed that InAsSb SLS's have type II band offsets, for alloy composition <40% As and demonstrated that large photoconductive gain can be observed in photodetectors constructed from these SLS's [87].

CHAPTER 3 A REVIEW OF RHEED AND RHEED INTENSITY OSCILLATIONS

3.1 Introduction

The first application of electron diffraction dates back to 1927 with the classical experiment of Davisson and Germer [88] who obtained diffraction of low energy electrons (30-600eV) from the surface of a nickel crystal. This confirmed the wave-particle nature of electrons as postulated by de Broglie in 1924 [89] and led to the development of the low energy electron diffraction (LEED) technique about 30 years later. In this technique the electron beam is directed at normal incidence to the surface of the crystal. Because of the high atomic scattering cross-sections LEED is extremely sensitive to surface atomic arrangements. The delay between the original experiment in 1927 and the development of LEED was mainly due to the technical difficulties in attaining vacuum better than 10^{-8} torr necessary for the LEED technique since residual gas can quickly be adsorbed on to the crystal surface causing significant errors.

Reflection high energy diffraction (RHEED) was first demonstrated by Nishikawa and Kikuchi [90] in 1928 when diffraction was obtained from the surface of a calcite crystal using a beam of high energy electrons at grazing incidence. In RHEED the energy of the electrons is usually between 10 and 100 keV resulting in large elastic mean free paths [91]. But, because grazing incidence and emergence are used this technique is particularly surface sensitive since the penetration of the electron beam perpendicular to the surface is small. As a consequence of this forward scattering geometry and its surface sensitivity RHEED has become a standard diagnostic technique with the introduction of the molecular beam epitaxial growth process. This was demonstrated very successfully by Cho [18] who found that the surface reconstructions of GaAs could easily be monitored during MBE growth.

This chapter presents a review of this important technique and shows how the diffraction patterns obtained can yield useful information about surface morphology and topography. It will also be shown that the intensity of the features within the diffraction patterns can provide information on growth rates and to study growth dynamics.

3.2 Fundamentals of RHEED

In this technique a beam of high energy electrons is directed at the surface of a crystalline specimen at grazing incidence. The diffraction pattern formed will be characteristic of the surface atomic structure since the incident electron momentum normal to the surface is very small. A typical RHEED system is shown in figure 3.1. Usually the angle of incidence of the electron beam is between 1-3°. The diffraction patterns are observed on a fluorescent screen from where they can be recorded.

Electron diffraction can be understood by using the postulation of de Broglie that electrons can exhibit wave-like properties. The wavelength

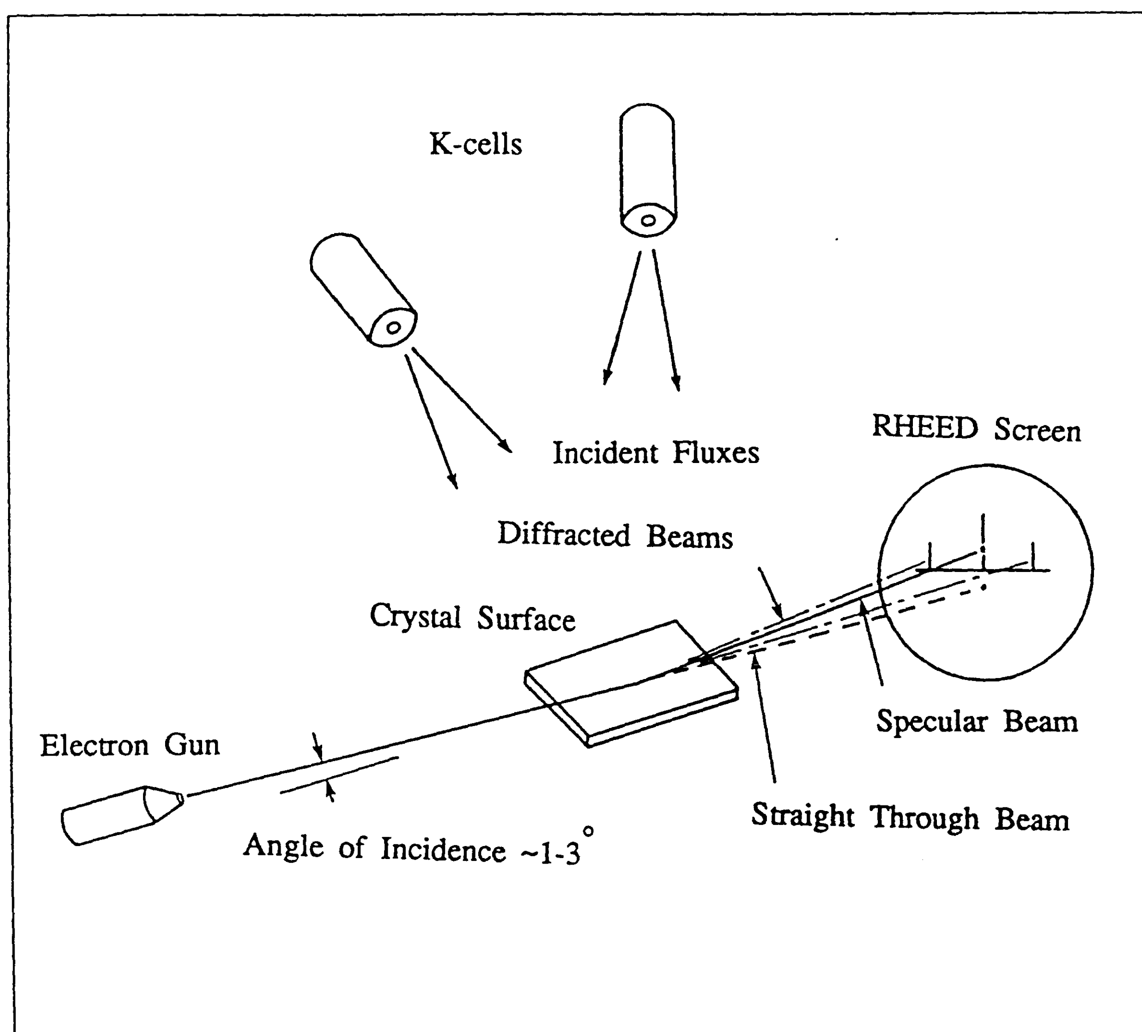

Figure 3.1 Schematic illustration of a RHEED system.

associated with electrons having energy E (in eV) is given by:

$$\lambda = \frac{h}{\sqrt{[2m_o eE(1+eE/(2m_o c^2)]}} \qquad (3.1)$$

where m_o is the electron rest mass, h is Planck's constant and c is the speed of light. This implies that the wavelengths associated with electrons used in RHEED varies from 0.04Å to 0.12Å. Therefore the electron beams are sensitive to atomic positions. An understanding of RHEED is greatly facilitated with the help of the reciprocal lattice.

3.2.1 The Reciprocal Lattice

The reciprocal lattice plays a fundamental role in the analysis of diffraction from periodic structures. It is a representation of the spatial properties of a crystal in Fourier space just as a quantity which varies with time can be represented in the frequency domain. For a perfect 3-dimensional crystal the reciprocal lattice in Fourier space is an infinite periodic 3-D array of points whose spacings are inversely proportional to the distances between planes in the direct lattice.

Let $\mathbf{a_1}$, $\mathbf{a_2}$, $\mathbf{a_3}$ represent the primitive vectors of the crystal in free space. Any vector that describes the set of points that make up this lattice can be written as:

$$\mathbf{R} = p\mathbf{a_1} + q\mathbf{a_2} + r\mathbf{a_3} \qquad (3.2)$$

with p, q and r being integers. The primitive vectors that define the reciprocal lattice are given by:

$$\begin{aligned} \mathbf{a_1^*} &= 2\pi(\mathbf{a_2} x \mathbf{a_3}) / \mathbf{a_1}.\mathbf{a_2} x \mathbf{a_3} \\ \mathbf{a_2^*} &= 2\pi(\mathbf{a_3} x \mathbf{a_1}) / \mathbf{a_1}.\mathbf{a_2} x \mathbf{a_3} \\ \mathbf{a_3^*} &= 2\pi(\mathbf{a_1} x \mathbf{a_2}) / \mathbf{a_1}.\mathbf{a_2} x \mathbf{a_3} \end{aligned} \qquad (3.3)$$

These vectors satisfy the following relation:

$$\mathbf{a_i^*}.\mathbf{a_j} = 2\pi\delta_{ij} \qquad (3.4)$$

Therefore,

$$a_i^* = 2\pi/a_i \qquad (3.5)$$

This means that the spacing between reciprocal lattice points is inversely proportional to the distance between points in the real space lattice. A reciprocal lattice vector **G** can be written as a linear combination of $\mathbf{a}_i^*$, i.e.

$$\mathbf{G} = h\mathbf{a}_1^* + k\mathbf{a}_2^* + l\mathbf{a}_3^* \qquad (3.6)$$

where h, k and l are integers.

Since RHEED is surface sensitive we shall now consider a diperiodic structure, that is a structure which is periodic in two dimensions only. Given that the vectors $\mathbf{a}_1$ and $\mathbf{a}_2$ define the mesh of the surface structure, a set of reciprocal lattice vectors $\mathbf{a}_1^*$ and $\mathbf{a}_2^*$ are formed such that equations (3.4) and (3.5) are satisfied.

The reciprocal lattice points of a two-dimensional (2D) structure may be thought of as rods. These reciprocal lattice rods are infinite in extent and normal to the surface plane. This becomes clearer by visualising a three-dimensional structure and expanding the structure to infinity along one of its axes. From (3.5) the reciprocal lattice points along this axis are moved closer together and in the limit form rods.

3.2.2 Diffraction from a 2-D Structure

As a result of the high electron energies used in RHEED the radius of the Ewald sphere in the reciprocal lattice is extremely large compared to the spacing of the reciprocal lattice points. Constructive interference occurs if the diffracted wavevector $\mathbf{k}_o$ and the incident wavevector $\mathbf{k}_i$ satisfy the "Laue condition" [92], that is

$$\mathbf{k}_o - \mathbf{k}_i = \mathbf{G} \qquad (3.7)$$

where **G** is a reciprocal lattice vector defined to be the 2D version of equation (3.6). The diffracted wavevector $\mathbf{k}_o$ can be determined graphically using the Ewald sphere construction in reciprocal space. Here the allowed values of $\mathbf{k}_o$ are represented by the intersection of the Ewald sphere with the reciprocal lattice. As a result of the high energies associated with the

incident electrons the Ewald sphere can be considered to be nearly flat at the origin of the reciprocal lattice. Thus the sphere will intersect the reciprocal lattice rods along their length producing elongated spots which are characteristic of RHEED patterns. However, the patterns usually consist of streaks indicative of surface disorder as will be discussed later. The intersection of the Ewald sphere with the reciprocal lattice rods determine the directions of the diffracted beams which are then projected on to a fluorescent screen normal to the shadow edge. The elongated spots or streaks are distributed over arcs of circumference as shown in figure 3.2. The separation of the streaks gives information about the periodicity of the surface atomic structure normal to the beam azimuth. In some cases the length and width of the streaks in the RHEED patterns may be correlated with the morphology of the crystal surface [22]. The appearance of spots instead of streaks in the diffraction pattern indicates surface roughness or asperities. Surface asperities usually take the form of 3-dimensional crystallites on the surface through which the RHEED electron beam will pass. The reciprocal lattice of these asperities is composed of points rather than rods resulting in a transmission or spotty diffraction pattern corresponding to the intersection of the Ewald sphere with the reciprocal lattice points [94].

3.3 Surface Reconstruction

III-V semiconductors crystallise into a zincblenbe structure in which the group III and group V atoms have an average of four electrons per atom available for binding. Although these electrons form tetrahedral covalent bonds, the two kinds of atoms do not have the same electronegativity and so the bonds exhibit some ionic character. The surface of any such crystal may be thought of as a section of the bulk crystal parallel to a given plane. In practice it is not so simple. Such a section involves the breaking of bonds and in the case of III-V semiconductors or any diamond-like structure the surface atoms have two broken bonds for (001) surfaces. These broken or dangling bonds on the surface give rise to high surface energy. Consequently the atoms rearrange themselves so as to minimise this surface energy. This phenomenon is known as surface reconstruction and has been the subject of numerous investigations [22,95-102]. These reconstructions modify the size of the unit cell at the surface and give rise to different electronic structure as compared to the bulk of the crystal [102].

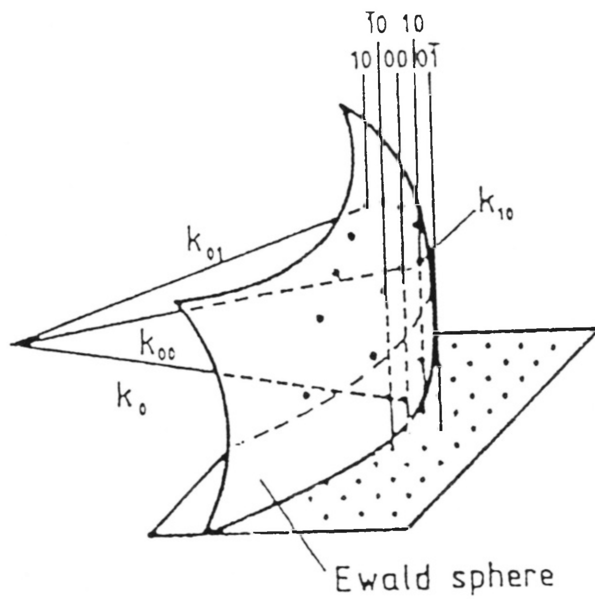

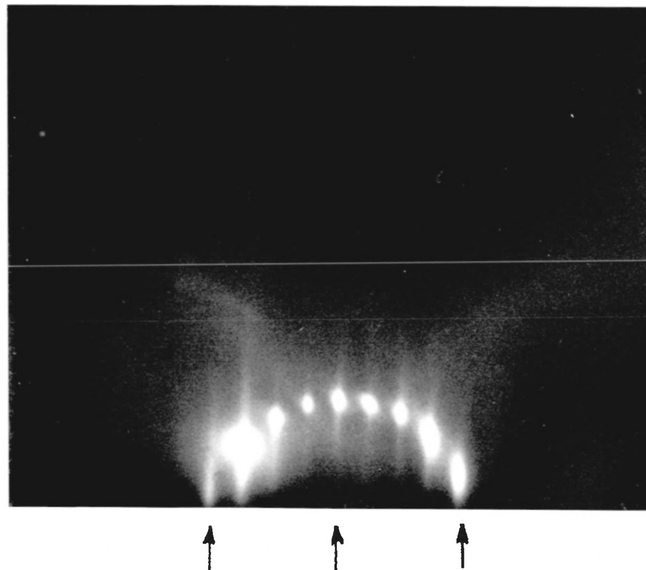

Figure 3.2 (a) Reciprocal space representation of RHEED. (After ref 93)

(b) RHEED pattern showing the elongated spots corresponding to the intersection of the Ewald sphere with the reciprocal lattice rods. This pattern is of the InSb(001)(2√2x2√2)R45° reconstruction taken along the [010] azimuth. Note the additional features present between the bulk streaks (denoted by the arrows) as a result of the surface reconstruction.

Throughout this thesis I shall be referring only to the polar (001) surface of III-V semiconductors. In this [001] direction the lattice comprises alternate layers of group III and group V atoms. Therefore the (001) surface is ideally terminated either with group III or group V atoms as shown in figure 3.3.

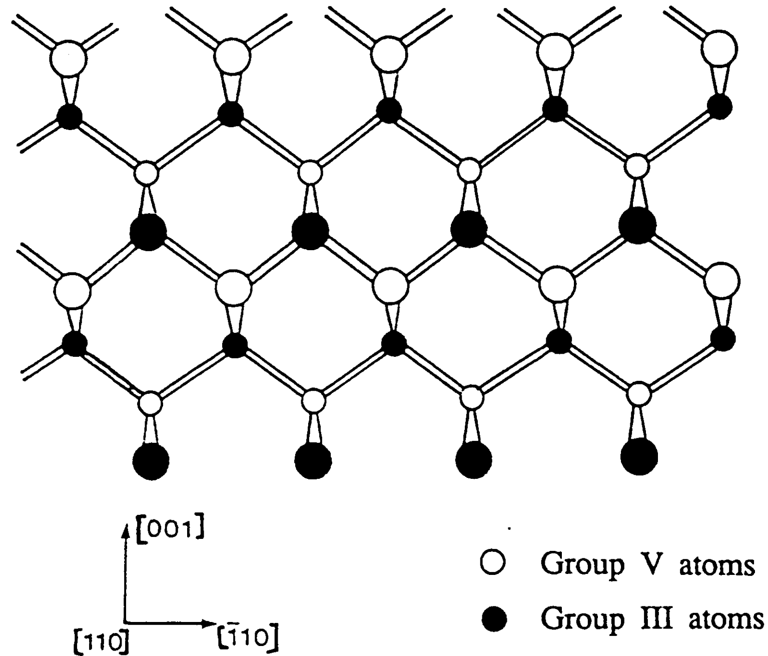

Figure 3.3 Schematic model of the polar (001) semiconductor surface showing the alternating layers of group III and group V atoms.

The (001) surfaces of III-V compound semiconductors have a large number of reconstructions associated with them depending on the actual surface stoichiometry. Throughout this thesis the Woods [103] notation for describing surface structure will be used. For example a surface structure denoted by InSb(001) $(2\sqrt{2}x2\sqrt{2})R45^{o}$ implies that an InSb crystal which is orientated with the [001] direction normal to the surface has a surface structure due to reconstruction whose unit mesh is $2\sqrt{2}x2\sqrt{2}$ larger than the underlying bulk structure and rotated through an angle of 45°. Surface meshes can also be centred an example of which is the InSb(001)c(8x2), having a surface structure whose unit mesh is 8x2 times larger than the bulk structure but includes an additional central atom.

As a result of the phenomenon of reconstruction the symmetry of the surface of a semiconductor with respect to the bulk lattice is modified i.e.

without reconstruction the surface would have had a (1x1) structure in which the position and arrangement of the atoms is exactly the same as in the bulk crystal. The result is that the size of the unit cell has a larger periodicity at the surface. This results in additional features in the RHEED patterns at fractional intervals between the bulk diffraction streaks. Such features can be seen in the diffraction pattern in figure 3.3b for the InSb(001)$(2\sqrt{2}x2\sqrt{2})R45^{\circ}$. Another name for this structure is c(4x4). For simplicity this notation will be used in later chapters.

3.4 Interpretation of RHEED Patterns

A careful analysis of RHEED patterns taken from different azimuths can yield information on surface disorder, morphology and topography [18]. One of the first attempts to interpret RHEED patterns during MBE growth was carried out by Cho [99] who was able to identify the various surface structures present during the growth of GaAs(001) and quantify these in terms of the flux ratio and substrate temperature. It was also shown that a rough substrate indicated by a spotty diffraction pattern changed to one which was atomically smooth shortly after growth characterised by a diffraction pattern consisting of streaks perpendicular to the shadow edge. This feature of MBE growth has also been reported by other workers [22,105,106] although it was pointed out by Neave and Joyce [22] that a streaked pattern alone is insufficient to define a smooth surface. Holloway and Beeby [107] used the thermal diffuse scattering mechanisms to explain the streaks. However, no experimental data is yet available to substantiate their theory.

From diffraction patterns taken from two orthogonal azimuths, information about the symmetry and the periodicity of ordered layers near the surface can be deduced together with the positions of the atoms within the unit cell, although the latter requires a detailed analysis of the diffracted beam intensity for various angles of incidence. However, no surface structure has yet been determined by this method. Hence a correlation of diffraction pattern with surface stoichiometry can be made [22,98,108].

Hernández-Calderón and Höchst [109] claimed to be able to analyse the diffraction pattern from a single azimuth to determine the surface reconstruction of α-Sn(100) and InSb(001). Such analyses however, becomes difficult when there is some lack of ordering in the reconstruction [110-112] as is usually the case for the GaAs(001)(2x4) surface

reconstruction. This lack of perfect ordering is the result of the rehybridisation of the dangling bonds of the surface As-atoms to form a tilted dimer structure during reconstruction. RHEED studies on this surface suggested that ordering is stronger in the $[\bar{1}10]$ azimuth than in the [110] direction and that disorder is the result of the phase sequencing of dimer chains in the [110] directions creating domains [113]. It was shown that the (2x4) and c(2x8) domains can co-exist on the surface and are simply the result of the random positioning of the tilted As-As dimers along the direction of the two-fold reconstruction. The presence of these two-dimensional surface disordered regions or domains which restrict the average size of the ordered areas would result in the ideal one-dimensional reciprocal rod becoming two-dimensional [104]. This would cause the streaks to become long and broad when the electron beam is parallel to the short domain side and short and narrow when the beam is parallel to the long domain side. It was also pointed out that these domains on the GaAs(001)(2x4) surface reconstruction are separated by one-dimensional or antiphase boundaries that give rise to curved streaks in the [010] direction [110]. Detailed analysis of the curved streaks in intermediate azimuths was used to distinguish between the GaAs(001)(2x4) and c(8x2) reconstructions. It is clear therefore that analysis of RHEED data should be made in all possible azimuths to avoid ambiguities.

3.5 RHEED Intensity Oscillations

In addition to providing structural and morphological information about semiconductor surfaces, RHEED also allows growth conditions to be optimised by monitoring the growing surfaces. It has been observed that the intensity of the features in RHEED patterns oscillate on the initiation of MBE growth. This temporal variation in the intensity of RHEED features has been developed into an extremely valuable technique for the *in-situ* investigation of thin film growth dynamics during MBE [114-115].

RHEED intensity oscillations were first observed during the MBE growth of Sn doped GaAs(001) [116]. It was established that the period of oscillation corresponded exactly to the growth of one monolayer of GaAs i.e. one layer of Ga and As atoms ($a_o/2$) in the [001] direction where a_o is the lattice parameter. It was also stated that the oscillations occurred as a result of a layer-by-layer growth mode but it was thought that the actual mechanism involved was related to the incorporation of the Sn dopant. However, it was

subsequently found that oscillations were present even when no dopant was used. Other oscillatory effects observed in thin film growth [117-119] were also associated with a two-dimensional growth process. This oscillatory behaviour was in qualitative agreement with the theoretical treatment of Weekes and Gilmer [120] who predicted such behaviour under certain conditions during crystal growth.

3.5.1 Nature of Diffraction Process

Figure 3.4 shows a typical plot of RHEED intensity oscillations during the growth of GaAs(001) oriented surface taken using the specular spot on the (00) beam. These oscillations are a direct consequence of layer-by-layer growth and are generally damped as the surface becomes disordered. In

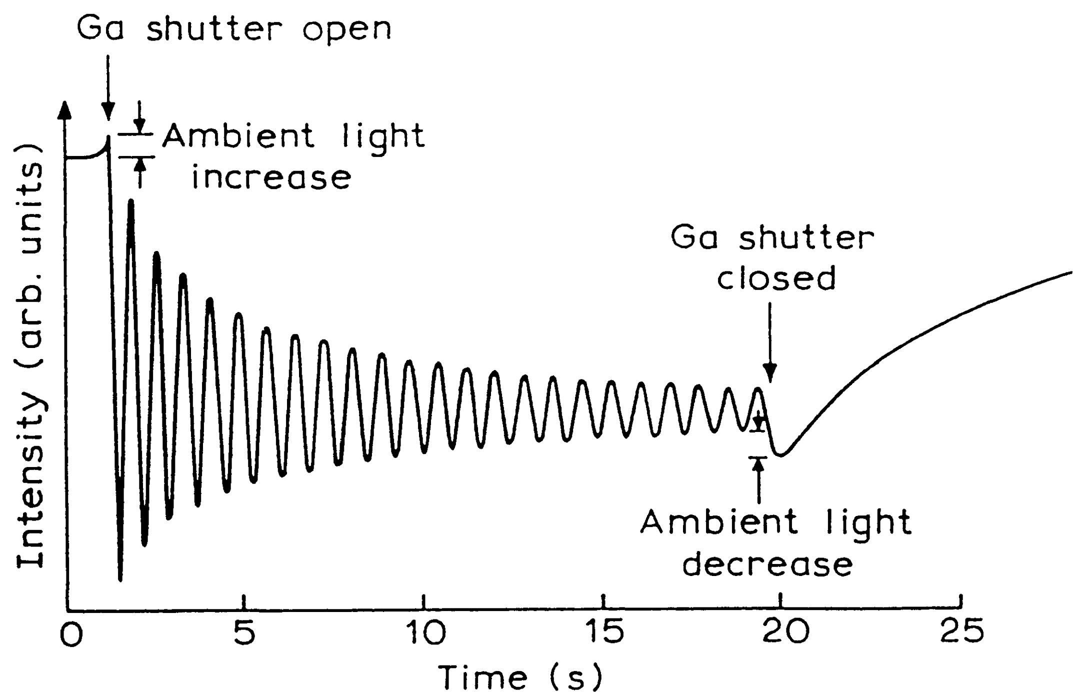

Figure 3.4 RHEED intensity oscillations during the growth of GaAs(001) taken from the specular spot of the (00) beam. (Reproduced with kind permission of B.A.Joyce)

addition, a wide range of waveforms are observed, and since the growth conditions are invariant, these were related to diffraction [127]. To determine the nature of the diffraction processes Larsen and co-workers [128] performed measurements of the intensity of the diffracted beams as a function of incident angles. Their rocking curves results indicated that highly dynamical diffraction processes are involved, confirming the theoretical work of Maksym and Beeby [126] who demonstrated that multiple scattering effects play an important role during growth. Larsen *et al* found structures on the rocking curves which could not be accounted for by purely a kinematic approach. Such an approach predicted peaks in the curves only at the primary Bragg positions. The elastic component of the specular beam was therefore considered to be due to a combination of primary Bragg diffraction, multiple diffraction processes and surface resonances. Surface resonance occurs when the Ewald sphere is tangential to a reciprocal lattice rod and an excited wave which travels parallel to the surface is prevented from emerging by the 'inner potential' of the crystal. These diffraction processes have been discussed in detail by Larsen *et al* [128]. It is also necessary to consider refraction effects since they strongly influence the angular positions at which the beams emerge. As electrons cross the surface potential barrier they gain additional energy, equal to the 'inner potential' and are therefore refracted as they enter the solid. This change in wavevector must be taken into account when constructing the Ewald sphere.

Strong features were also reported in the diffraction pattern near to the (00) rod which are fixed in position with respect to the shadow edge [129]. This was attributed to diffuse scattering in which the emergent electrons are incoherent with the incident beam following inelastic scattering involving excitation with either a phonon or a plasmon. Dynamical interaction of diffuse scattering also resulted in Kikuchi features which was shown to influence the formation of RHEED intensity oscillations during growth.

3.5.2 Origin of RHEED Intensity Oscillations

Since the discovery of RHEED intensity oscillations various models have been proposed to provide an understanding of such oscillations. Van Hove *et al* [115] measured the angular width of the specular beam as a function of time both before and during MBE growth and came to the conclusion that RHEED oscillations were related to periodic variations in the distribution of

steps on the GaAs surface. Neave and co-workers utilised an optical model to qualitatively explain the origin of these oscillations in which they equate the changes in intensity of the specular beam with changes in surface roughness [114,121]. The model proposed by Cohen and co-workers [115,125] suggest that the intensity variation is the result of an interference between beams reflected from terraces on the surface which are separated in height by one or more monolayers. Their treatment, although able to predict some features of the intensity oscillations, together with the earlier models cannot explain some of the features associated with the RHEED oscillations which are clearly diffraction related. A model considering multiple diffraction processes to explain the features in the RHEED intensity oscillations was developed by the group from Philips Research Laboratories in the U.K., and is briefly outlined below.

In explaining the oscillatory behaviour of the RHEED intensity Larsen and co-workers [128] and Zhang *et al* [129] considered diffraction to be a multiple scattering process in which the elastic component of the specular intensity is attributed mainly to multiple diffraction and surface resonances. In addition, there is also a significant contribution resulting from inelastic and incoherent processes depending on the azimuth, angle of incidence and the energy of the primary beam. As a result of the penetration of the electron beam into the solid, the determination of the angular position of the emergent beam requires that refraction effects be considered. The primary and elastically diffracted beams in the surface layer are diffusely scattered more strongly with small momentum transfer as the layer becomes disordered during growth. These diffusely scattered electrons then penetrate into the bulk of the solid and reflected back by Kikuchi processes. The conclusion therefore is that RHEED intensity oscillations during steady state growth is the contribution from the periodic variation of the diffusely scattered electrons, with some of the transferred intensity going into Kikuchi features.

Double period oscillations in the RHEED intensity observed for certain angles of incidence were accounted for by the dynamical interaction between the specular beam and the Kikuchi related feature present on the (00) rod. The oscillations for this feature are 180° out of phase with those from the specular beam. A combination of these two oscillations would produce a doubling in the period of the intensity of the oscillations. This is in contrast to the double period oscillations observed during the growth of Si

[122]. It was reported that bilayer ($a_o/2$) mode oscillations in the specular beam occur when the incident beam is along the [110] direction although the usual monolayer ($a_o/4$) mode oscillations can be observed along the [010] azimuth. Kawamura *et al* explained this discrepancy by using a model in which the islands are elongated with the longer dimension alternating between the [$\bar{1}$10] and the [110] directions [123]. The effect resulting from the combined diffraction of the Kikuchi related feature and the specular spot is also responsible for the changing phase observed when the angle of incidence is varied.

3.5.3 Applications of RHEED Intensity Oscillations

The use of RHEED intensity oscillations to study growth dynamics and effects which depend on the knowledge of layer completion, such as heterojunction formation, requires quite specific diffraction conditions. The effects of diffraction conditions manifest themselves in the transient and phase of RHEED oscillations. From a study of these phase relationships as a function of angle of incidence and azimuth it was shown that the maxima in the oscillations correspond to layer completion only when the time from the initiation of growth to the second minimum is 1.5 times the steady state period [130].
Notwithstanding the fact that any detailed study of MBE growth process using RHEED oscillations requires a specific set of diffraction conditions, a great deal of information can be obtained from the periodicity of these oscillations. Even if the maxima in the oscillations do not correspond to layer completion, the basic concept of layer-by-layer growth is still valid. Excluding double period oscillations the following information can be extracted from the steady state period of RHEED oscillations.

(1) Growth rate and flux calibration: A measurement of the period of oscillation obviously provides an *in-situ* growth rate monitor with fractional layer precision. Since the sticking coefficient of the group III element is unity under most growth conditions (moderate temperatures) this can be used to calibrate the group III flux emanating from the K-cell. The group V incorporation rate can be calibrated using a technique similar to arsenic-induced RHEED intensity oscillations employed for arsenic incorporation determination [131]. From a knowledge of the sticking coefficient of such fluxes the incident group V flux can be calculated.

(2) Alloy Composition: In the case of III_AIII_BV alloys, provided the group III sticking coefficient is unity then the alloy composition can be determined from the individual group III growth rates. However there are cases when the sticking coefficient of the group III atoms is not always unity. An example of which is $Al_xGa_{1-x}As$ where high growth temperatures are required. In such circumstances the alloy composition can be determined by measuring the change in the period of oscillation when the second of the two group III fluxes is introduced during growth.

The $IIIV_AV_B$ alloys present some difficulties when using RHEED oscillations to determine alloy composition simply because the sticking coefficient of the various group V fluxes need to be accurately known. However in the case of $InAs_xSb_{1-x}$, at normal growth temperatures Sb usually sticks to the surface in preference to As. Hence by measuring the Sb flux (using Sb-induced oscillation) and the In flux during the growth of InSb the alloy composition can be determined. During the course of this research RHEED oscillations were observed for the first time on InSb. These will be presented in chapter 5.

CHAPTER 4 MBE GROWTH EQUIPMENT AND PROCEDURES

In this chapter the MBE growth equipment used throughout this research is described. Some of the routine procedures adopted in the preparation for the growth of high quality III-V compound semiconductors are also presented. This system is housed in the Department of Physics at Imperial College, London.

4.1 System Configuration

The Vacuum Generator Semicon V80H MBE system comprises three stainless steel ultra high vacuum (UHV) chambers, separated by gate valves and pumped independently. These are the deposition or growth chamber, the preparation chamber and a fast entry load lock. Figure 4.1 shows the system. Sample transfer between chambers is realised using a rack and pinion mechanism with UHV rotary motion drives and wobble sticks to handle the substrates which are transported facing downwards.

4.2 Deposition Chamber

The deposition chamber, figure 4.2, contains the Knudsen effusion cells (K-cells), the substrate holder and analytical facilities which include a beam monitoring ion gauge (BMIG) to monitor the incident fluxes, reflection high energy diffraction and a 1-100 amu quadrupole mass spectrometer.

The K-cells contain the source materials and generate stable high purity molecular (group V) and atomic (group III) beams. In front of each cell there is a fast action magnetically actuated shutter capable of opening and closing with a nominal response time of < 0.1 sec. Since growth rates in MBE are generally low - around one monolayer per second i.e. about one micron per hour, this would in principle, allow compositional or dopant changes to be made to atomic layer precision. However, severe problems can arise from the existence of transients in the beam flux intensity when the shutter is opened. In particular, this is a major problem with the antimony flux as will be discussed in the next chapter. The cells are mounted in a semi-horizontal arrangement which allows the source material to be retained by gravity and reduces contamination from falling flakes of condensed matter. To minimise chemical and thermal 'cross-talk' each cell is surrounded by a liquid nitrogen baffle and cooled by recirculating chilled water.

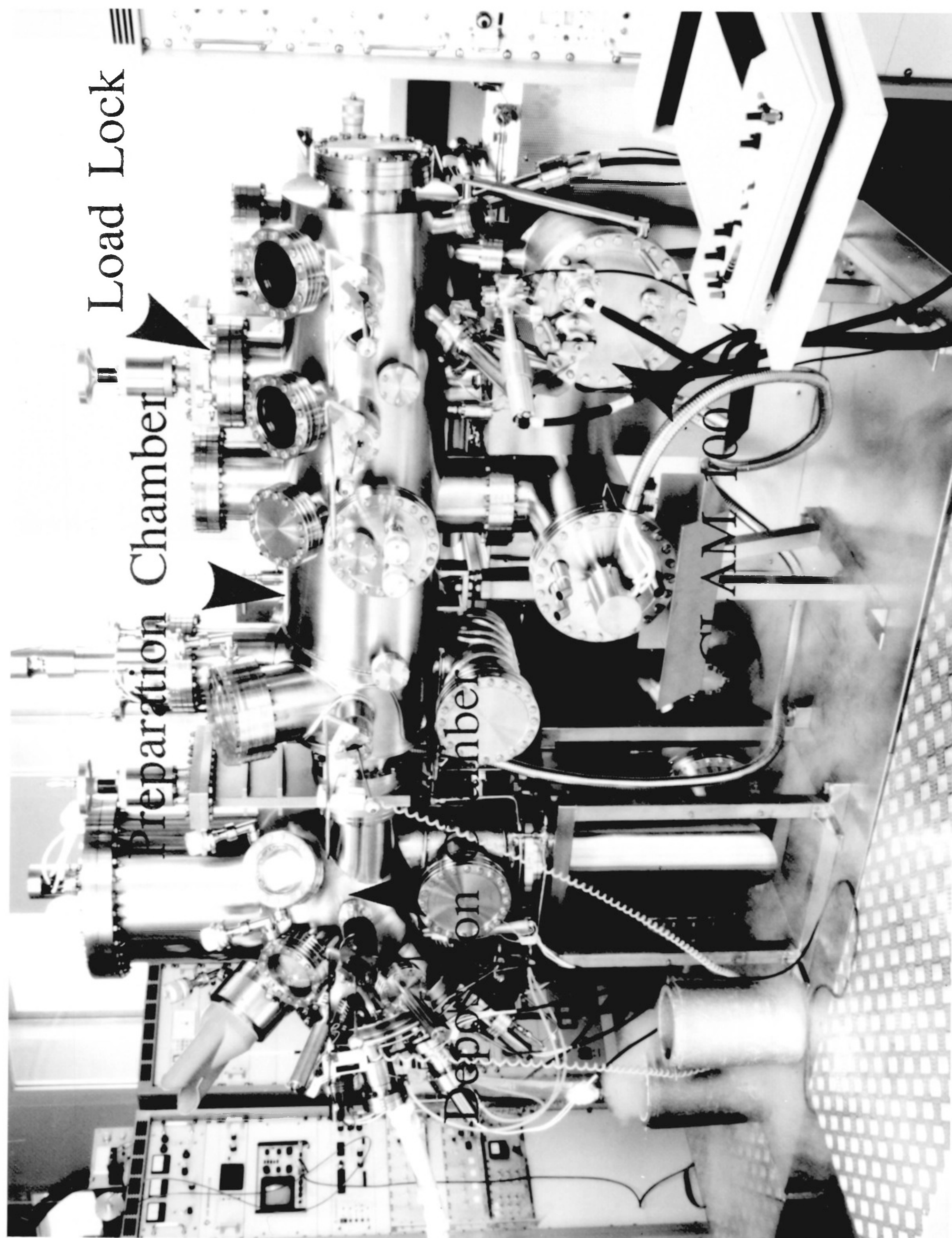

Figure 4.1 The VG V80H MBE system.

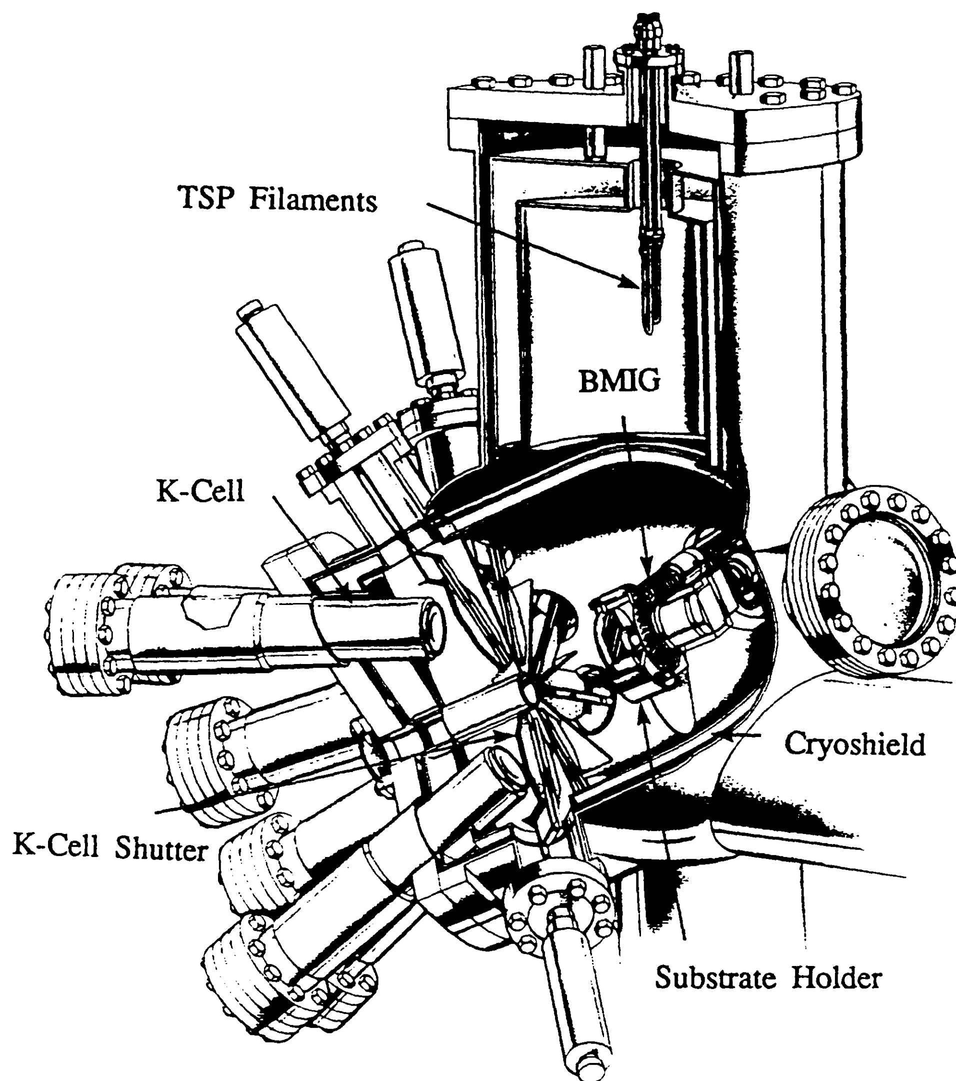

Figure 4.2 A cutaway diagram of the deposition chamber. (Reproduced from VG information brochure)

4.2.1 Molecular Beams: Generation and Monitoring

The atomic and molecular beams used in MBE growth are thermally generated in K-cells. Figure 4.3 shows one such cell. The growth materials are contained in pyrolytic boron nitride crucibles which are heated by radiation from foil

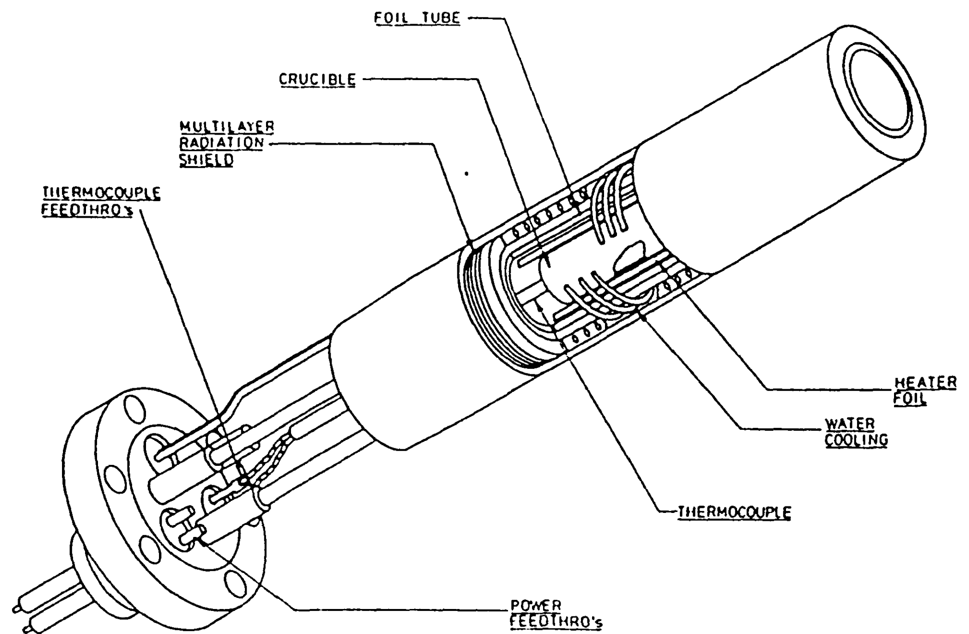

Figure 4.3 A Knudsen cell used in MBE systems to generate the beam fluxes. (After ref 132)

heaters surrounding the crucibles. The use of pyrolytic boron nitride crucibles ensures that possible contaminant levels are kept to a minimum during growth. For a true Knudsen cell, in which the mean free path of the vapour atoms or molecules is much larger than the cell orifice, the flux striking unit area of a substrate at a distance d away can be expressed as:

$$J_i = \frac{pAN}{\pi d^2 \sqrt{(2\pi M_i RT)}} \quad \text{molecules cm}^{-2}\ \text{sec}^{-1} \qquad (4.1)$$

where p is the pressure in the cell; A the area of the cell orifice; N Avogadro's number; T the temperature of the cell (in K); R the gas constant and M_i the molecular weight of the source material. The cell temperatures are controlled using a computer via individual Eurotherm temperature controllers employing temperature feedback.

In commercial MBE systems the K-cells are far from being ideal Knudsen sources. They have large orifice area so as to achieve enhanced growth rates

at lower cell temperatures. It should be noted that this non-ideal behaviour is due to the non-equilibrium nature of the K-cell. Although, at the pressures involved in MBE the flow from the cell is still molecular the gas-solid equilibrium is constantly being disturbed whenever the shutter is opened. Consequently the surface area of the source material becomes important in terms of flux stabilization. As a result the relationship between cell temperature and incident flux cannot be accurately determined. An alternative, and the most widely used method of determining beam fluxes, is to measure the beam equivalent pressures (BEPs) using a movable ion gauge normally situated at the back of the substrate stage. From the BEPs the relative flux in each beam can be determined [41,133]. The beam monitoring ion gauge (BMIG) is generally used to set up the flux ratios, and check the reproducibility of the group III and group V components prior to growth; the absolute magnitudes of the fluxes are not measured. Because the ion gauge is essentially a density monitor the relative average velocity of each species must be considered when comparing the BEPs [134]. Using the relative BEPs the flux ratio may be calculated from:

$$J_x/J_y = (P_x/P_y)(\eta_y/\eta_x)\surd(T_xM_y/T_yM_x) \qquad (4.2)$$

where J_x is the flux of species X; P_x its beam equivalent pressure and T_x, M_x the absolute temperature and molecular weight respectively. η is the ionisation efficiency relative to nitrogen and is given by:

$$\eta/\eta_{N2} = [(0.4Z/14) + 0.6] \qquad (4.3)$$

where Z is the atomic number.

4.2.2 Source Materials

Elemental In (6N MCP), Ga (9N Alusuisse), Sb (6N MCP), and As (6N Preussag) are used as source materials. In addition Si (6N Wacker) and Be (5N Krystal Kelpin) are used for n- and p-type dopants respectively. The arrangement of these cells is shown in figure 4.4.

The group III source materials are liquid at their normal operating temperatures during growth, so the cells are placed in the lowest possible positions to prevent these materials from flowing out. The group V materials on other hand, are not liquid at growth temperatures but they do have high

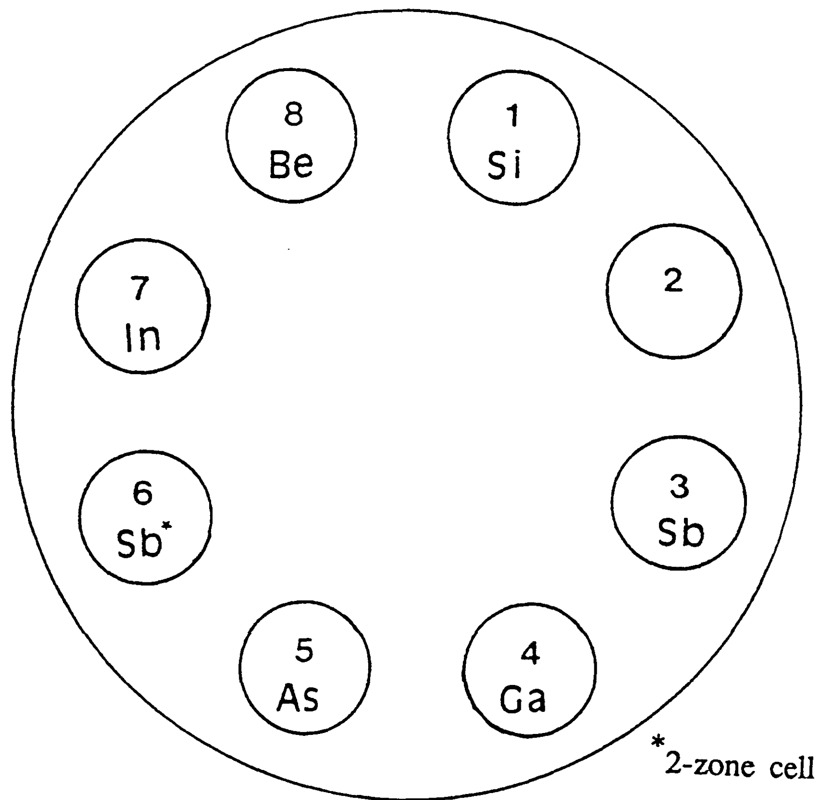

Figure 4.4 The arrangement of the K-cells containing the source materials used in this study.

vapour pressures. Because of this arsenic and antimony tend to deplete most rapidly. By placing these cells also in the lowest available positions they can be filled to the top. Sometimes more than one cell is used. One solution to the problem of the rapid depletion of the group V materials is to use shaped charges having dimensions of the crucible. In this way the cells can be filled with the maximum amount of material. Such charges will shortly be available from MCP, U.K.

The antimony cell was initially placed in position 2 but at this position it was found that antimony accumulated at the top end of the cell, condensed into a ball and eventually blocked the orifice. Two possible solutions to this problem were considered. First the cell was moved to a lower position with the hope that gravity would prevent the build up of antimony. So far

this has proved to be successful in that no significant condensation was seen to occur and the antimony flux remained stable (±3% as measured by RHEED oscillations) throughout subsequent layer growth. However a significant amount of antimony in the form of flakes was still present on the shutter and on the cooling fins around the end of the cell. The second solution considered the temperature at the top end of the cell. It was thought that the condensation of antimony around the area of the orifice resulted from the top end of the cell being cooler than the bottom end. A new type of K-cell was therefore designed by VG Semicon in which two independent heaters were employed. The additional heater was placed at the top end of the cell with the aim of keeping the area around the orifice hot enough to prevent condensation. This cell was placed in position 6. Its performance in overcoming the initial problem is now being assessed.

The arsenic charge is supplied in the form of granules sealed in a quartz ampoule. Recharging the cell is carried out by scribing and breaking the top of the container and emptying the contents into the crucible. Antimony however, is supplied in the form of large 500gm ingots which have to be broken into small pieces to fit into the crucible. This was normally carried out by wrapping an antimony ingot in a thin foil of etched molybdenum before being crushed with a small hammer.

The dopant materials, Si and Be, have very low vapour pressures. They do not melt at the temperatures used during growth and very small quantities are used during a typical growth run. Hence they are placed in the top positions as shown.

4.2.3 The Substrate Holder

The substrate holder consists of a molybdenum (Mo) block which is heated by radiation. A schematic layout is shown in figure 4.5. Molybdenum is used because it is a refractory metal and can be obtained in a high purity form (usually 99.97%). The Mo block can accommodate substrates up to three inches in diameter which are fixed using indium solder. The indium, which is liquid at normal growth temperature, holds the substrate by surface tension and provides excellent heat transfer. The substrate can be rotated in a plane perpendicular to the incident beams. It has been shown that rotation of the substrate during growth reduces the lateral variation in thickness and composition and improves doping uniformity over the substrate arising from

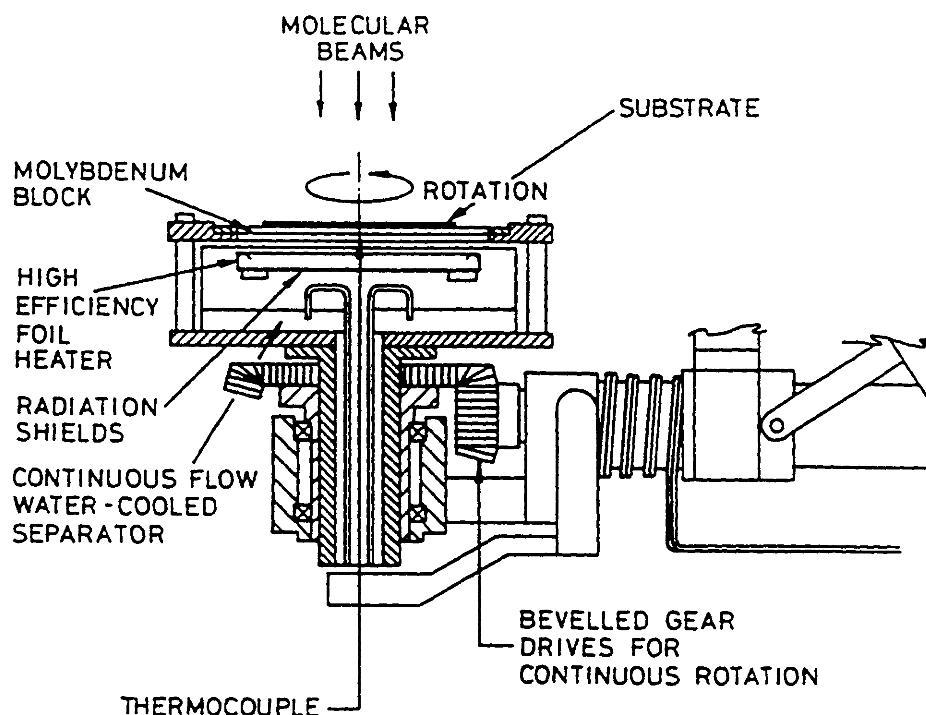

Figure 4.5 A schematic layout of the substrate holder showing the various components. (After ref 132)

the non-uniform distribution of the beams, emanating from the K-cells [135-137]. Temperature measurement is achieved using a thermocouple situated between the Mo block and the heating element. The problems associated with this arrangement will be discussed later in this chapter.

4.3 The Preparation Chamber

The preparation chamber is used for outgassing new Mo blocks and pre-growth cleaning of new substrates. In effect this acts as a buffer chamber between the load lock and the growth chamber. This ensures that the growth chamber will remain free from contamination whenever a new substrate is inserted for growth. In the preparation chamber new GaAs substrates are outgassed prior to growth and InSb substrates are cleaned using argon ion sputtering and thermal annealing. This chamber is also equipped with a "cassette style" parking stage for storing up to 10 Mo blocks and so allowing a variety of

substrates, including test samples to be kept under UHV conditions. There is also an analysis section which can be used for detailed surface analytical studies on MBE grown materials without exposing the sample to atmosphere.

4.4 The Load Lock

The fast entry load lock allows new substrates and samples to be inserted or taken out of the system without the need to expose the growth chamber or the preparation chamber to the atmosphere. The load lock was first introduced to MBE systems in 1978 [138] enabling the exchange of samples to be carried out in a short period of time as compared to the time required for epilayer growth. More important is the fact that there is a significant reduction in the contamination of the K-cells and substrate holder whenever a wafer is loaded or removed from the system. This resulted in highly improved material quality as exemplified by the growth of DH (double heterostructure) lasers [139]. The load lock is equipped with a cassette holder capable of holding 10 Mo blocks facilitating a serial cycling of wafers through the pre-growth processing and layer growth stages so that substrate insertion and removal no longer limit the throughput for MBE III-V materials.

4.5 Analytical Facilities

The UHV environment allows a number of surface analytical facilities to be incorporated so that both the chemical and structural properties of epilayers can be monitored before, during and after growth.

Reflection High Energy Diffraction (RHEED) is the main analytical technique used during the growth of the epilayers. The RHEED system consists of a VG Scientific LEG110 electron gun capable of producing an electron beam in the range of 5-15 keV with a minimum spot size of 100µm. As seen in the previous chapter its geometry is ideal for monitoring the growth front thereby providing information on surface reconstruction and hence stoichoimetry, and topography.

Auger Electron Spectroscopy (AES) can be performed in the analysis section of the preparation chamber. This facility is centred around a VG Scientific CLAM (Combined Lens Analyser Module) 100 system. It consists of a high resolution 150° spherical sector analyser, a LEG 61 electron gun with a variable spot size of between 30 µm to below 5 µm with beam currents of 50

μA to 0.3 μA respectively, relevant driving electronics and a sample holder mounted on a xyz horizontal manipulator. Throughout this work AES was used mainly to check the chemical composition of the surface of the InSb substrates after argon ion cleaning just prior to growth and the epilayers after growth. In addition the analysis section has the capability to perform Auger depth profiling.

A 1-100 amu Masstorr quadrupole mass spectrometer is mounted in the growth chamber and is used as a residual gas analyser. In addition, a movable ion gauge is located on the substrate holder and is used to estimate the relative flux of the incident beams.

4.6 Pumping Arrangement

For good quality MBE growth a base pressure of less than 10^{-10} mbar is required. To achieve these UHV conditions various pumps are used. The growth chamber is equipped with an ion pump, a titanium sublimation pump and a cryopump in addition to a liquid nitrogen cryopanel surrounding the growth area. The preparation chamber is pumped with an ion pump and a titanium sublimation pump although the latter was not used while argon ion sputtering was carried out. The fast entry load lock is pumped independently with a turbomolecular pump. Sorption pumps are used to rough pump the entire system.

Sorption pumps operate on the principle of physical adsorption of gases on the surfaces of molecular sieves. For greater efficiency during operation the pump is cooled by immersing in a dewar of liquid nitrogen.

The main UHV pumping is provided by the ion pump. During its operation electrons are emitted from a cathode and collide with gas molecules forming ions. These positive ions in turn bombard the cathode and sputter metal which form stable compounds with the chemically active gas molecules. The pumping speed depends on the chemical nature of the gases - nitrogen, oxygen, carbon monoxide, carbon dioxide, hydrogen and helium are pumped efficiently. However, ion pumps cannot handle large loads of inert gases.

Titanium sublimation pumps (TSP's) are used in conjunction with other high vacuum pumps. Chemically active gases react with a film of titanium deposited on a condensing surface by the electrical heating of titanium

alloy filaments. Pumping speeds are considerably increased when the condensed surface is cooled to liquid nitrogen temperatures.

The turbomolecular pump, backed using a rotary pump is the only through-put vacuum pump used in which the pumping load is ejected to atmosphere. Once at operating speed, pumping is very rapid from about 10^{-3} mbar. As such it is used to pump the fast entry load lock which is regularly opened to atmosphere.

The growth environment is surrounded with a cryopanel which is kept at liquid nitrogen temperature during growth. This provides the main pumping during growth as it ensures that any background contaminants in the chamber are kept to a minimum. It also provides a surface onto which any desorbing species, e.g. the group V molecules from the semiconductor surface can be captured during growth. The cryopanel is very effective in pumping CO_2 and water vapour and so care is always taken during growth to ensure that the cryopanel does not increase in temperature as the CO_2 will be readily desorbed.

4.7 Attainment of UHV Conditions

Once the MBE system has been exposed to atmosphere for recharging the K-cells or for routine maintenance, it is essential to carry out rigorous outgassing procedures to ensure that the residual gas environment is ultraclean. The ultimate aim is to eliminate altogether the active gases such as H_2O, O_2, CO, and CO_2 as these tend to degrade the electrical qualities of III-V compound semiconductors. Unintentionally-doped GaAs is generally p-type. This is probably due to the incorporation of carbon [140]. In n-type layers the presence of compensating C acceptors leads to a reduction in the low temperature mobility due to the role of ionised carbon as an effective electron scattering centre. In addition oxygen incorporation in GaAs is thought to be the cause of electron and hole traps [141-143].

Initially sorption pumps are used to evacuate the entire system to about 10^{-3} mbar. These are then isolated and pressures of between 10^{-7} and 10^{-8} mbar are achieved using ion pumps. However, the main barrier to achieving lower pressures is the presence of water vapour on the walls of the stainless steel chamber. To overcome this the entire system is baked at $180^{\circ}C$ for about 4 to 5 days. Before and after baking the chambers are leak

tested using helium gas with the aid of the quadrupole mass spectrometer. The cryoshield surrounding the growth environment and the condensing surface of the TSP's are then cooled to liquid nitrogen temperature and the K-cells containing the source materials are outgassed. At the same time all components which are likely to exceed $150^{o}C$ are also outgassed. These include the substrate holder, the ion gauge filaments and grids, the quadrupole mass spectrometer, the TSP filament and the RHEED electron gun in the growth chamber. In the preparation chamber these include the outgassing stage, the argon ion gun, the AES electron gun, the TSP filament and the Mo blocks. During the heating of the K-cells, residual gas analysis indicates that H_2, CO and CO_2 are the principal species generated. After bakeout and outgassing the base pressure is usually better than $5x10^{-11}$ mbar and a mass spectrum, figure 4.6, shows the predominant species in the growth chamber to be H_2 with some residual H_2O, and CO.

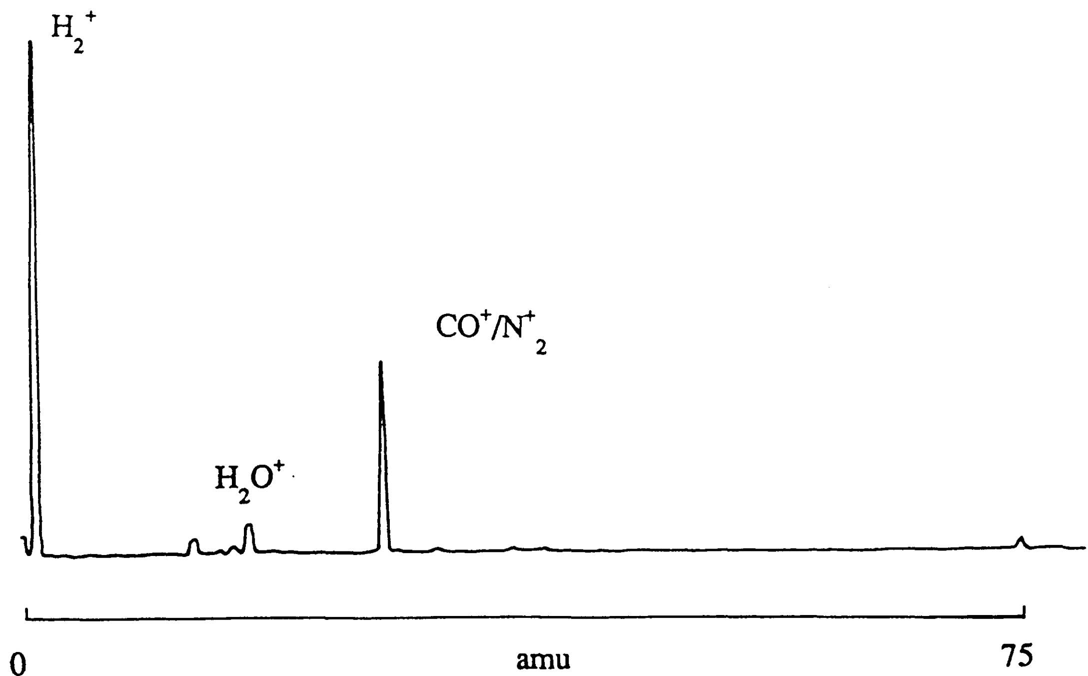

Figure 4.6 Mass spectrum showing the predominant gaseous species in the growth chamber after bakeout and outgassing.

4.8 Substrate Preparation

One of the most important aspect of good quality MBE growth is the preparation of the substrate. Atomically smooth and clean substrates are required to encourage the growth of epilayers with good morphological qualities. In this study various substrates were used ranging from semi-insulating GaAs(001) (MCP, ICI), n- and p-type InSb(001) (MCP) to undoped GaSb(001) (MCP).

4.8.1 *Ex-situ* cleaning

Polished substrates are supplied by MCP and ICI Wafertech. These are then degreased by boiling in propanol, trichloroethylene, acetone and methanol in that order after which they are etched in a freshly prepared acidic mixture for between 2 and 5 minutes. The acidic mixture comprised of H_2SO_4:H_2O_2:H_2O in a proportion of 8:1:1 by volume for GaAs, CH_3.CHOH.COOH(lactic acid):HNO_3:HF in a proportion of 25:4:1 by volume for InSb and a solution of 0.1% bromine-methanol for GaSb. This procedure removes the top few microns from the surface by an oxidising process which eliminates any residual damage that may have resulted from polishing and transportation. A layer of oxide is then grown by submerging the etched surface in de-ionised water for between 3 and 8 minutes. Afterwards the substrate is blown dry with filtered nitrogen and then mounted on the molybdenum block using molten indium of 6N purity. The block is then loaded into the MBE system via the load lock.

4.8.2 *In-situ* Substrate Cleaning

Once the pressure in the load lock has dropped to about $2x10^{-8}$ mbars the substrate is transferred into the preparation chamber. GaAs substrates are initially outgassed at 300 ^{o}C for a minimum period of one hour prior to insertion into the growth chamber. This heat treatment desorbs any water molecules and volatile contaminants from the substrate and Mo block. After transferring to the growth chamber the GaAs substrate is heated slowly to a temperature of 600 ^{o}C in a beam of As_4. At this temperature the native oxide is desorbed. This is monitored using RHEED where the pattern changes to a sharp (2x4) As-stable reconstruction. On some substrates there was evidence of facets immediately after oxide desorption. However these were eliminated by annealing the substrate at 620 ^{o}C for 30 minutes. At this stage the substrate is considered to be atomically clean and smooth and ready for

growth.

In the case of InSb *in-situ* substrate preparation has been a major problem. Whereas for GaAs the oxide passivating layer formed as a result of chemical etching can be easily desorbed thermally, no such passivating layer has been found for InSb substrates which can be as easily removed and at the same time be resistant to atmospheric contamination. Various overlayers were produced *ex-situ* and examined [144,145]. Heating the oxides *in-situ* gives rise to In droplets [146] and heat treatment is insufficient to remove a high initial carbon concentration [147]. With chloride films it was shown that a 60% reduction in carbon contamination was possible using a Cl_2 plasma for about 20-30 secs to grow the chloride overlayer [145,148]. However, the production of chloride overlayers requires special equipment and so was not considered.

An alternative *in-situ* procedure for preparing InSb substrates is to sputter away the topmost few monolayers using an energetic beam of argon ions. Although this method has the disadvantage of producing crystal damage it does remove nearly all the active contaminants such as oxygen and carbon. The surface damage is normally reduced by annealing the cleaned substrates. InSb substrates are sputtered using a beam of 500eV argon ions, in an Ar pressure of $5x10^{-5}$ mbar for one hour at a temperature of $100^{o}C$, after which they are annealed at $200^{o}C$ for another hour. Normally one cycle of ion bombardment and thermal annealing is sufficient to completely remove any oxygen and carbon, as detected using AES with a signal to noise ratio greater than 100 as measured using the Sb (458eV) MNN peak from a clean InSb substrate. A typical Auger spectrum of the InSb surface before and after cleaning is shown in figure 4.7.

4.9 Calibration of Substrate Temperature

Perhaps the most difficult growth parameter to measure accurately is the substrate temperature. This difficulty arises because the thermocouple is situated at some distance away from the substrate, between the heater elements and the rotating Mo block. Changes in the emissivity of the Mo blocks can also affect the measured values. In the V80H MBE system errors as large as $350^{o}C$ have been recorded, during the course of this study, between the real temperatures and those measured by the thermocouple.

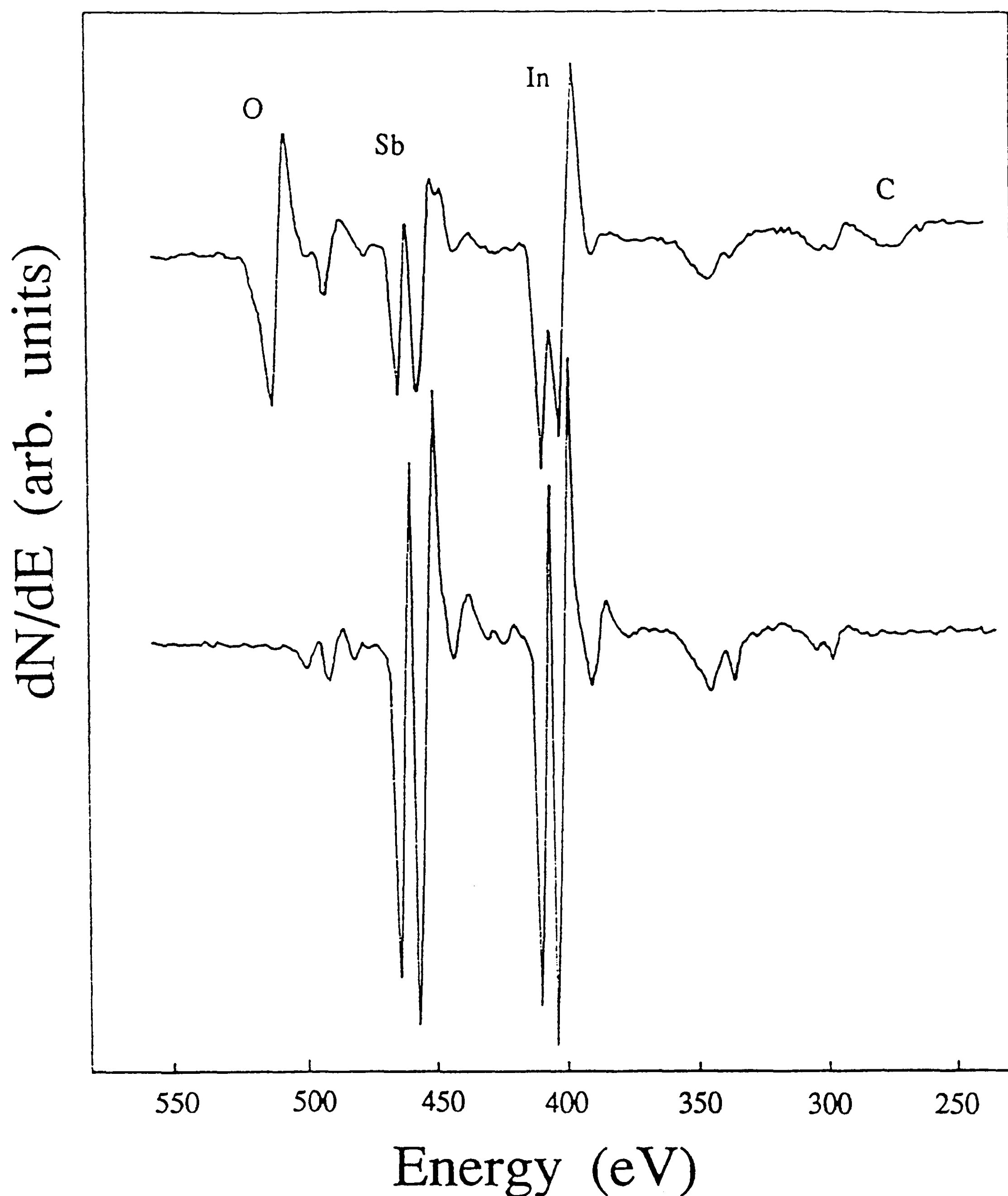

Figure 4.7 A typical Auger spectrum of an InSb substrate before and after argon ion cleaning.

The most reproducible way of determining the substrate temperature is to monitor the transition temperature, T_T, between surface reconstructions [112,150]. This temperature is system-independent and provides a method to improve reproducibility and facilitate the comparison of results from different laboratories [67,151,152]. For GaAs this method involved the

careful monitoring of the reversible c(4x4) to (2x4) reconstruction change which occurred when the GaAs(001) surface was either heated or cooled in an As_4 overpressure. For any given values of As_4 flux this transition temperature, T_T has been found to be extremely reproducible [112] and can therefore be used to provide a very reliable reference point for substrate temperature calibration. An additional reference point for calibration is the temperature at which the oxide desorbs from the surface of a new GaAs substrate. This reference point was invariably used during growth because flakes of antimony produce a small amount of Sb_4 flux which modified the reconstruction of the GaAs(001) surface. The antimony flux was produced whenever the Ga cell was heated to its operating temperature because of its close proximity to the antimony cell. The modification of the GaAs(001) reconstruction made it impossible to monitor the transition between the c(4x4) and the (2X4) reconstructions. The oxide desorption temperature was estimated to be 590°C using an infrared pyrometer.

The reference point during the growth of InSb(001) was taken to be the transition between the c(4x4) and the so-called "pseudo" or asymmetric (1x3) reconstructions [150]. For the flux ratios and growth rates used in this study this transition temperature was estimated to be 370°C during growth and 20°C higher under static conditions i.e. with the surface annealing in a Sb_4 flux. The difference in the these two temperature can be seen from the surface phase diagram of figure (2.3) which shows the transition to be dependent on the group V/group III flux ratio.

All InAs epilayers were grown heteroepitaxially on GaAs, hence the GaAs(001) oxide desorption temperature was used to calibrate the InAs growth temperature due to a lack of any clear reconstruction changes during the growth of InAs epilayers. In the case of heteroepitaxial growth of InSb the transition temperature between the InSb(001) c(4x4) and the "(1x3)" reconstructions was determined after about 10-15 minutes of InSb growth. The growth temperature calibration for $InAs_xSb_{1-x}$ was determined using one of the above procedures depending on the substrate used.

CHAPTER 5 THE GROWTH OF NARROW GAP SEMICONDUCTORS BY MBE

5.1 Introduction

In this chapter the MBE growth of InAs, InSb and $InAs_xSb_{1-x}$ is described. The steps taken during the preparation of the growth environment are first outlined, then the growth conditions used throughout this study for layer growth will be presented. During the course of this research RHEED intensity oscillations were for the first time, observed during the growth of InSb. A summary of this work is presented in this chapter. In addition, the results of a RHEED study on the initial stages of the heteroepitaxial growth of InSb on GaAs will be given. The observation of RHEED oscillations represent a significant advancement in that it shows conclusively that layer-by-layer growth is occurring and also allows for the *in-situ* calibration of fluxes. Finally the surface morphology of the layers grown will briefly be discussed in terms of the growth conditions.

5.2 Experimental

When the MBE system is in a state of idleness, e.g. overnight and at weekends, the K-cells and the substrate stage, containing a blank molybdenum plate, are kept at $200^{\circ}C$ with the exception of the arsenic cell which is set to $120^{\circ}C$. This prevents any significant build up of contaminants, especially on the shutters. Prior to growth, the cryopanel is cooled to liquid nitrogen temperatures. The K-cells are then ramped to $50^{\circ}C$ above the temperatures used during growth with the exception of the group V sources which, because of their high vapour pressures, are ramped slowly to their operating temperatures. At the same time the substrate stage is ramped to an indicated temperature of $950^{\circ}C$. They are maintained at these temperatures for a minimum of one hour to ensure thorough outgassing. The aim of this outgassing procedure is to reduce the carbon and oxygen containing gases in the growth environment since these affect material quality. Figure 5.1 shows mass spectra taken at various stages during the preparation of the growth environment. During this period, the substrates are themselves outgassed in the preparation chamber or in the case of InSb, argon ion sputtering and thermal annealing are used.

After outgassing, the K-cells are set to the normal temperatures used for

growth, typically 880 °C, 1080 °C, 560 °C and 285 °C for the In, Ga, Sb and As cells respectively. The substrate stage is set to a measured temperature of 300 °C. The substrate is then transferred into the growth chamber. During growth the titanium sublimation pump and filaments of the BMIG and mass spectrometer are switched off as these are potential sources of contamination. In addition, the minimum possible use is made of the RHEED equipment during growth.

As mentioned in the previous chapter, the incident fluxes are not uniformly distributed over the substrate. In order to achieve layer uniformity therefore, the substrate is rotated during the growth period. Figure 5.2 shows the effect when Sb was deposited onto a cold piece of silicon which was not rotated.

5.2.1 Flux Ratios and Calibration of Dopant Fluxes

For stoichiometric growth of III-V compound semiconductors, at normal growth temperatures used in MBE, the ratio of the group V to group III species is usually greater than unity. The beam monitoring ion gauge is used to set the relative fluxes to ensure that $J_V/J_{III} > 1$. For the group III fluxes the beam equivalent pressures used for growth are typically 7×10^{-7} mbar, corresponding to a growth rate of about 1 monolayer per second while those for the group V molecules are usually set to between 5 and 10 times greater than the group III BEPs. However, for absolute flux measurements, use is made either of the *in-situ* RHEED oscillation technique or an *ex-situ* thickness measurement although the latter is avoided whenever possible since this involves the deposition of the group III and group V species separately onto cold substrates and then measuring the thickness of the deposited layers. During the initial stages of this study it was found that thickness measurement for flux calibration was time consuming. In addition, there can be errors associated with measuring the thickness of the deposited layers.

For InSb growth it has been reported that the best quality material was obtained using a flux ratio close to unity [49,51,153]. Consequently, it was necessary to obtain a quick and reliable method, preferably *in-situ*, for measuring the fluxes. Initially the BMIG and *ex-situ* thickness measurements were used [154] but the former turned out to be inaccurate and the latter time consuming. Later however, as a result of RHEED oscillations observed during InSb growth [155], it was possible to measure both the antimony and

the indium fluxes *in-situ*, with a great degree of accuracy. Even more useful was the fact that during the growth of $InAs_xSb_{1-x}$ the measurement of the antimony flux, which is the controlling group V species, using the RHEED oscillation technique allows the composition to be determined as will be discussed later.

Although the group III and group V fluxes can be determined *in-situ* by the RHEED oscillation technique, the dopant fluxes are too small to be measured. These were calibrated in the conventional way by growing a GaAs epilayer doped in a staircase manner as shown in figure 5.3a. C-V profiling was then carried out on these samples by J. Bellchambers at Philips Research Lab, Redhill to determine the n- and p-type carrier concentrations for Si and Be respectively at the various cell temperatures. These were then used to calibrate the fluxes from the two cells. Figure 5.3b shows the calibration curves obtained. Of course, for these to be used with any degree of accuracy, the compensation in the staircase samples must be zero. This was assumed to be the case since GaAs epilayers previously grown in identical conditions exhibited electrical characteristics which indicated very little, if any, compensation for the dopant concentrations considered. In using these calibration curves to calculate the cell temperatures for a specific doping density, any change in the growth rate and lattice parameter must be taken into consideration.

5.2.2 Thickness Determination

Epilayer thickness is usually determined to fractional monolayer precision using the RHEED oscillation technique as described in chapter 4. However, initial attempts at the thickness determination of InSb epilayers proved to be difficult since RHEED intensity oscillations were not observed during the growth of this material. As a result, *ex-situ* methods were relied upon [154]. A small segment of silicon was inserted into the growth chamber and In was deposited for a certain period of time. The thickness of this In layer was then measured using a talystep from which a growth rate was inferred, assuming unity sticking coefficient for In. For subsequent growth of InSb epilayers the thickness was calculated by taking into account any change in the BEP of the indium flux. This method can introduce significant errors since there is no simple relationship between the BEP and incident flux, resulting from the non-ideal behaviour of the K-cells as mentioned previously. With the observation of RHEED intensity oscillations (discussed

later in this chapter) epilayer thicknesses were determined *in-situ* for each InSb layer grown.

The thickness, d, of $InAs_xSb_{1-x}$ was determined by measuring the growth rate, using identical In flux but on an InSb test layer and the composition, x, deduced from the ratio of the antimony to indium fluxes. Using these measurements d can be calculated from the following expression:

$$d = \frac{1}{2} [x\ LP_{InAs} + (1-x)LP_{InSb}] \cdot GR \cdot t \cdot 10^{-4}\ \mu m \qquad (5.1)$$

where GR is the growth rate in monolayers per second, LP is the lattice parameter and t is the growth period in seconds.

5.2.3 Data Recording

All RHEED patterns were recorded directly from the fluorescent screen using a 35mm camera. With HP5 film, exposure times of between 15 and 30 seconds were used depending on the quality of the patterns. RHEED oscillations were recorded by monitoring the intensity of the specular spot in the RHEED pattern. A lens was used to focus the specular spot onto the end of an optic fibre which in turn was connected to a photomultiplier tube. The output of the photomultiplier tube was fed to a x-t chart recorder via an amplifier. The incident beam energy was 12.5 keV and the angle of incidence was estimated to be about 2°.

5.3 RHEED Intensity Oscillations during the MBE Growth of InSb(001)

During the course of this research RHEED intensity oscillations were observed for the first time during the growth of InSb, providing direct evidence for layer-by-layer growth. This enabled accurate measurements of growth rate and incident beam fluxes to be made directly without the need for post-growth calibration techniques. Originally migration enhanced epitaxy [156] was used to grow relatively thin buffer layers of InSb from which RHEED oscillations were easily observed. It was thought that this method would produce a surface smooth enough to allow the observation of these oscillations. A much simpler approach and one that was subsequently adopted was to anneal the InSb substrates at a temperature of ~$390^{o}C$ for 30 minutes. Dosing the surfaces with one or two 5 seconds exposure to the In

flux after the anneal followed by re-annealing for a few minutes was often advantageous as indeed it is for GaAs [157]. RHEED oscillations were also observed after the growth of ~1/2 μm of InSb directly on a GaAs substrate.

Figure 5.4 shows a typical set of data recorded from the specular beam in the [110] azimuth using a flux ratio of J_{Sb4}/J_{In}= 1.75 and a growth rate of 0.77 ML/s. The substrate temperature was calibrated as described in the previous chapter and here T_T refers to the transition temperature at which the surface reconstruction changed from a c(4x4) to the so-called pseudo (1x3) during growth under Sb-rich conditions [52,150]. The flux ratios given are effective flux ratios and represent the ratio of the fluxes incorporated. These are equal to the incident flux ratios only if the sticking coefficient with respect to the incoming beams is unity.

A close examination of figure 5.4 reveals a comparatively narrow range of growth temperatures, 80°C centred around T_T, during which RHEED oscillations are observed. This temperature range was found to vary when the flux ratios were changed. Figure 5.5 shows the RHEED oscillations, as a function of substrate temperature, observed for a flux ratio of J_{Sb4}/J_{In}=1.02, a growth rate of 1.31 and recorded using the specular beam in the [110] azimuth. Under these conditions RHEED oscillations can clearly be observed at temperatures beyond T_T+60°C and below T_T-100°C. Figures 5.4 and 5.5 show that RHEED oscillations are at their strongest at substrate temperatures around T_T. Closer examination of figure 5.5 reveals a slight increase (9%) in growth rate with increasing temperature which is thought to be due to the re-evaporation of indium deposits in the vicinity of the substrate at higher growth temperatures thereby increasing the total indium flux incident on the growing surface. Another possibility considered is the transient behaviour of the In flux whenever the shutter is opened. However, there is not enough data available to substantiate this possibility.

At temperatures above T_T it was found that the amplitude of the RHEED oscillations became progressively smaller and harder to detect at high growth temperatures. This is most likely due to a change in growth mode from two-dimensional layer-by-layer growth to step propagation as reported for the growth of GaAs(001) [158,159]. At low growth temperatures the step density varies as a result of 2-dimensional nucleation whilst at high temperatures the arriving adatoms have sufficient mobility to ensure incorporation to step edges thus keeping a constant mean step density.

RHEED oscillations also became difficult to resolve at lower substrate temperatures. This is probably due to the less rapid diffusion of the free surface In atoms as the temperature is reduced. As a result, the average distance travelled by the In atoms before they combine with dissociated Sb_4 molecules decreases as the temperature is lowered. Ultimately, this leads to random aggregation of islands and hence a three-dimensional growth mode [160]. In addition, antimony is reported to have long surface residence lifetimes at low temperatures [52] which is expected to reduce further the average distance travelled by the free In atoms before being incorporated in the growing lattice. Indeed, the different ranges of temperature over which RHEED oscillations are observed in figures 5.4 and 5.5 may well be due to the different In atom surface lifetimes as a consequence of the different flux ratios used.

Figure 5.6 presents the results of varying the flux ratio. Here the Sb_4 flux was kept constant and the In flux was varied from 2.4×10^{14}atoms $cm^{-2}sec^{-1}$ to about 6.42×10^{14}atoms $cm^{-2}sec^{-1}$ using a constant substrate temperature of T_T-20°C. It can be seen that the RHEED oscillations become most pronounced as the flux ratio approaches unity. For flux ratios greater than about 2 the oscillations become harder to resolve. The appearance of RHEED intensity oscillations is therefore critically dependent on the flux ratio. The lower curve in figure 5.6 corresponds to growth under In-rich conditions, i.e. $J_{Sb4} < J_{In}$ and oscillations are caused by the arrival rate of Sb_4 since indium is now present in excess. On initiating growth, the surface reconstruction changed from a Sb-rich c(4x4) to an In-rich c(8x2). Using this curve the effective Sb_4 flux can be deduced from the period of oscillations although prolonged growth under these conditions rapidly degrades the surface morphology as indicated by the reduction in intensity of the RHEED pattern. In practice Sb_4 flux measurement is more easily made using a technique similar to that for As-induced oscillations [131]. In this method the InSb surface is dosed with about 10 monolayers of In before the antimony shutter is opened. The period of the Sb-induced oscillations then gives the effective Sb_4 flux. A typical plot of Sb-induced oscillations is shown in figure 5.7.

RHEED oscillations were also obtained from the [$\bar{1}$10] and the [010] azimuths, and at temperatures for which the RHEED pattern indicated a Sb-stabilised c(4x4) reconstruction they were observed in the integral and 1/2 order

features in the <110> azimuths as shown in figure 5.8. In addition, RHEED oscillations were observed after the growth of ~0.5 μm InSb grown on GaAs. Figure 5.9 shows a typical plot of In- and Sb-induced RHEED intensity oscillations obtained during the growth of InSb/GaAs. A systematic investigation of the phases and initial transients of the oscillations was not carried out since the position of the diffraction pattern on the screen moved whenever the magnetically actuated shutters were opened or closed.

In summary RHEED oscillations during the MBE growth of InSb(001) have been observed for the first time during the course of this study providing direct evidence that growth proceeds via a 2-dimensional layer-by-layer mode. These oscillations are strongly dependent on the flux ratio and substrate temperature; RHEED oscillations are strongest using a flux ratio close to unity at a substrate temperature around T_T. Growth rates and flux ratios can now be measured directly without the need for post-growth calibration techniques [154].

5.4 Layer Growth

This section describes the homo- and heteroepitaxial growth of narrow gap semiconductors and discusses their morphology in terms of the growth conditions. The results of a RHEED study on the initial growth stages of InSb on GaAs substrates will also be presented.

5.4.1 InSb

InSb epilayers were grown on InSb substrates (homoepitaxial growth) and on GaAs substrates (heteroepitaxy), the latter enabling the electrical properties to be studied without the need for substrate removal.

After argon ion sputtering and thermal annealing the InSb substrate exhibited an In-rich c(8x2) RHEED pattern as shown in figure 5.10a. The substrate is then ramped in 5 minutes to a temperature approximately equal to T_T, normally taken to be the value found for the previous InSb epilayer grown. During this period the main shutter is kept closed and the antimony shutter opened to stabilise the antimony flux. Figure 5.11 shows the large transient that exists whenever the K-cell shutter is opened. Once the substrate temperature has reached its setpoint the main shutter is opened. Immediately, the RHEED pattern changes from an In-rich c(8x2) to either the

c(4x4), figure 5.10b, or the so-called pseudo "(1x3)", figure 5.10c, depending on the substrate temperature. The temperature is then slowly varied at approximately 5 ^{o}C in 3 minutes with a 5 minutes waiting period, and the "system-measured" temperature at which the surface reconstruction changes from a c(4x4) to the "(1x3)" is monitored. The transition is taken to be the disappearance of the 4 fold symmetry in the [010] azimuth when the surface reconstruction changes from the Sb-stable c(4x4) to the "(1x3)". This temperature is referred to as the static transition temperature, T_T^s, estimated to be 390 ^{o}C and is used to calibrate the growth temperature. Initially the dynamic transition temperature, i.e. the transition temperature during layer growth, T_T, was monitored but because the substrate cannot rotate while carrying out RHEED observations this method introduces non-uniform layer growth across the substrate. By monitoring T_T^s no growth is actually taking place so eliminating this initial non-uniform layer. Once T_T^s has been found the substrate is annealed for 30 minutes at a temperature of T_T^s+20 ^{o}C to minimise further the damage introduced by argon ion sputtering.

For heteroepitaxial growth on GaAs a buffer consisting of ~1/2 μm undoped GaAs is grown on the substrate to provide a clean and smooth surface prior to the growth of the InSb epilayer. During this growth period the antimony cell is kept at 200 ^{o}C in order to keep the vapour pressure of antimony in the growth chamber as low as possible during GaAs growth. After buffer layer growth the substrate is cooled to a measured temperature of 300 ^{o}C before the As_4 flux is turned off. The antimony cell is then slowly ramped to its operating temperature and allowed to outgas for a period of 40 minutes. This time period also allows the residual pressure of As_4 in the growth chamber to be significantly reduced. This can be seen in figure 5.12 which shows a mass spectrum taken during the growth of the GaAs buffer layer and another just prior to the growth of the InSb epilayer. After outgassing, the In cell is set to the temperature required for growth and both the In and Sb shutters are opened keeping the main shutter closed. The fluxes are then allowed to stabilise in a time period of 15 minutes after which the substrate is ramped to a temperature estimated to be T_T. Once this temperature is reached the main shutter is opened and 10-15 minutes of InSb growth is completed before T_T^s is determined. Epilayer growth is restarted after the growth temperature is calibrated.

For the growth temperatures used during this study, homoepitaxial growth of

InSb was characterised by 2-dimensional nucleation, as monitored by RHEED. It has been reported that the surface morphology is dependent on the flux ratio and the substrate temperature [49]. All epilayers were grown using a flux ratio of $J_{Sb4}/J_{In} \cong 1.2\text{-}1.6$ and growth rates of between 0.7 and 1.1 monolayers per second. Systematic studies of surface morphology were not undertaken during this research, but Nomarski micrographs did indicate that the surface morphology was dependent on the growth temperatures for the flux ratios used. At temperature around T_T all epilayers appeared mirror shiny and featureless when grown under Sb-rich conditions as shown in the Nomarski micrograph of figure 5.13a. As the growth temperature was reduced, the surfaces became degraded, probably due to the increase in the residence lifetimes of antimony on the surface. This low migration of antimony over the surface can lead to the growth of InSb clusters and eventually to polycrystalline growth at low substrate temperature [49]. Figure 5.13b shows a the surface of an InSb epilayer grown at 240°C possibly indicating regions of polycrystalline growth. At low growth temperatures the morphology of the epilayer may be dependent on the growth rate. A careful study is therefore required to ascertain the lowest temperature at which InSb with good morphological properties can be grown. Figure 5.13 shows a Normaski micrograph of a sample grown under the c(8x2) In-rich surface reconstruction showing what are probably indium droplets as the predominant features. Prolonged growth under these conditions resulted in poor quality RHEED patterns.

5.4.2 Initial Stages of InSb/GaAs growth: A RHEED Study

This section presents the results of a RHEED study on the effects of the lattice mismatch on the initial stages of InSb layer growth on GaAs. The motivation for this study resulted from the need to grow high quality InSb layers on GaAs which could potentially lead to the fabrication of single chip integrated opto-electronic devices. Because of the large lattice mismatch involved the quality of the interface plays a crucial role in the use of this technologically important semiconductor for device purposes. The aim of this study therefore, was to gather information on the nucleation, growth and coalescence of InSb deposits on GaAs. In association with this work TEM studies were also carried out on the layers grown. This, together with the RHEED study, provided a complete description of the growth process [46].

The indium and antimony fluxes were calibrated using RHEED intensity oscillations during homoepitaxial growth. Layer thickness will be expressed in terms of monolayers (MLs) (1ML=3.24Å for InSb).

After the growth of ~1/2 μm undoped GaAs buffer the substrate was cooled to 300°C before the arsenic cell was closed off and cooled to 120°C. At this temperature RHEED indicated a c(4x4) surface reconstruction, figure 5.15a, corresponding to a chemisorbed layer of As [161]. This reconstruction remained when the substrate was heated to the InSb growth temperature but changed to a (1x3) reconstruction (or a c(2x6) reconstruction) as soon as the antimony shutter was opened, figure 5.15b. It is thought that this reconstruction change may be due to the chemisorption of Sb, or possibly a surface exchange reaction between As and Sb.

Figure 5.16 shows the RHEED patterns after the deposition of the equilavent of 1, 2, 3, 4 and 5 MLs respectively of InSb. After 1ML the pattern consisted of discrete spots characteristic of 3-dimensional growth. The RHEED patterns in the [110] and $[\bar{1}10]$ azimuths were qualitatively similar. Measurements indicated that, to within experimental error, the lattice spacing of the deposit was identical to that for bulk InSb. Lines of diffuse intensity were observed between the spots in the <111> directions together with some weak features due to the GaAs substrate. After the deposition of about 3MLs of InSb, distinct differences were seen between the [110] and $[\bar{1}10]$ azimuths. At this coverage, the [111] and $[1\bar{1}1]$ streaks in the $[\bar{1}10]$ azimuth disappeared. After the growth of 5MLs there was clear evidence that (113) and $(\bar{1}\bar{1}3)$ facetting in the $[\bar{1}10]$ direction was occurring as indicated by the "arrowheads" in the RHEED pattern. Although TEM results indicated the existence of $(\bar{1}11)$ and $(1\bar{1}1)$ facets these were not observed in the RHEED patterns although they could have been present but obscured by the $(\bar{1}11)$ and $(1\bar{1}1)$ streaks. From about 3MLs, streaks of diffracted intensity perpendicular to the shadow edge could also be seen in the RHEED patterns which were associated with diffraction from reconstructed InSb(001) surfaces.

Figure 5.17 shows RHEED patterns after the deposition of 8, 16, 36, 75 and 200 MLs of InSb respectively. The "arrowheads" due to the {113} facetting were only observed in the $[\bar{1}10]$ azimuth. As growth proceeded the nature of the diffraction process seemed to change from 3-dimensional, characterised by spots, to 2-dimensional, i.e. streaks after the deposition of about

36MLs, indicating appreciable diffraction from the top of the islands. The "arrowheads" associated with the facetting disappeared after the growth of about 150MLs which may suggest that the islands are starting to join together. The reconstructions of the (001) surfaces of the InSb islands shown in the RHEED patterns of figure 5.17 appear to be complicated but these can be interpreted as a mixture of the c(4x4) and the so-called "pseudo" or asymmetric (1x3) reconstructions. The growth temperature for this study was chosen to be ~370°C which corresponds to the temperature at which the transition between the c(4x4) and the "(1x3)" occurs.

In the coverage range 1-5 monolayers, the RHEED data indicated island growth for coverages as low as 1 ML which is inconsistent with a Stranski-Krastanov growth mode. Measurements on the RHEED patterns seemed to indicate complete lattice relaxation. At 5MLs coverage there are clear indications of island growth with the facetted sides being parallel to the ($\bar{1}$11), (1$\bar{1}$1), (113) and ($\bar{1}\bar{1}$3) planes as shown in figure 5.18. These planes are all Sb terminated consistent with the growth conditions, i.e. $J_{Sb4}/J_{In}>1$. By comparing the angular width of the RHEED features in the two orthogonal <110> azimuths, it can be inferred that the long axes of the islands are parallel to the [110] direction, consistent with the TEM results [36]. The observations made during the growth of InSb on GaAs, i.e. nucleation and the growth of facetted islands were also reported by Noreika *et al* [52] although no mention was made of the relative orientation of the facets. Similar trends were also observed during the growth of Ge on Si by Koide *et al* [45] and GaAs on Si by Charasse *et al* [47].

A simple calculation using the theory of Matthews and Blakeslee [162] indicates that the value for the critical thickness, is less than the thickness of a monolayer. As a result it would not be possible to grow a lattice matched monolayer of InSb on GaAs since the high interface energy would lead to island growth.

Other factors which could have led to island growth were considered. These included the growth temperature and surface contamination. Because the distance over which the surface adatoms can migrate is reduced at low temperature, this can lead to random aggregation of molecules and hence island growth. However, in this study the growth temperature used was such that layer-by-layer growth was occurring as demonstrated by the observation of well defined RHEED oscillations during homoepitaxial growth of InSb for

the same growth temperature. Hence the possibility of adatom surface mobility limiting growth can be discounted. On the other hand, carbon contamination is known to nucleate island growth and cause twinning in silicon homoepitaxy [163]. However, if a similar mechanism was to operate during the growth of InSb/GaAs epilayers the extent to which this was occurring is difficult to establish since independent experiments using AES showed no detectable accumulation of carbon during the timescales involved. Nevertheless the RHEED data confirmed the presence of {111} twinning, in the [110] azimuth as shown in figure 5.19, for some samples grown in the range 2-6 MLs, which may be related to contamination.

In summary therefore, the RHEED data suggest that the large lattice mismatch of 14.6% is the dominant factor in island formation and that the MBE growth of InSb on GaAs proceeds via a Volmer-Weber model in which the initial 3-D nucleation is followed by island coalescence and eventually to 2-D growth. The islands tend to have flat tops and sloping sides.

5.4.3 InAs

All InAs epilayers considered in this work were grown on GaAs. Buffer layers were first grown on the GaAs substrates as for InSb/GaAs. Afterwards the substrate was cooled in a beam of As_4, to the temperature required for InAs growth, which is between 475 ^{o}C to 500 ^{o}C. This temperature was calibrated by monitoring the GaAs oxide desorption temperature or the system measured temperature as the surface reconstruction changed from a GaAs(001) c(4x4) to a (2x4). Growth was initiated by opening the indium shutter and after 10-15 minutes of growth the growth rate was calibrated by measuring the period of RHEED oscillations. Figure 5.20 shows RHEED intensity oscillations against substrate temperature taken after the growth of about 0.3 μm of InAs on GaAs indicating the wide range of substrate temperature over which layer-by-layer growth occurs.

The initial stages of InAs/GaAs growth as observed by RHEED proceeded via the Stranski-Krastanov growth mode during which an initial 2-D nucleation was followed by a period of 3-D island growth. This is in agreement with studies made by other workers [67-69]. On initiation of growth the first few monolayers take up the strain energy associated with the 7.4% lattice mismatch. Once the critical thickness has been reached the epilayer relaxes and releases this strain energy through the generation of misfit

dislocations. During the initial 2D nucleation RHEED intensity oscillations were clearly visible, confirming a layer-by-layer growth mode.

The flux ratio used for InAs growth was between 2.0 and 3.0 and the growth rate varied from about 0.6 to 1.0 MLs^{-1}. The surface morphology of InAs epilayers grown at a substrate temperature of 475 ^{o}C under the As-stable (2x4) reconstruction were mirror shiny and featureless as indicated by the Normarski micrograph of figure 5.21. However, an epilayer grown at 500 ^{o}C showed two distinct regions; to the naked eye one part of the surface looked shiny while the other cloudy. Non-uniform flux distribution across the wafer was ruled out since the substrate was rotated during growth. The most likely explanation therefore, was a non-uniform temperature distribution across the wafer. Indeed, an examination of the reverse side showed that the In solder was unevenly spread over the Mo block. As a result part of the wafer, corresponding to the cloudy part, was in good thermal contact with the block while the shiny part was not. Figure 5.22 shows the Normaski micrograph of these two regions. It is thought that at high growth temperatures the arsenic flux is insufficient to replace the arsenic atoms that are preferentially lost due to an increase in the thermal decomposition of InAs. Kubiak *et al* [70] observed similar effects for InAs grown under As_4-deficient conditions. This suggest that the flux ratio used in this work for InAs growth is not large enough to replenish the preferential loss of arsenic atoms at growth temperatures above 475 ^{o}C.

5.4.4 InAsSb

$InAs_xSb_{1-x}$ epilayers were grown on GaAs substrates over the complete compositional range 0<x<1. In addition InAsSb epilayers were also grown lattice matched to GaSb. It was reported that the alloy composition and layer quality of $InAs_xSb_{1-x}$ was dependent on the substrate temperature, the flux ratio of Sb to In and the growth rate [81]. Yen and co-workers found that mirror shiny surfaces were obtained for $InAs_xSb_{1-x}$ films (x=0.4) grown on GaAs substrates using a growth temperature of 410 ^{o}C and a growth rate of 1 µm/hr [83]. In this study growth of InAsSb alloys on GaAs substrates has been carried using a growth rate of ~1 µm/hr and a substrate temperature of about 370 ^{o}C. This substrate temperature was chosen as a first step since the antimony flux was calibrated using a substrate temperature of 370 ^{o}C during InSb growth (see later). This would eliminate any change in the sticking coefficient of antimony which may result from a change in the

substrate temperature, thereby ensuring the required alloy composition is achieved. At this temperature it was also shown that the growth of both the end compounds, i.e InSb and InAs, occurs via a layer-by-layer growth process as demonstrated by the observation of RHEED intensity oscillations. The antimony flux is set relative to the indium flux to achieve the desired alloy composition. The arsenic flux on the other hand is supplied in excess at a beam equivalent pressure of around $6x10^{-6}$ mbar.

One of the major problem in the growth of this ternary alloy has been in controlling the alloy composition during growth. Previous workers have used the fact that antimony was incorporated preferentially to arsenic to control the crystal composition (see chapter 2). However it was also shown that the incorporation of antimony was dependent on the substrate temperature temperature when tetrameric group V sources are used [79]. It is important therefore, to obtain an accurate calibration for the antimony flux against cell temperature so that the alloy composition of InAsSb can determined accurately. The observation of RHEED oscillations allow this to be carried out to a great deal of accuracy. The Sb flux was calibrated using the RHEED oscillation technique as described in section 5.3. Although it was difficult to obtain Sb-induced oscillations for low cell temperatures, it was possible to obtain enough data to produce a calibration curve for the Sb incorporation rate as shown in figure 5.23. From a knowledge of the In flux as measured from the period of the In-induced RHEED oscillations, the antimony cell temperature was then deduced for the specified alloy composition using the relationship,

$$(1-x) = J_{Sb4}/J_{In} \quad (5.2)$$

The heteroepitaxial growth of InAsSb on GaAs involved the initial growth of a 1/2 μm undoped GaAs buffer followed by a period of about 10 mins growth of InAs. The aim of this InAs buffer is to reduce the effects of the lattice mismatch between the substrate and the epilayer. During the growth of lattice matched $InAs_xSb_{1-x}$ (x=0.91) on GaSb, a buffer layer comprising ~1/2μm undoped GaSb was grown prior to epilayer growth.

So far in this study, the growth of InAsSb is at a very early stage and as such the growth conditions have not as yet been optimised. Nevertheless, the layers grown, ranging from about 3 to 4.5 μm in thickness, do appear mirror shiny and featureless when viewed with the naked eye. However, examination

using a Nomarski microscope does indicate that the surfaces are far from smooth. Figure 5.24 shows the surface morphology for layers grown under identical conditions but with a variety of alloy composition. However, it is too early to suggest any correlation between the surface morphology and alloy composition.

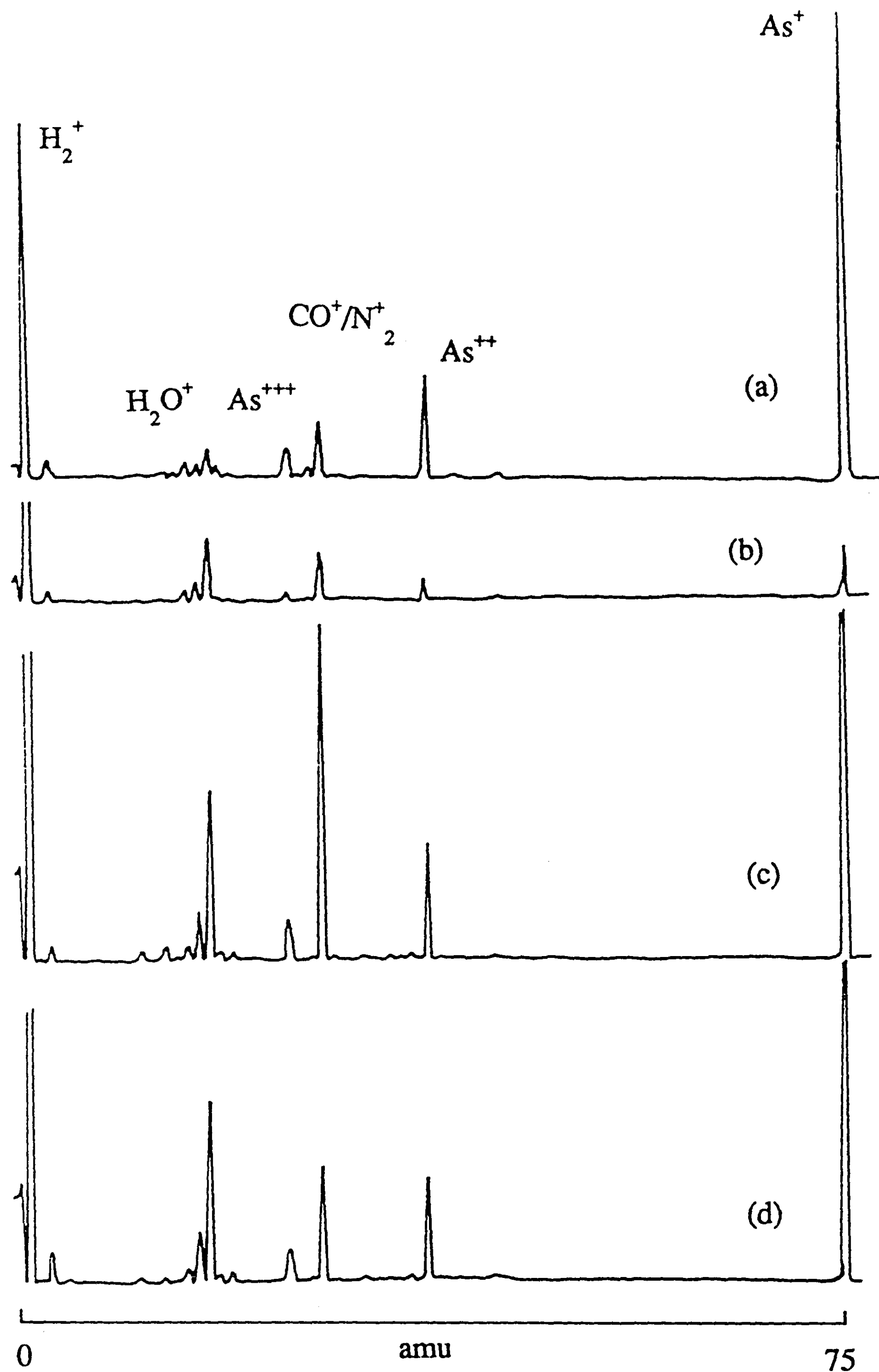

Figure 5.1 Mass spectra showing the gaseous species in the deposition chamber at various stages during the preparation for MBE growth of GaAs; (a) prior to cooling cryoshield, (b) after the cryoshield has been filled with nitrogen, (c) K-cells including Si at their outgassing temperature and (d) K-cells at the temperature used for growth.

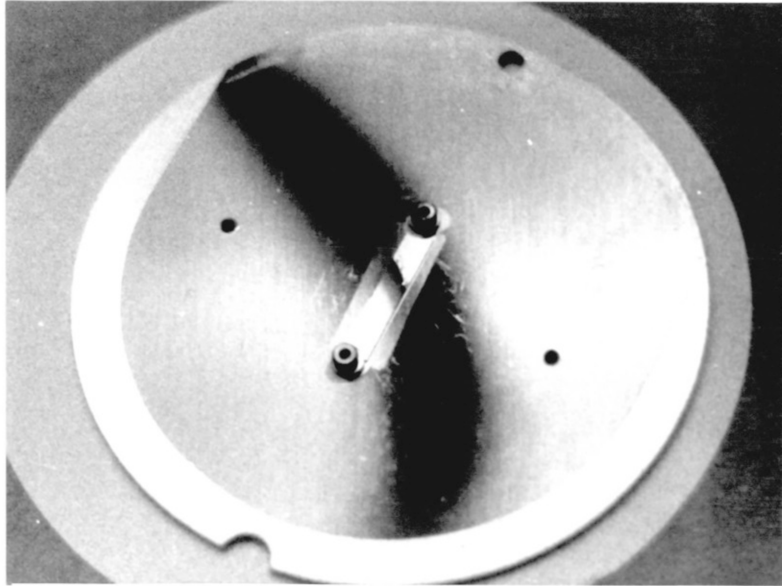

Figure 5.2 Non-uniform distribution of antimony flux. Sb was deposited onto a cold piece of silicon with the substrate rotation turned off.

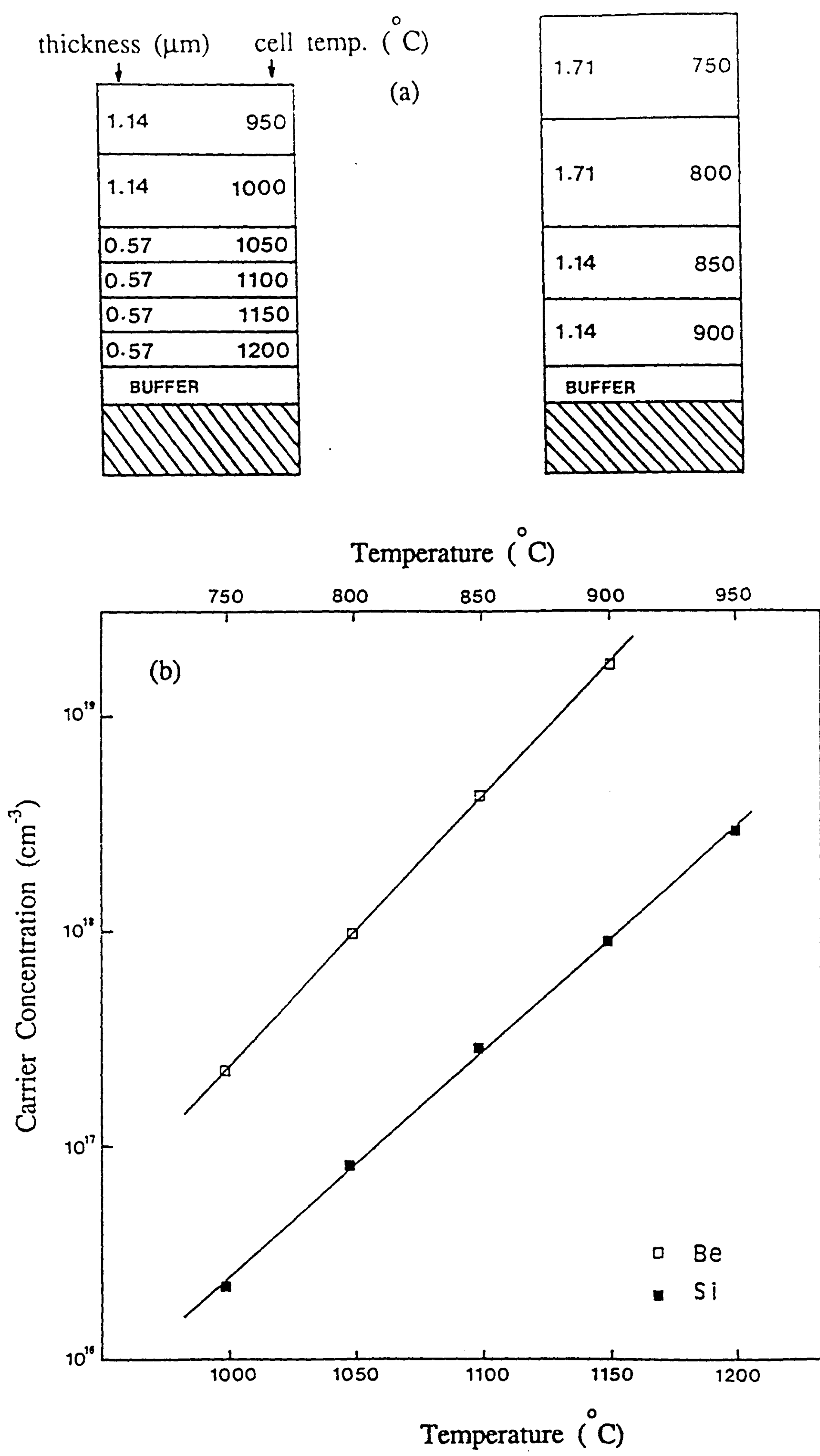

Figure 5.3 (a) Staircase doping profiles of GaAs for calibration of dopant fluxes. (b) Calibration curves for the Si and Be cells obtained from the results of C-V profiling carried out on the samples in (a).

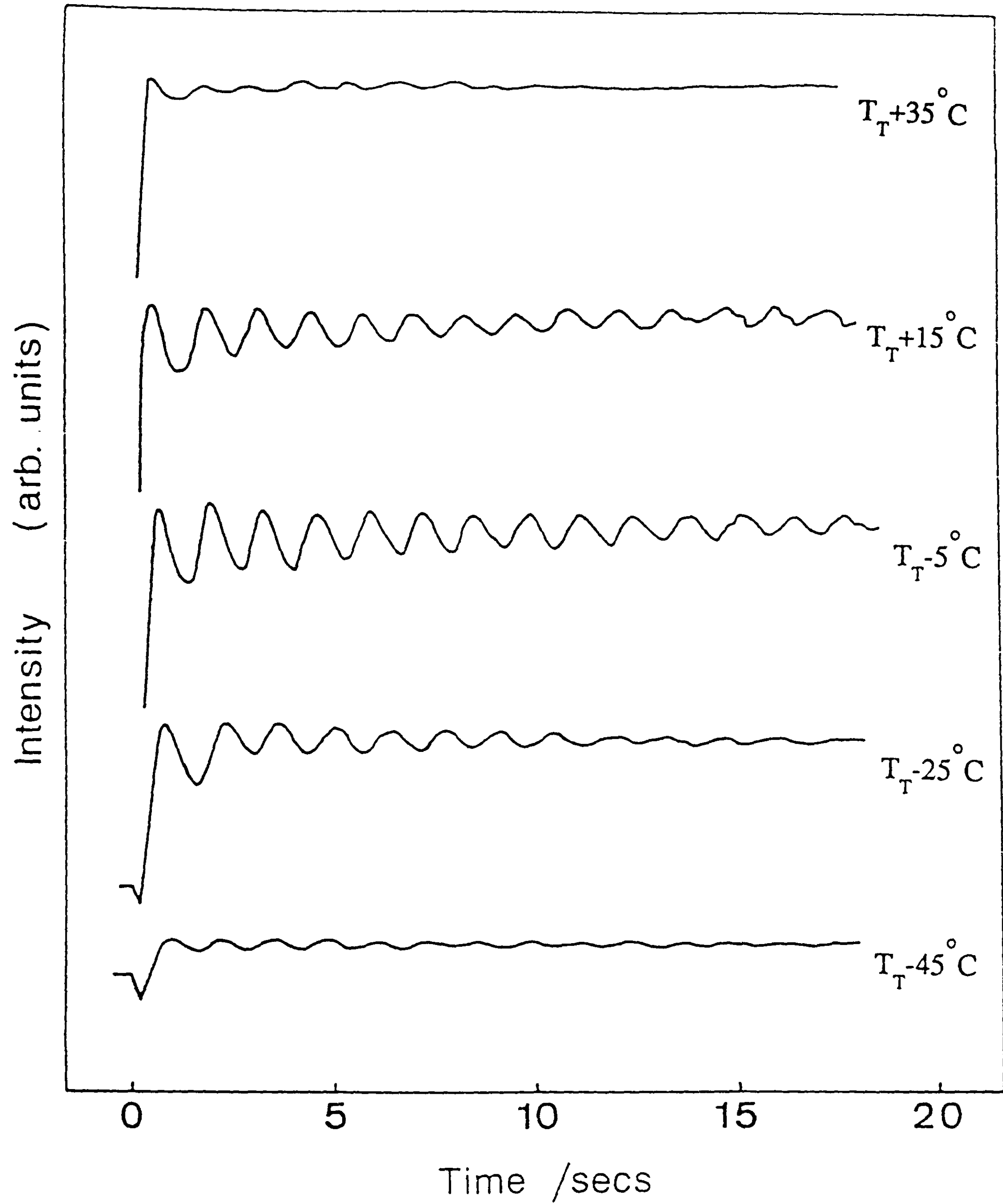

Figure 5.4 RHEED intensity oscillations from InSb(001) as a function of substrate temperature recorded from the specular spot in the [110] azimuth using a flux ratio of J_{Sb4}/J_{In}=1.75 and a growth rate of 0.77 ML/s.

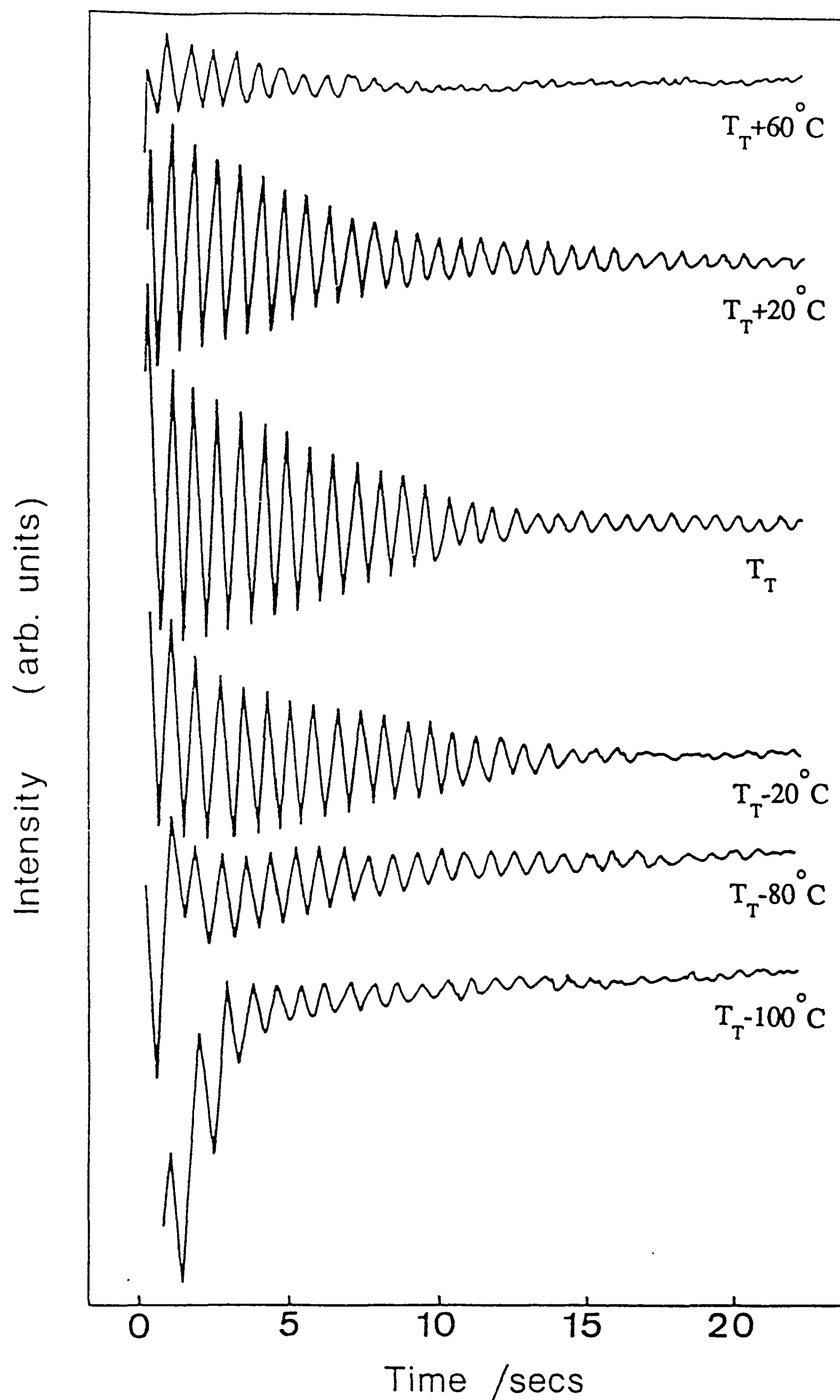

Figure 5.5 RHEED oscillations from InSb(001) as a function of substrate temperature recorded for a flux ratio of 1.02 and a growth rate of 1.31 ML/s.

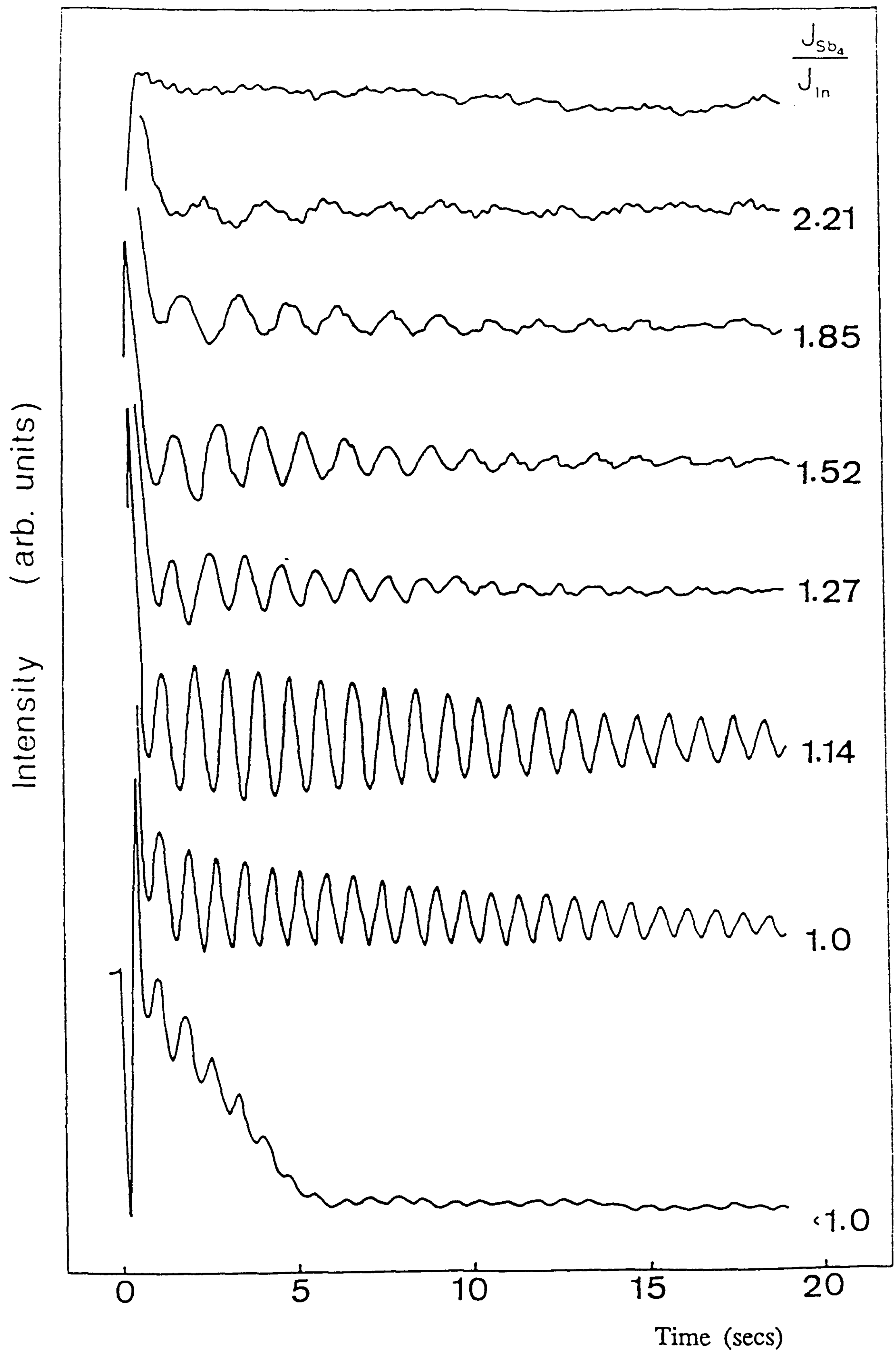

Figure 5.6 RHEED intensity oscillations recorded from the specular spot in the [110] azimuth as a function of flux ratio using a constant substrate temperature of T_T-20°C.

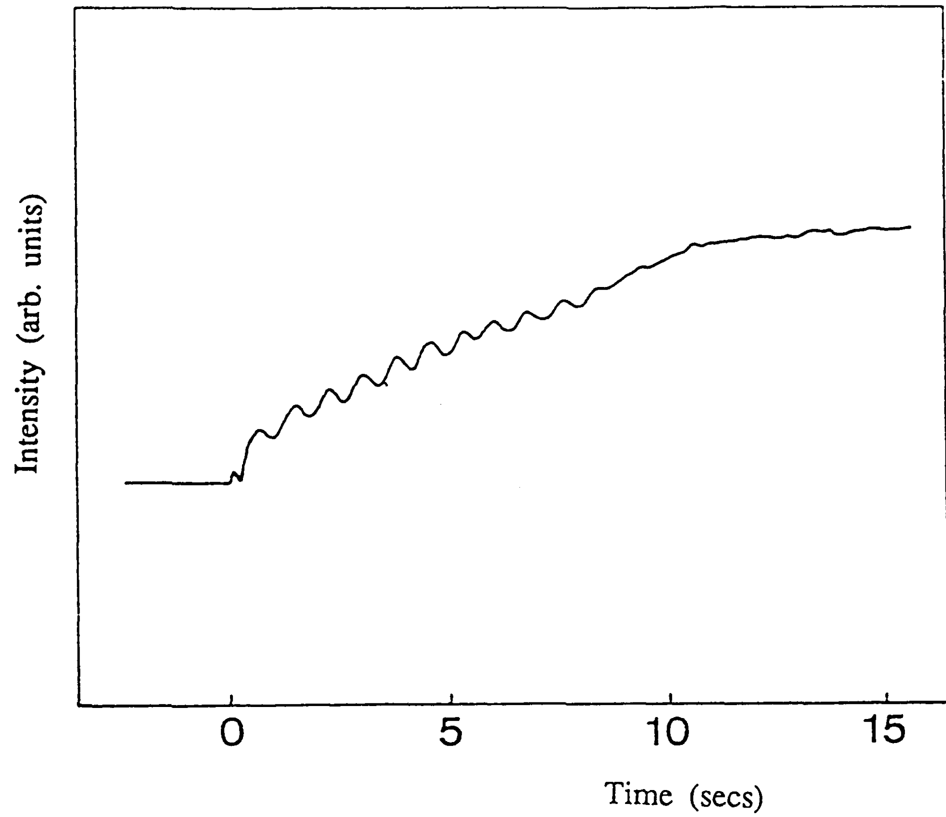

Figure 5.7 Sb-induced oscillations from InSb(001) recorded in the [110] azimuth following the deposition of the equivalent of about 10 MLs of In onto the InSb surface at a substrate temperature of T_T-20°C.

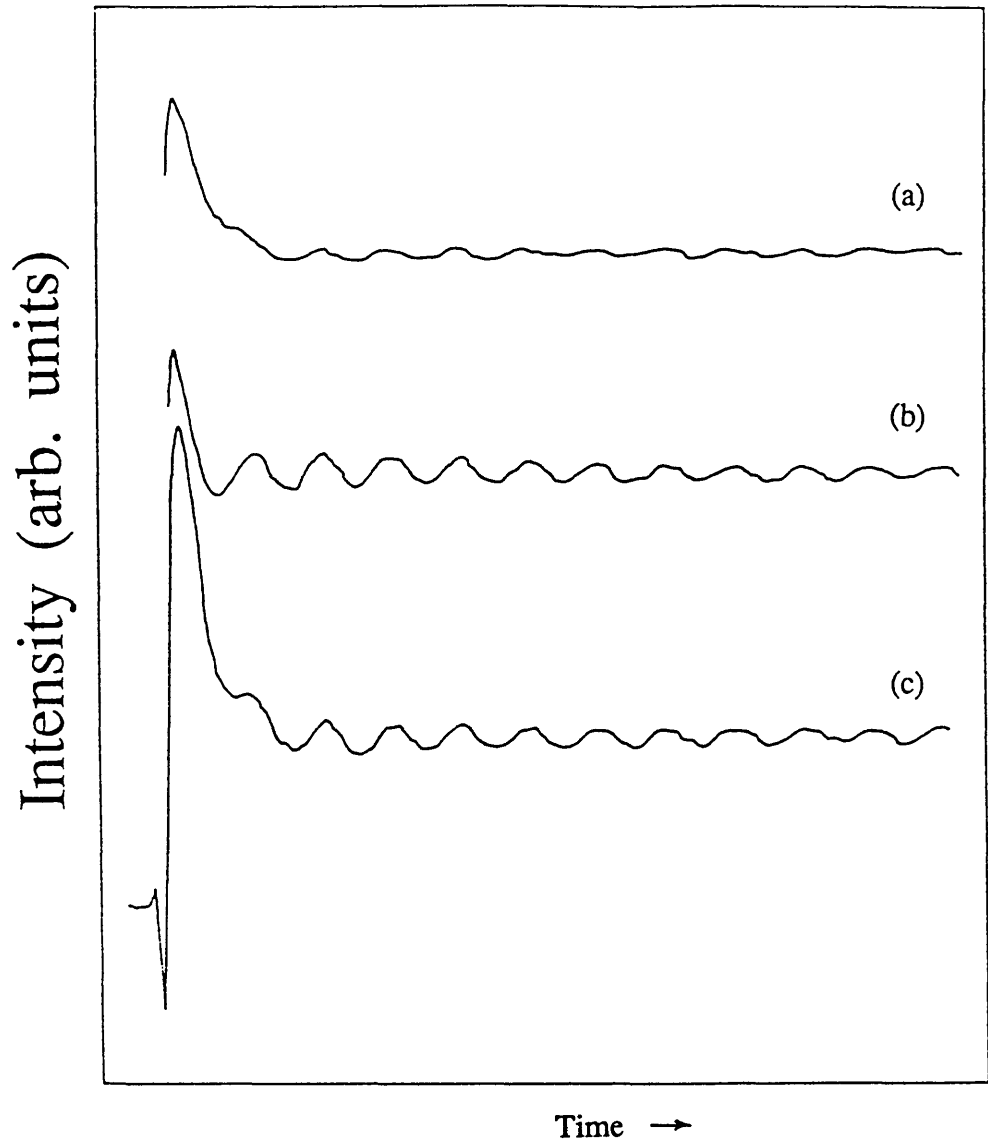

Figure 5.8 Typical plot of RHEED oscillations obtained from the (a) the integral order feature, (b) the 1/2 order features and (c) the specular spot on the c(4x4) surface reconstruction in the <110> azimuth.

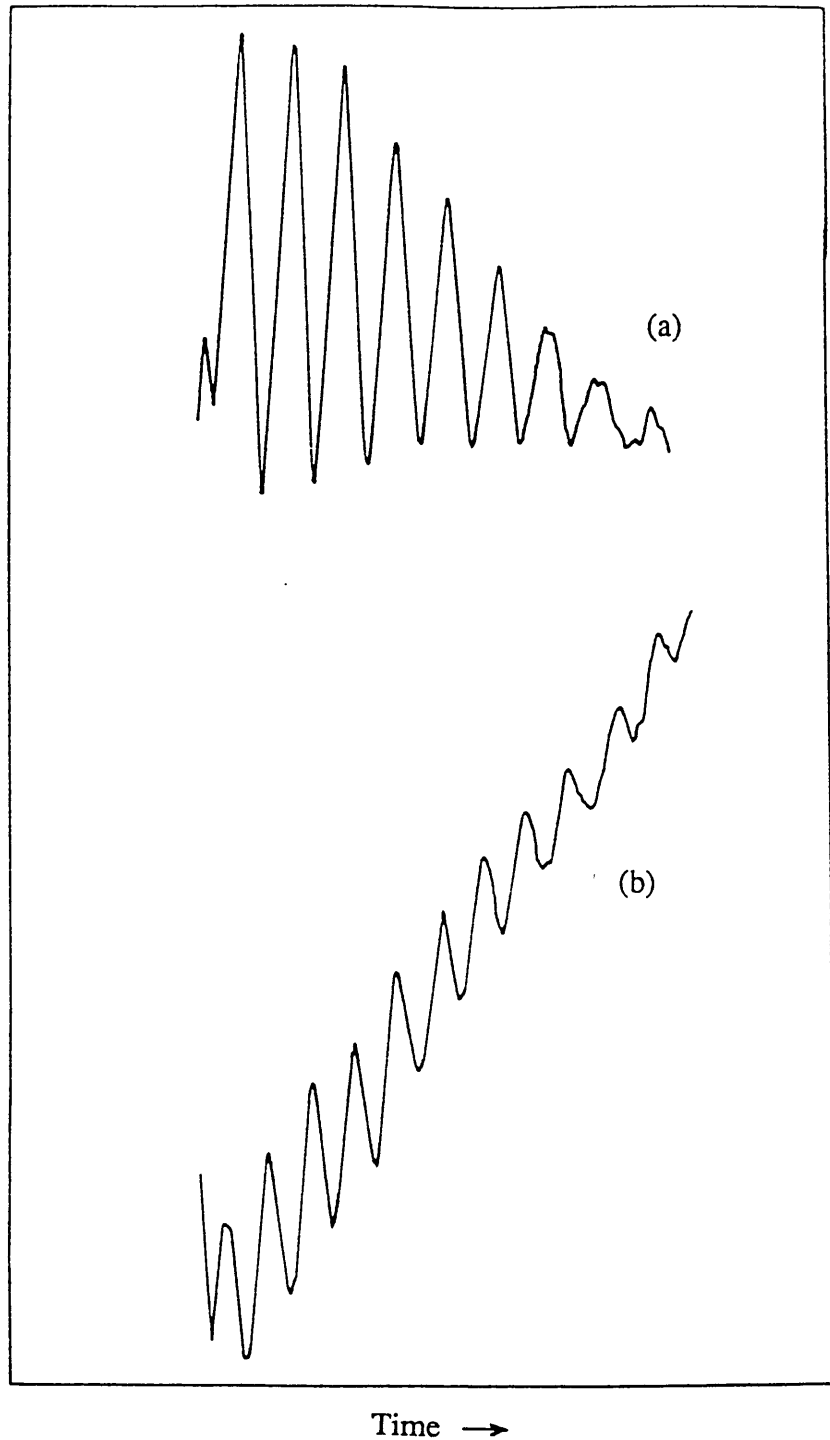

Figure 5.9 A typical plot of RHEED intensity oscillations observed in the <110> azimuth after the growth of 1/2 μm InSb on GaAs. The substrate temperature was T_T-20 ^{o}C; (a) In-induced and (b) Sb-induced oscillations.

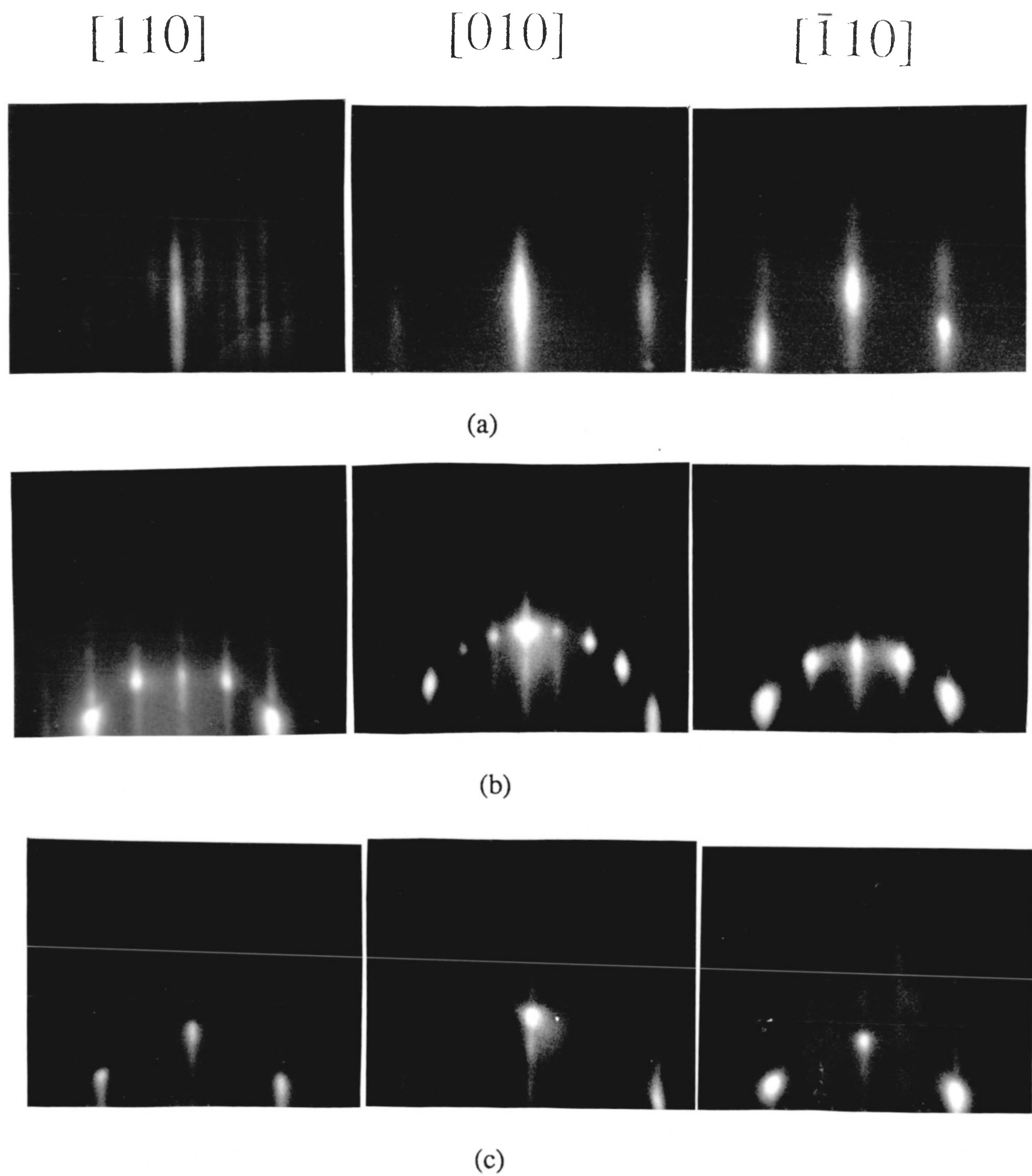

Figure 5.10 RHEED patterns taken in the [110], [010] and [$\bar{1}$10] azimuths showing (a) the In-rich c(8x2) reconstruction obtained from an InSb surface after argon ion cleaning, (b) Sb-stabilised c(4x4) reconstruction and (c) the so-called pseudo or asymmetric (1x3) reconstruction obtained at high substrate temperature.

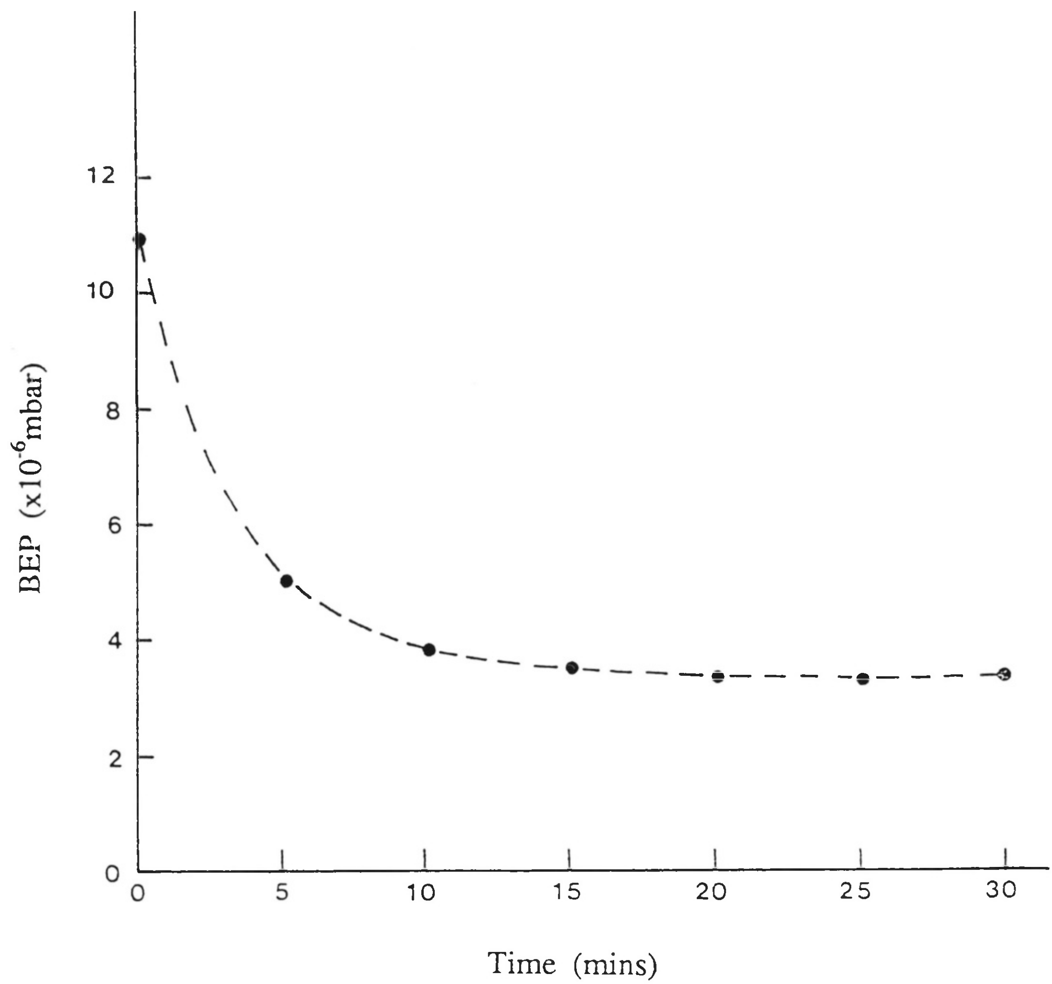

Figure 5.11 Variation with time of the beam equilavent pressure of the antimony flux after opening the shutter. This shows flux stabilisation is achieved after about 15 minutes from the time the antimony shutter is opened.

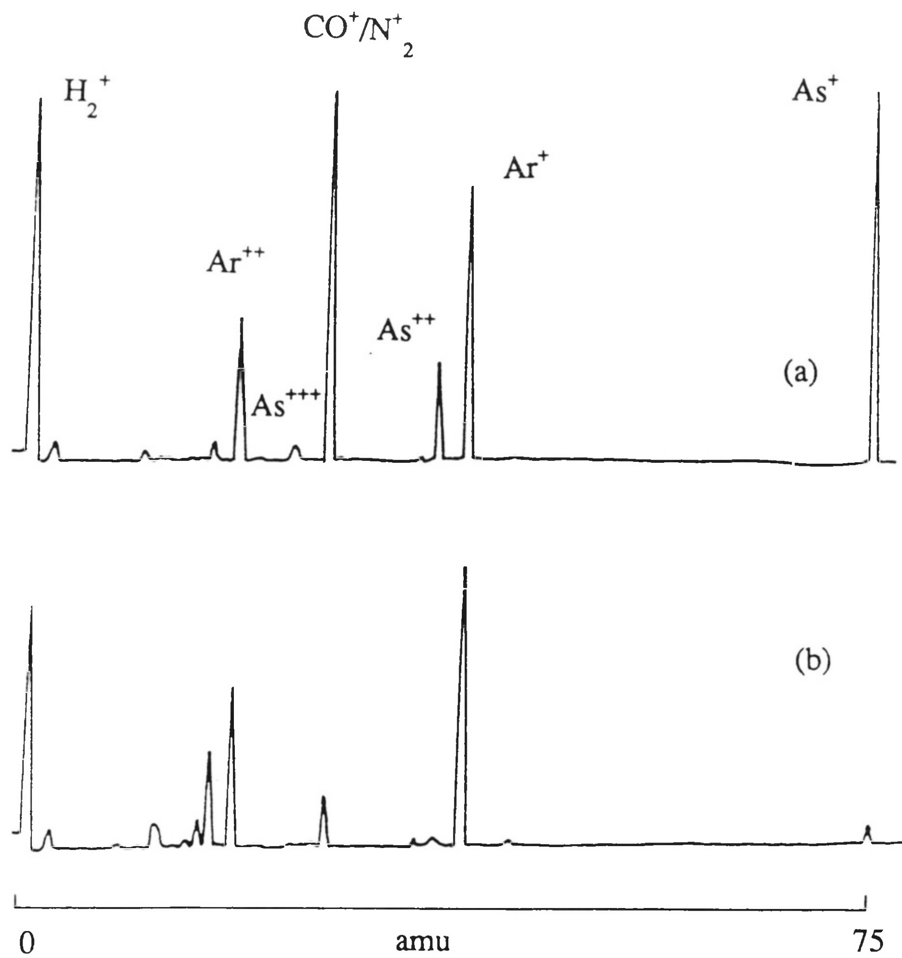

Figure 5.12 Mass spectrum taken (a) during the growth of a GaAs buffer layer and (b) just prior to the growth of InSb/GaAs, 40 mins after the arsenic cell has been shuttered off. Note the reduction in the peaks associated with As.

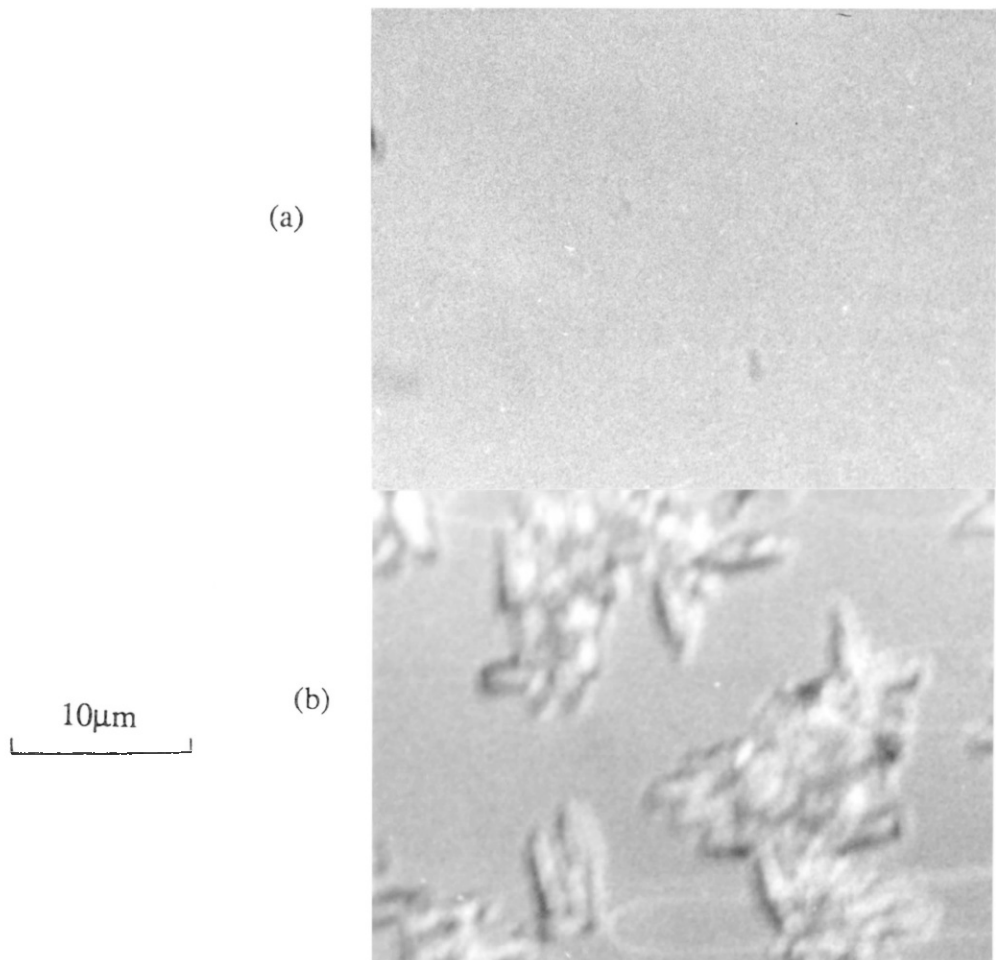

Figure 5.13 Normarski micrographs of (a) InSb surface grown under Sb-stabilised conditions at a temperature of 340°C, (b) InSb surface grown at 240°C at a growth rate of about 1 ML/s.

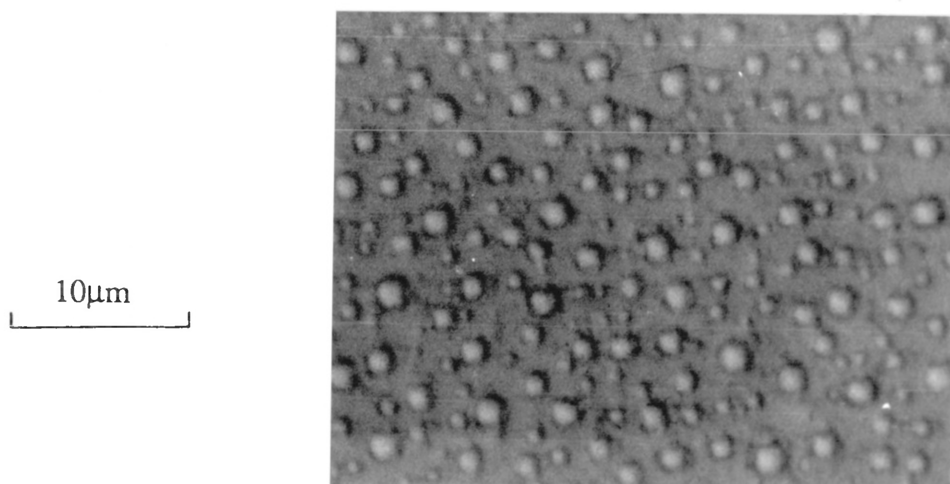

Figure 5.14 Surface morphology of InSb grown under the In-rich c(8x2) reconstruction.

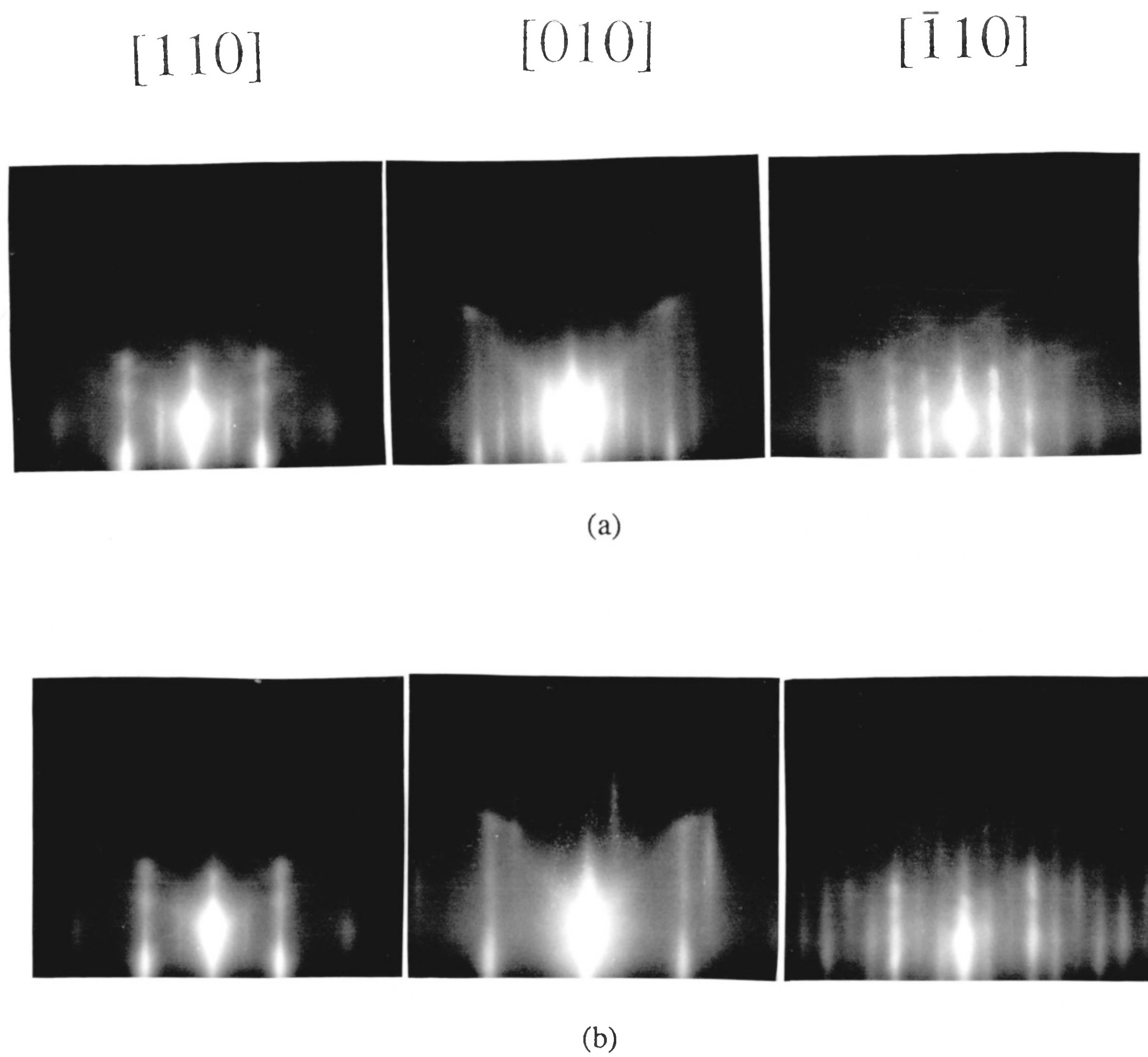

Figure 5.15 RHEED patterns prior to the growth of InSb on GaAs showing the (a) GaAs(001)c(4x4) As-stabilised reconstruction, (b) symmetric (1x3) reconstruction obtained after exposing the GaAs c(4x4) surface to a flux of antimony.

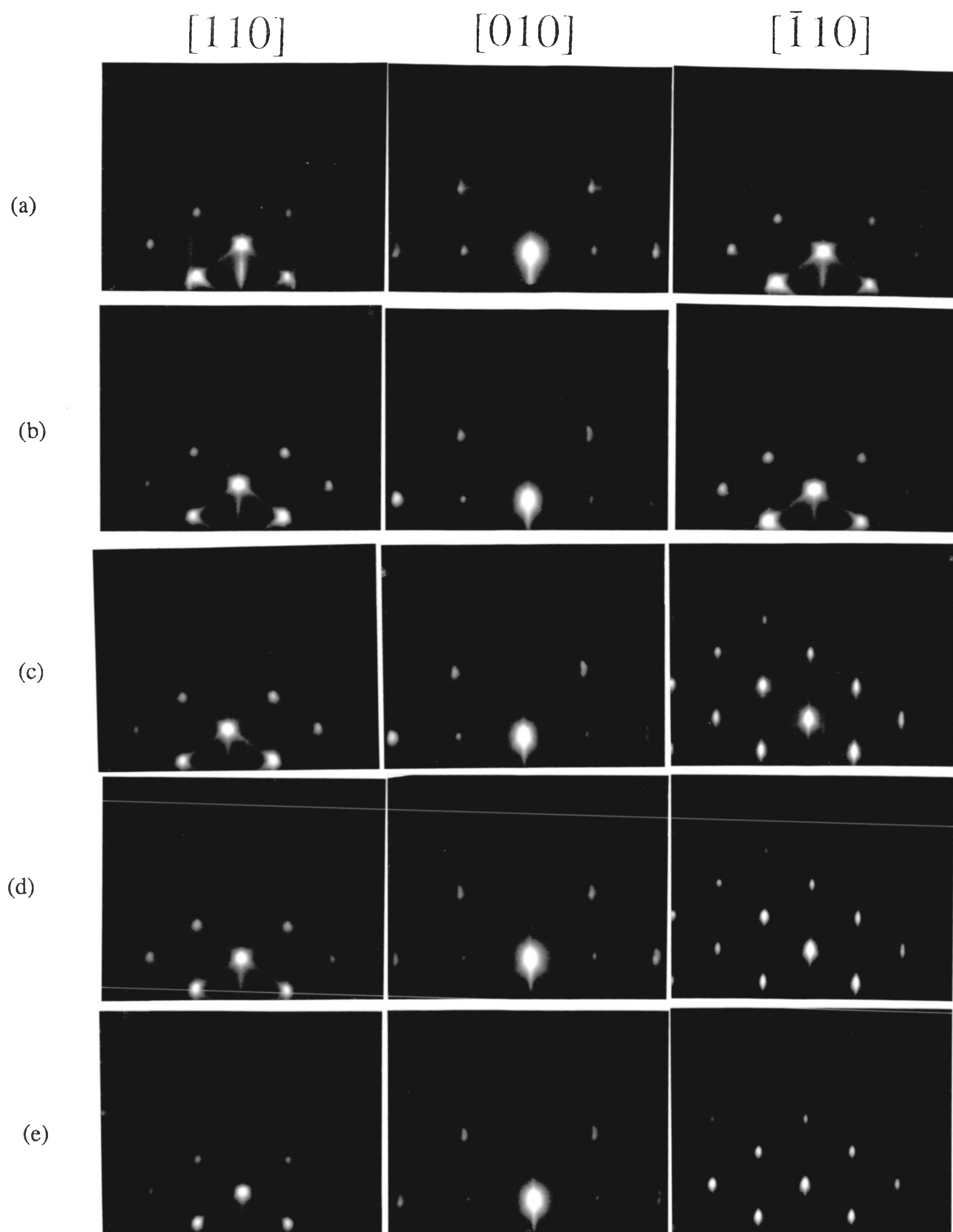

Figure 5.16 RHEED patterns taken in the [110], [010] and [$\bar{1}$10] azimuths during the initial stages of InSb grown on GaAs(001); (a) 1 ML (b) 2 ML (c) 3 ML (d) 4 ML (e) 5 ML.

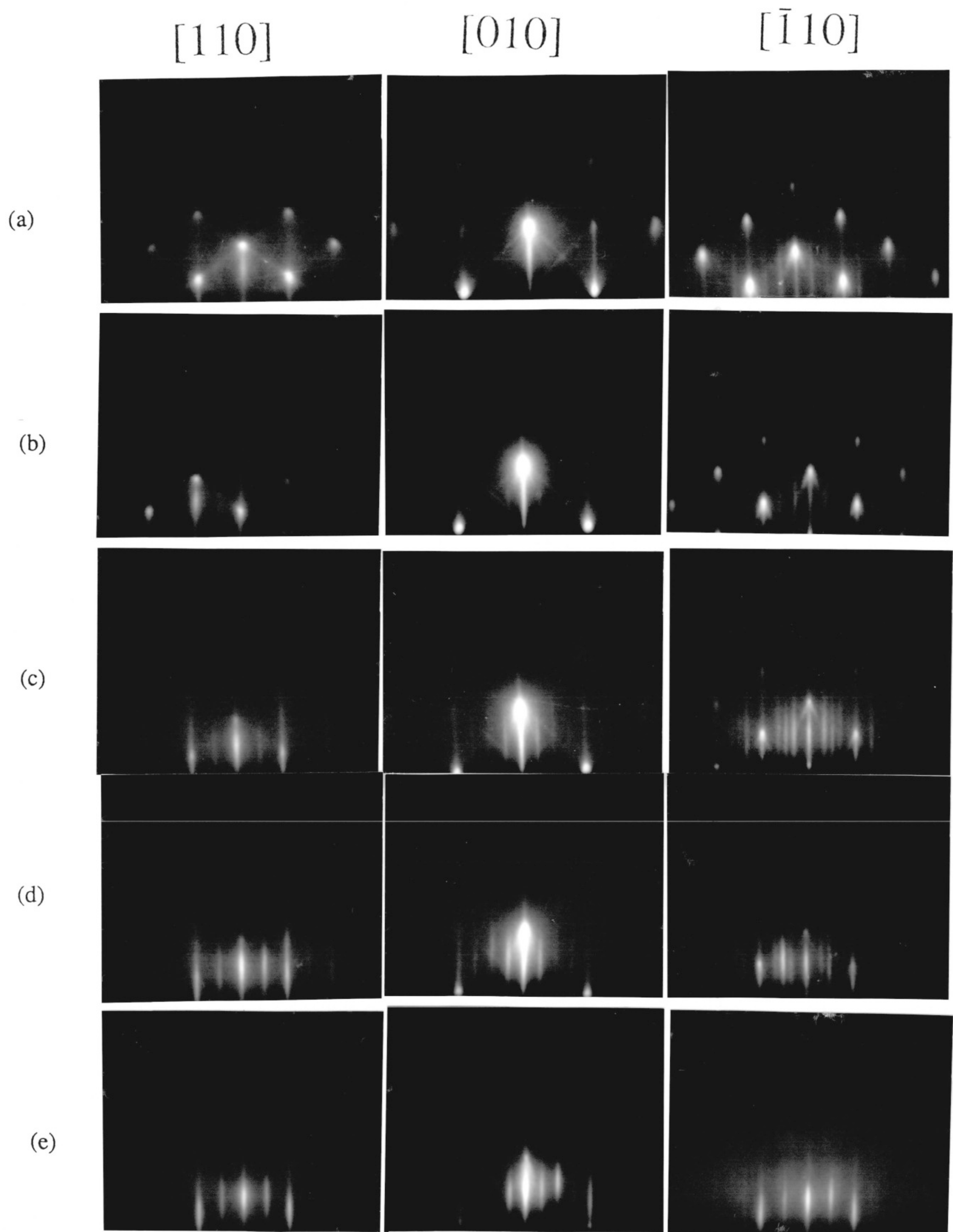

Figure 5.17 RHEED patterns after the growth of (a) 8 ML (b) 16 ML (c) 36 ML (d) 75 ML (e) 200 ML of InSb on GaAs.

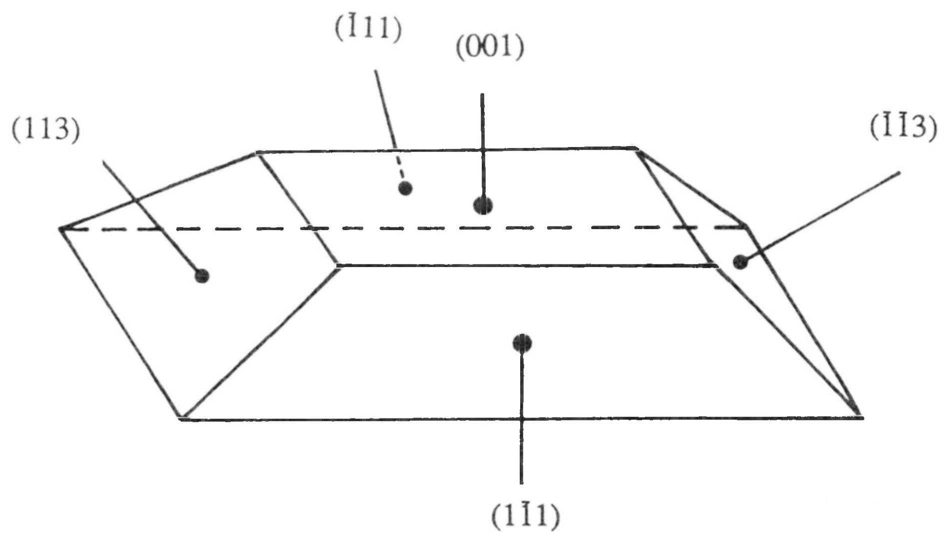

Figure 5.18 Relative orientation of the sides of the islands as they occur during the initial stages of the heteroepitaxial growth of InSb on GaAs.

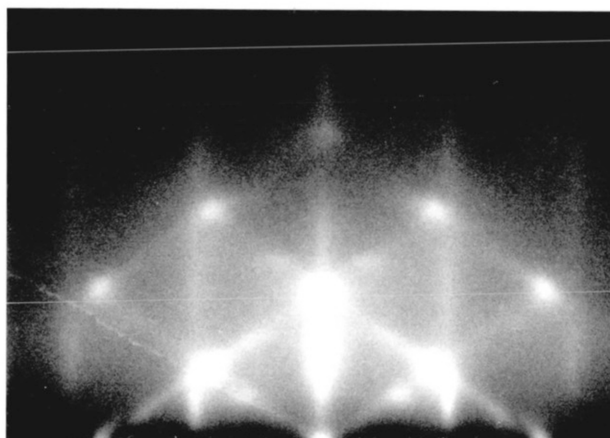

Figure 5.19 RHEED pattern showing evidence of (1̄11) and (11̄1) twinning in the [110] azimuth observed during the growth of some InSb/GaAs samples.

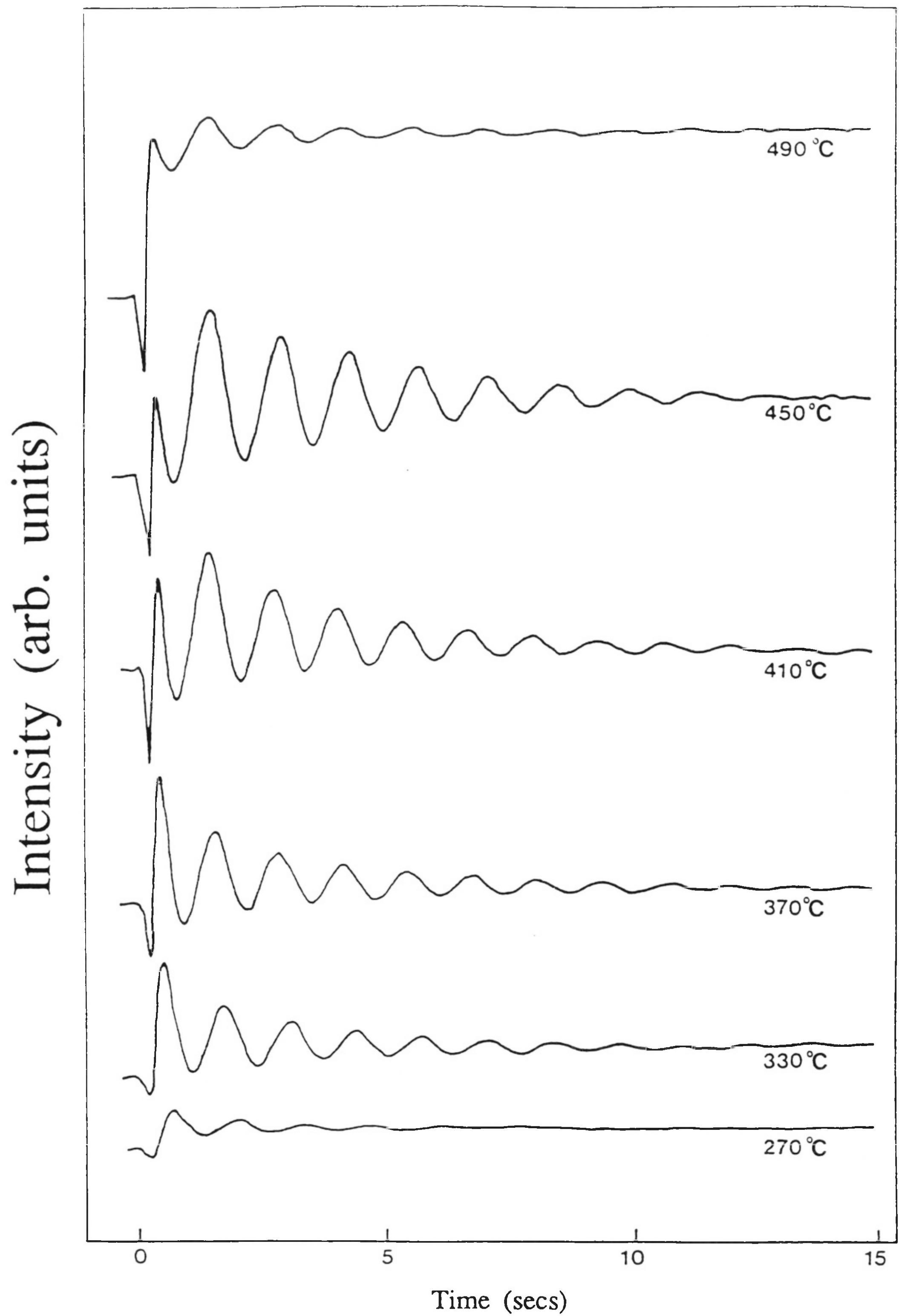

Figure 5.20 RHEED intensity oscillations as a function of substrate temperature obtained after the growth of ~1/3 μm of InAs on GaAs. The oscillations were recorded from the specular spot in the [010] azimuth.

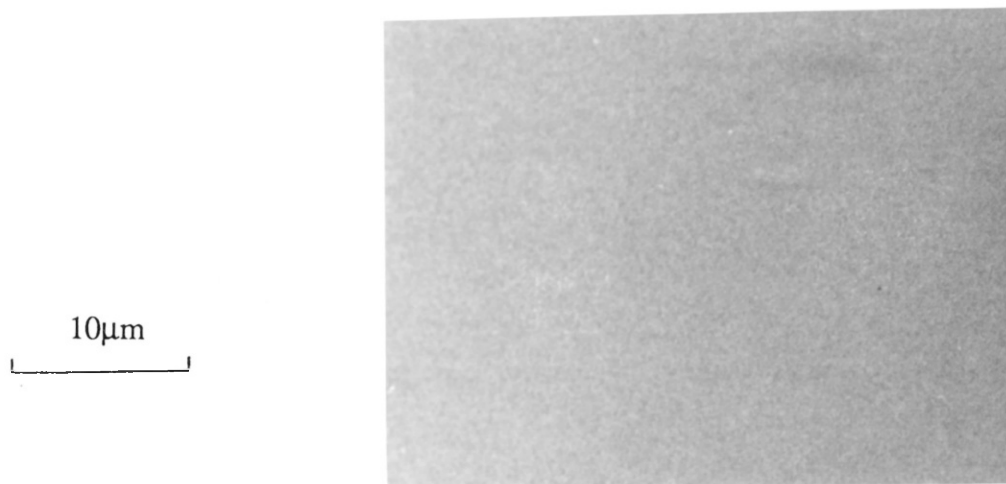

Figure 5.21 Surface morphology of InAs grown under As-rich conditions at a substrate temperature of 475°C.

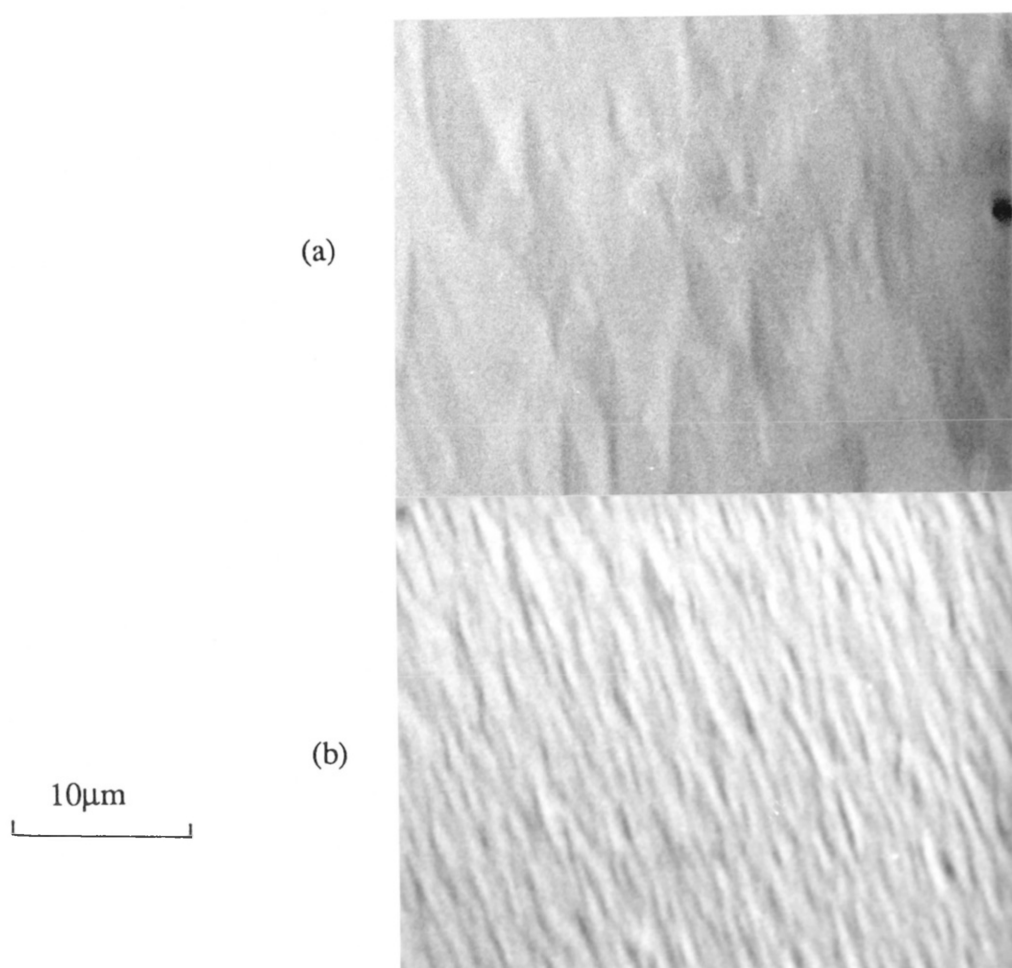

Figure 5.22 Nomarski micrographs of the surface of an InAs sample grown at 500°C showing two regions which to the naked eye appeared (a) shiny, (b) cloudy.

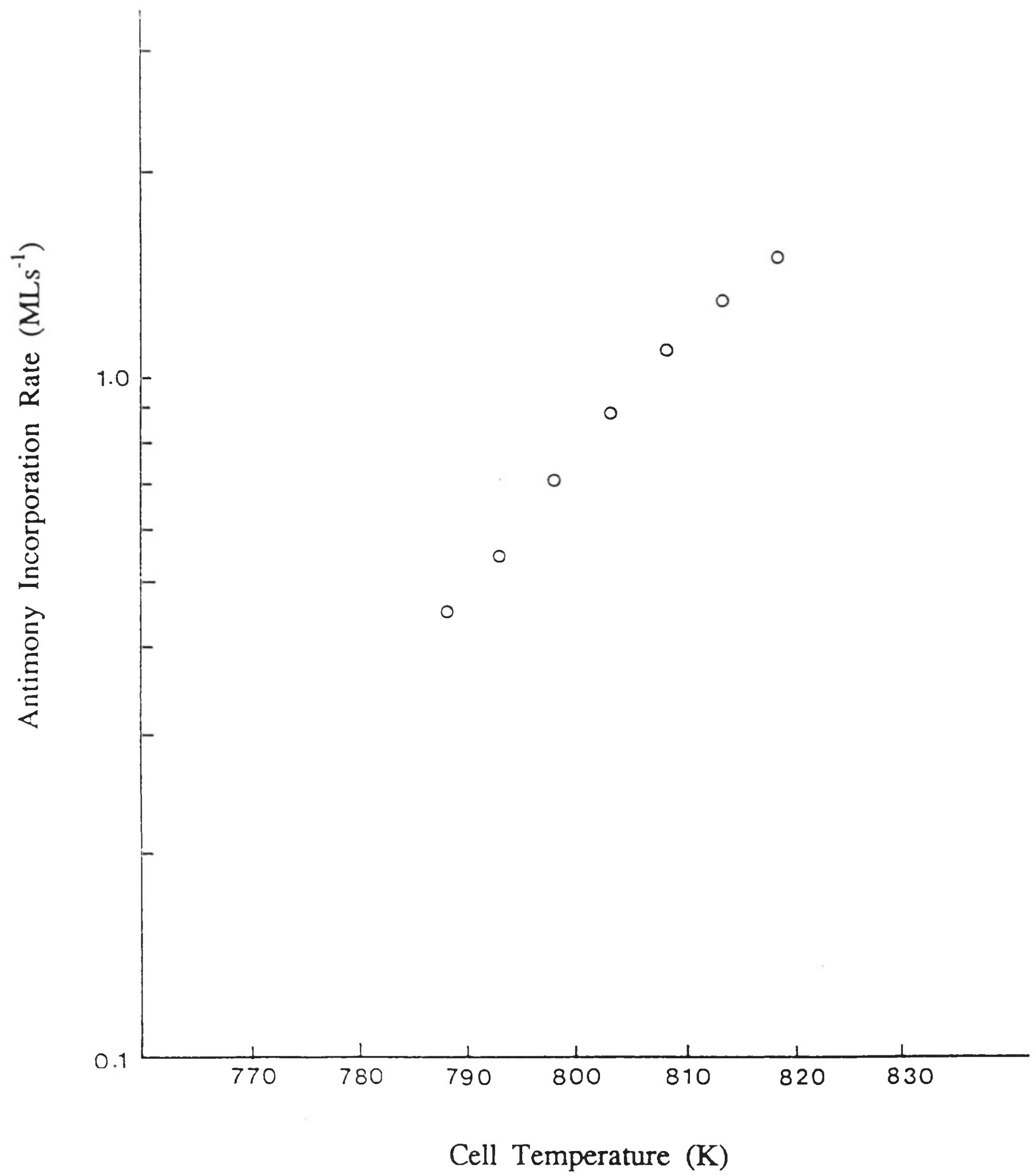

Figure 5.23 The variation of antimony incorporation rate against antimony cell temperature during the growth of InSb as deduced from Sb-induced RHEED intensity oscillations.

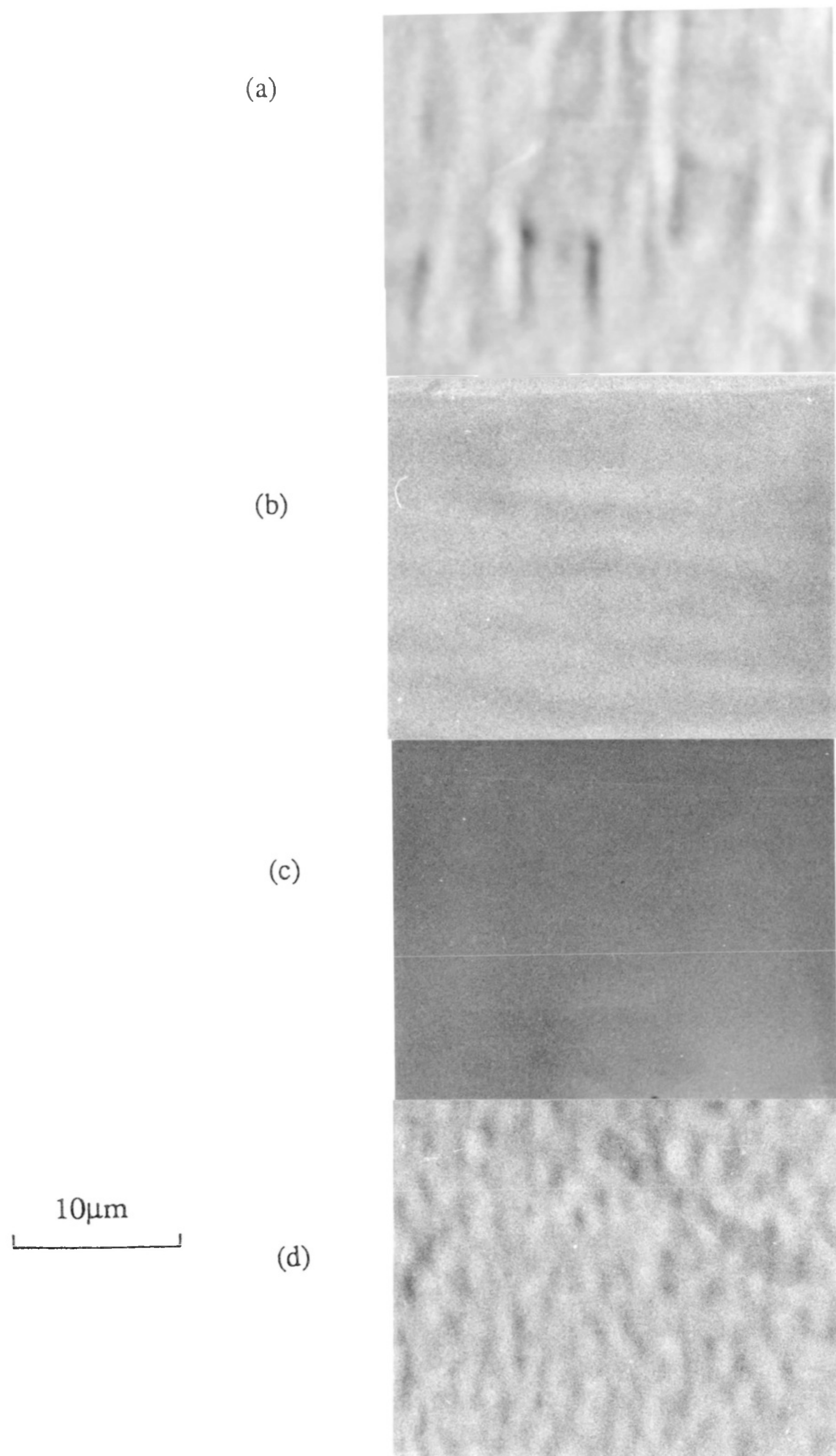

Figure 5.24 Surface morphology of $InAs_xSb_{1-x}$ epilayers grown at a constant substrate temperature of 370 ^oC. (a) x=0.2, (b) x=0.4, (c) x=0.6, (d) x=0.8.

CHAPTER 6 ELECTRICAL CHARACTERISATION OF SEMICONDUCTORS: THEORETICAL AND PRACTICAL CONSIDERATIONS

6.1 Introduction

Electrical characterisation of epitaxial layers provides the crystal grower with considerable information about the purity of such layers. This information is essential for the growth of high quality semiconductor materials as it allows the output of the MBE machine to be monitored continuously. In this study, the III-V semiconductors described in the previous chapter are characterised using Hall measurement, magnetoresistance and Shubnikov-de Haas techniques.

Hall measurement is an extremely common characterisation technique as analysis of the Hall coefficient combined with resistivity measurements enables the free carrier density and mobility to be extracted. The variation with temperature of the Hall coefficient can also be used to determine the energy gap of the material and the impurity activation energy involved. On the other hand the mobility-temperature variation can be used to determine the nature of the scattering mechanisms. It will be shown in section 6.3 that the Hall coefficient $R_H = r_H/ne$. Because scattering is energy dependent, r_H and hence R_H will depend on the magnetic field. At high fields the Hall scattering factor approaches unity. At low magnetic fields this factor is $\cong 315\pi/512$ for ionised impurity scattering and $3\pi/8$ for acoustic phonon scattering. It therefore follows that the carrier concentrations deduced from Hall measurements, i.e. using $n=1/R_He$ in the low field regime can be in error by as much as 100% if ionised impurity scattering limits the mobility. Other scattering mechanisms introduce smaller but still significant errors.

Magnetoresistance measurements can provide information on the existence of multiple carriers and multilayer conduction (transverse magnetoresistance) or electrical inhomogenieties within the material (longitudinal magnetoresistance). An analysis of the period of Shubnikov-de Haas oscillations provides a direct and accurate measurement of the free carrier concentration. The size and shape of the Fermi surface can also be determined from the dependence of the oscillation period on the orientation of the magnetic field.

The purpose of this chapter therefore, is to present some of the theory

behind the methods used for the electrical characterisation of the semiconductors grown. The practical aspects of the measurement techniques will also be given.

6.2 Carrier Transport in Semiconductors

Charge carriers in free space are accelerated when acted upon by an electric field. However, in a solid, because of collisions with impurities, lattice imperfections and phonons, these charge carriers are maintained in a steady state with velocity, v_d, called the drift velocity. The equation of motion for the carriers in an electric field is given by,

$$d(mv_d)/dt = q\mathcal{E} - mv_d/\tau \tag{6.1}$$

where m is the mass of the carrier having charge q, and τ is the momentum relaxation time or the time between collisions. The term mv_d/τ describes the 'friction' which the carriers experience as they drift through the crystal. In the steady state, equation (6.1) reduces to,

$$v_d = q\mathcal{E}\tau/m \tag{6.2}$$

If in a constant field $\mathcal{E}$ there are n electrons per unit volume with velocity v_d, the electric current density will be given by,

$$\mathbf{J} = nqv_d = nq^2\tau\mathcal{E}/m \tag{6.3}$$

The electrical conductivity σ is defined as $\mathbf{J} = \sigma\mathcal{E}$, so that

$$\sigma = nq^2\tau/m \tag{6.4}$$

From (6.2) the drift velocity is proportional to the electric field, i.e.

$$|v_d| = \mu|\mathcal{E}| \tag{6.5}$$

where $\mu = |q|\tau/m$ is called the drift mobility. It follows therefore, that

$$\sigma = nq\mu \tag{6.6}$$

The above equation for σ takes into account only one type of carrier. If

however, both electrons and holes are present the equation can be modified such that

$$\sigma = ne\mu_e + pe\mu_h \tag{6.7}$$

where μ_e and μ_h are the mobilities of the electrons and holes respectively. n and p are the concentration of electrons and holes.

6.2.1 Derivation of the Conductivity Tensor

In performing Hall measurements it is generally assumed that the current is proportional to the electric field at all points in the sample for small values of electric field. If this is the case then **J** and $\mathcal{E}$ are related by the conductivity tensor, i.e

$$\mathbf{J} = \sigma.\mathcal{E} \tag{6.8}$$

When a uniform magnetic field **B** is applied to a semiconductor the Lorentz force acting on an electron having a charge q = -e is given by,

$$\mathbf{F} = -e(\mathcal{E} + \mathbf{vxB}) \tag{6.9}$$

The classical equation of motion for the electron will then be

$$mdv/dt = -e(\mathcal{E} + \mathbf{vxB}) - mv/\tau \tag{6.10}$$

Let $\mathbf{B} = (0,0,B_z)$ and $\mathcal{E} = (\mathcal{E}_x,\mathcal{E}_y,0)$, i.e. the magnetic field is applied perpendicular to the electric field. Equation (6.10) becomes,

$$mdv_x/dt = -e\mathcal{E}_x - ev_yB_z - mv_x/\tau \tag{6.11a}$$
$$mdv_y/dt = -e\mathcal{E}_y + ev_xB_z - mv_y/\tau \tag{6.11b}$$
$$mdv_z/dt = -mv_z/\tau \tag{6.11c}$$

At steady state the left hand side of the above equations is equal to zero. Therefore,

$$0 = ne^2\tau\mathcal{E}_x/m + ne\omega_c\tau v_y + nev_x \tag{6.12a}$$
$$0 = ne^2\tau\mathcal{E}_y/m - ne\omega_c\tau v_x + nev_y \tag{6.13b}$$

where $\omega_c = eB/m$ and is the cyclotron frequency. But since $\mathbf{j} = -nev$ and $ne^2\tau/m$ is the conductivity at zero magnetic field, σ_o, we have

$$j_x = \sigma_o \mathcal{E}_x - \omega_c \tau j_y \quad (6.14a)$$
$$j_y = \sigma_o \mathcal{E}_y + \omega_c \tau j_x \quad (6.14b)$$

These equations can be written in terms of the conductivity as follows,

$$\mathbf{J} = \sigma.\mathcal{E} = \frac{ne^2\tau/m}{1 + \omega_c^2\tau^2} \begin{pmatrix} 1 & -\omega_c\tau \\ \omega_c\tau & 1 \end{pmatrix} .\mathbf{E} \quad (6.15)$$

The derivation of the conductivity tensor has so far assumed that the conductivity arises from a set of electrons all with identical behaviour. In practice there is a velocity distribution of electrons due to various scattering processes which must be considered. The result would be a variation of the relaxation time with the velocity and energy of the charge carriers. Consequently the elements of the conductivity tensor must be replaced with their energy weighted averages over the density of states N(E) and zero electric field distribution function F(E) [164]. The conductivity tensor now becomes,

$$\sigma = \frac{ne^2}{m} \begin{pmatrix} \left\langle \frac{\tau}{1 + \omega_c^2\tau^2} \right\rangle & \left\langle \frac{-\omega_c\tau^2}{1 + \omega_c^2\tau^2} \right\rangle \\ \left\langle \frac{\omega_c\tau^2}{1 + \omega_c^2\tau^2} \right\rangle & \left\langle \frac{\tau}{1 + \omega_c^2\tau^2} \right\rangle \end{pmatrix} \quad (6.16)$$

where the angle brackets represents the weighted tensor components with the weighting function for a non-degenerate system being given as EN(E)F(E) [165].

6.3 The Hall Effect

Hall measurement represents the most widely used test for the electrical quality of a semiconductor. The results obtained from such a measurement can be used to determine the components of the conductivity tensor. In the Hall measurement technique a known current is constrained to flow along a

well-defined direction by the sample geometry and contacting. The application of a magnetic field perpendicular to the current direction will encourage an initial deflection of the charge carriers in the transverse direction, i.e. in a direction normal to the current and magnetic field. Because no current path exist in this direction, the charges will accumulate on the surfaces. This establishes a Hall electric field which opposes the charge motion and prevents further accumulation. In equilibrium the force produced by the Hall electric field will balance the Lorentz force exactly. If all the charge carriers have the same drift velocity, then in equilibrium all the carriers would move through the sample undeflected by the magnetic field. In this case the magnetoresistance will be zero, i.e. there will be no change in the sample resistance when a magnetic field is applied. Although the magnetoresistance in some metals can be very small, in most semiconductors quite large magnetoresistance can be measured, indicating that the Lorentz balance condition cannot be achieved for most of the carriers.

In Hall experiments the current density is established in the x-direction and the magnetic field is applied in the z-direction. No current is permitted to flow in the y-direction. Therefore from equation (6.15)

$$\begin{pmatrix} J_x \\ J_y \end{pmatrix} = \begin{pmatrix} \sigma_{xx} & -\sigma_{xy} \\ \sigma_{xy} & \sigma_{xx} \end{pmatrix} \begin{pmatrix} E_x \\ E_y \end{pmatrix} \tag{6.17}$$

where $\sigma_{xx} = \dfrac{ne^2\tau/m}{1 + \omega_c^2\tau^2}$

and $\sigma_{xy} = \dfrac{ne^2\tau/m}{1 + \omega_c^2\tau^2} \cdot \omega_c\tau$

Since $J_y = 0$ it follows that,

$$-\sigma_{xy}\mathcal{E}_x + \sigma_{xx}\mathcal{E}_y = 0 \tag{6.18}$$

Therefore $\mathcal{E}_y/\mathcal{E}_x = \sigma_{xy}/\sigma_{xx}$

$$= \omega_c\frac{\tau^2}{1 + \omega_c^2\tau^2} \Big/ \frac{\tau}{1 + \omega_c^2\tau^2} \tag{6.19}$$

$\mathcal{E}_y/\mathcal{E}_x$ is known as the Hall angle and if τ is constant then the Hall angle will be equal to $\omega_c\tau$.

The Hall coefficient R_H is given as

$$R_H = \mathcal{E}_y/J_xB \tag{6.20}$$

E_y and J_x can be determined directly and since B is a known quantity the Hall constant can be determined. From equations (6.17) and (6.18),

$$R_H = -\sigma_{xy}/\, B(\sigma_{xx}^{\ 2} + \sigma_{xy}^{\ 2}) \tag{6.21}$$

In the low magnetic field limit $\omega_c\tau \ll 1$ and

$$R_H = \frac{1}{ne}\frac{<\tau^2>}{<\tau>^2} = r_H/ne \tag{6.22}$$

where r_H is known as the Hall scattering factor which is dependent on the nature of the scattering mechanisms involved. In the high field limit $\omega_c\tau \gg 1$ and R_H = 1/ne exactly so that r_H can be determined by taking the ratio of R_H at low and high magnetic fields. The sign of R_H gives the type of the dominant charge carrier taking part in transport.

It follows therefore that measurement of the Hall constant is useful in determining the carrier concentration and their type. In addition equation (6.6) enables the mobility of the carriers to be calculated from the measured sample resistivity and Hall constant.

6.4 Magnetoresistance

The magnetoresistance of a semiconductor is usually defined as the fractional change in resistance produced by the application of a magnetic field. If the charge carriers in a semiconductor are all identical and described by a constant relaxation time, the Hall field will compensate fully the Lorentz force for all the carriers. In this case the magnetoresistance $\Delta\rho/\rho_o$ will be zero. On the other hand if there is more than one type of carrier with different effective masses or a single carrier with classical statistics and a relaxation time which is energy dependent, there will be some current flowing in the transverse direction to

the electric and magnetic fields. In this case $\Delta\rho/\rho_o \neq 0$. In addition sample configuration and contact size can also cause a complete or partial short circuit of the Hall field $\mathcal{E}_y$. If $\mathcal{E}_y = 0$ then for constant relaxation time equation (6.17) reduces to,

$$J_x = \sigma_o \frac{1}{1 + \omega_c^2\tau^2} \mathcal{E}_x \tag{6.23}$$

For $\omega_c\tau = \mu B \ll 1$,

$$\sigma(B) = \sigma_o(1 - \mu^2B^2)$$

or

$$\Delta\rho/\rho_o = \mu^2B^2 \tag{6.24}$$

The magnitude of the magnetoresistance may be varied for a partial short circuit of the Hall field, whether it is caused by sample geometry or a lack of uniformity which includes multilayer conduction.

6.5 Parallel Conduction

Parallel conduction in epitaxial materials makes Hall measurements difficult to interpret. Parallel conduction can involve (i) multiple carrier effects in which there are two or more distinct carrier species having different effective masses or (ii) multilayer system in which there are two or more layers taking part in conduction, each having different doping density. This is usually the case for InSb epilayer grown on an InSb substrate. Because of its narrow bandgap InSb has no semi-insulating form. As a result the substrate can contribute significantly to the measured Hall mobility.

Consider a system having two types of carriers (denoted by 1 and 2) in which N_1 and N_2 are the areal carrier concentrations and μ_1 and μ_2 are the mobilities. Using equation (6.14) then

for 1:

$$J_{x1} = \sigma_1\mathcal{E}_x + \mu_1 B J_{y1}$$
$$J_{y1} = \sigma_1\mathcal{E}_x + \mu_1 B J_{x1}$$

for 2:

$$J_{x2} = \sigma_2\mathcal{E}_x + \mu_2 B J_{y2}$$
$$J_{y2} = \sigma_2\mathcal{E}_x + \mu_2 B J_{x2}$$

Using $\sigma = Nq\mu$ the above equations can be rearranged to give the following;

$$J_{x1}(1 + \mu_1^2B^2) = q(N_1\mu_1\mathcal{E}_x + N_1\mu_1^2B\mathcal{E}_y)$$

$$J_{x2}(1 + \mu_2^2B^2) = q(N_2\mu_2\mathcal{E}_x + N_2\mu_2^2B\mathcal{E}_y) \tag{6.25}$$

$$J_{y1}+J_{y2} = 0 = q\mathcal{E}_y(N_1\mu_1+ N_2\mu_2) - q\mathcal{E}_xB(N_1\mu_1^2+ N_2\mu_2^2)$$

$$\Rightarrow \qquad \mathcal{E}_y = \frac{B(N_1\mu_1^2+N_2\mu_2^2)}{(N_1\mu_1 +N_2\mu_2)}\mathcal{E}_x \tag{6.26}$$

For low magnetic fields,

$$R_H = \frac{\mathcal{E}_y}{J_{x1}+J_{x2}} = \frac{N_1\mu_1^2+ N_2\mu_2^2}{q(N_1\mu_1+ N_2\mu_2)^2} \tag{6.27}$$

and for high fields ,

$$R_H= \frac{1}{q(N_1+ N_2)} \tag{6.28}$$

6.6 Scattering Mechanisms

It was shown in the previous sections that Hall measurements can be used to determine the type of charge carriers that are responsible for transport in a semiconductor. Their concentration and mobilities and even the scattering parameters can also be deduced from the results of Hall experiments. The mobility of a charge carrier can be expressed as

$$\mu =-e\tau/m^* \tag{6.29}$$

where m^* is now the effective mass of the carrier. If τ is a function of energy, then it can be expressed as an energy-averaged relaxation time, $\langle\tau\rangle$. The Hall coefficient of a material containing a single, non-degenerate and spherical conduction band is given as $R_H = r_H/ne$, where $r_H=\langle\tau^2\rangle/\langle\tau\rangle^2$ is a scattering or Hall factor and its value depends on the characteristics of the scattering process. The energy-averaged relaxation time also makes the Hall mobility different from the drift mobility, i.e $\mu_H= r_H\mu_d$.

Following is a brief discussion of some relevant scattering processes which

have been studied for semiconductors. The processes by which carriers can be scattered include:-

(i) acoustic phonon scattering
(ii) optical phonon scattering
(iii) ionised impurity scattering
(iv) dislocation scattering
(v) alloy scattering.

The above scattering processes can be combined by assuming that each process is independent of the others. In this case the total scattering rate ($1/\tau$) is simply given by the sum of the individual scattering rates for the various scattering processes, i.e.,

$$\frac{1}{\tau} = \sum_i \left(\frac{1}{\tau_i}\right) \tag{6.30}$$

This is known as Mathiesen's rule. Since the mobility is proportional to the relaxation time, it follows that the total mobility can be expressed as,

$$\mu = \left[\sum_i \frac{1}{\mu_i} \right]^{-1} \tag{6.31}$$

where μ_i is the mobility limited by the various scattering processes.

6.6.1 Acoustic Phonon Scattering

Carriers are scattered by collisions with disturbances in the periodic potential inside a semiconductor. These disturbances are due to thermal vibrations of the crystal lattice which are quantised as phonons. The local changes in the atomic spacing of the lattice caused by acoustic phonons introduces shifts in the energy band structure of the semiconductor which interact with the charge carriers. The resulting drift mobility limited by this type of scattering was derived by Shockley and Bardeen [166] as,

$$\mu_{AC} = \frac{(8\pi)^{1/2}\hbar^4}{3eE_{AC}m^{*5/2}} \rho u_l \frac{1}{(kT)^{3/2}} \tag{6.32}$$

where u_l is the average longitudinal sound velocity and E_{AC} is the acoustic deformation potential.

Another type of scattering which can occur with long wavelength acoustic phonons is piezoelectric scattering [167]. This type of scattering is more important at low temperatures (≤50K) but is usually insignificant except in very pure material.

6.6.2 Optical Phonon Scattering

Scattering by polar optical phonons is an inelastic process in which not only the momentum but also the energy of the electrons is changed. This is because the phonon energy is not always negligible compared with the energy of the electron. In such a case the solution of the Boltzmann's equation must be obtained numerically since the relaxation time approach cannot be applied. However for high temperatures, when $kT > \hbar\omega_{op} = k\theta$ where θ is the Debye temperature for the longitudinal optical phonon branch, the energy of most of the electrons is much higher than the phonon energy. Collisions can therefore be considered to be approximately elastic. The expression for the mobility limited by optical phonon scattering was determined by Ehrenreich [168] and given as,

$$\mu_{op} = \frac{16\hbar\varepsilon_o (2\pi k_B)^{1/2}}{3e\omega_{op}} G(z) \frac{[\exp(z)-1]}{1/\varepsilon(\infty)-1/\varepsilon(0)} T^{1/2} m^{*-3/2} \qquad (6.33)$$

where $z = \hbar\omega_{op}/k_B T$ and G(z) is a screening factor. G(z) is a slowly varying function of the order unity. ω_{op} is the angular frequency of the phonons.

6.6.3 Ionised Impurity Scattering

Ionised impurity scattering is important in relatively pure materials at low temperatures and at increasing higher temperatures as the materials become less pure. This mechanism is particularly important because the mobility and carrier concentration of a semiconductor at a known temperature can be used to deduce the concentration of ionised impurities and the compensation ratio. This is reflected in the work of Stillman and Wolfe [169] for GaAs and Walukiewicz and co-workers for GaAs [170,171] and InP [172] who produced empirical graphs and tables for the determination of the concentration of ionised impurities and the compensation ratio using the results of Hall measurements. This section will consider ionised impurity scattering for the cases when a semiconductor is (i) non-degenerate and (ii) degenerate.

Case 1: Non-degenerate

The initial formulation of ionised impurity scattering was given by Conwell and Weisskopf [173] in which the impurity potential was modelled by a Coloumb potential. Each ion was considered to scatter independently of all the others and the field produced by a single atom was terminated at half the mean distance between two impurity atoms. The mobility derived using these features is given as,

$$\mu_I = \frac{2^{7/2}(4\pi\varepsilon\varepsilon_o)^2(kT)^{3/2}}{\pi^{3/2}m^{*1/2}e^3N_I\ F} \tag{6.34}$$

where

$$F = \ln\{\ 1 + [3(4\pi\varepsilon\varepsilon_o)^2kT/e^2N_I^{1/3}]^2$$

N_I is the concentration of ionised impurities.

A quantum mechanical approach was later used to calculate the mobility, the treatment of which attempted to include screening by neighbouring impurities. This mobility as given by the theory of Brooks-Herring [174] is,

$$\mu_I = \frac{2^{7/2}(4\pi\varepsilon\varepsilon_o)^2(kT)^{3/2}}{\pi^{3/2}m^{*1/2}e^3N_I}\ \frac{1}{\ln(1+b)-b/(1+b)} \tag{6.35}$$

where

$$b = \frac{6}{\pi}\ \frac{(4\pi\varepsilon\varepsilon_o)m^*(kT)^2}{n\hbar^2e^2}$$

n is the free carrier concentration.

Case 2: Degenerate

The Brooks-Herring expression for the mobility due to ionised impurity scattering cannot be used for narrow bandgap semiconductors such as InSb. Their investigation of ionised impurity scattering was based on a spherical band structure and on semiconductors which were non-degenerate at low temperatures. InSb on the other hand has quite a complex band structure and is degenerate at 77K even for a carrier concentration as low as 10^{16} cm^{-3}.

Any interpretation of electron transport in InSb needs to take into account

the non-parabolicity of the conduction band and the small electron effective mass. Consequently even a relatively small number of electrons occupy quite high energies above the band edge and degenerate statistics apply even at relatively high temperatures (e.g. for $n \cong 10^{16}$ cm^{-3}, $E_f \cong 9meV \equiv 112^{o}C$). Following is an outline of a theory that has been developed by Zawadski and Szymanska [175,176] to calculate the mobility due to ionised impurity scattering in degenerate narrow bandgap semiconductors such as n-type InSb. This theory will be used in the next chapter to analyse the experimental data obtained from silicon doped InSb epilayers.

The relaxation time was obtained in the form of,

$$\tau(E) = \frac{1}{2\pi} \frac{(4\pi\varepsilon\varepsilon_o)^2\hbar}{e^4 N_i} \frac{1}{F} \frac{dE}{dk} k^2 \qquad (6.36)$$

where N_i is the concentration of scattering centres, E and k are the energy and wavevector of the scattered electron. F accounts for the screened Coloumb potential and to a good approximation is given as,

$$F = \ln (b+1) - \frac{b}{b+1} - a(4-a)[1- \frac{2}{b}\ln (b+1)]+\frac{3}{2} a^2(1-\frac{4}{b}) \qquad (6.37)$$

where $b = (2k\lambda)^2$ and $a = 2E/(E_g+2E)$.

λ = the screening length describing the screening of impurity ions by the free electrons. This is a function of the electron concentration and temperature.

E_g = the energy gap.

E = the electron energy in the conduction band taking the bottom of the conduction band to be E = 0.

Notice that for a parabolic band $E \ll E_g$ and F reduces to the expression given in the Brooks-Herring formulation of equation (6.35).

According to Zawadski [176] it is the momentum effective mass which must be used in any description of transport phenomenon in materials with non-parabolic conduction bands. The momentum effective mass is defined as,

$$\frac{1}{m^*} = \frac{1}{\hbar^2 k} \frac{dE}{dk} \qquad (6.38)$$

For InSb, Zawadski used a simplified version of Kane's band model in which

he assumed the energy of the spin orbit interaction to be much larger than the energy gap to derive the energy dependence of the wave vector in the conduction band,

$$\hbar^2 k^2/2m_c^* = E(1 + \frac{E}{E_g}) \tag{6.39}$$

where m_c is the effective mass at the bottom of the conduction band. From equations (6.38) and (6.39),

$$m^* = m_c\,(1 + 2E/E_g) \tag{6.40}$$

For conditions of high degeneracy it can be assumed that only electrons at the Fermi surface are involved in transport. It was shown [175] that, for a non-parabolic band, the expression for the Fermi energy can be written as,

$$E_f = \frac{1}{2}\,E_g(\sqrt{\delta} - 1) \tag{6.41}$$

where

$$\delta = 1 + 2\pi^2\left(\frac{3}{\pi}\right)^{2/3}\left(\frac{\hbar^2}{m_c^* E_g}\right) n^{2/3}$$

Hence the effective mass of the electrons at the Fermi surface will be given by,

$$m^*(E_f) = m_c^*\sqrt{\delta} \tag{6.42}$$

But at the Fermi surface $\frac{dE}{dk} = \frac{\hbar^2 k_f}{m^*}$ and $k_f = (3\pi^2 n)^{1/3}$.Therefore the mobility due to ionized impurity scattering in a degenerate semiconductor having a non-parabolic conduction band can be written as,

$$\mu_i = \frac{3\pi}{2}(4\pi\varepsilon\varepsilon_o)^2 \frac{\hbar^3}{e^3} \frac{n}{N_i} \frac{1}{m^{*2}\,F} \tag{6.43}$$

In the parameters a and b necessary to calculate F we need to put $E = E_f$. Therefore,

$$a = 1 - \frac{m_o^*}{m^*(E_f)} \tag{6.44}$$

The parameter b has been calculated by Kolodziejczak [177] and is given by,

$$b = \pi^2(3/\pi)^{1/3}(4\pi\varepsilon\varepsilon_o)\hbar^2/(e^2m^*)n^{1/3} \tag{6.45}$$

6.6.4 Dislocation Scattering

Dislocation scattering was first treated by Dexter and Seitz [178] who considered the scattering of electrons or holes by the dilation of the lattice around rigid, randomly arranged edge type dislocations. In their calculations the mobility due to dislocation scattering was found to be proportional to the temperature and inversely proportional to the density of dislocation lines. Another mechanism whereby dislocations can cause scattering was suggested by Read [179,180] who treated dislocations as a line of accepter centres creating a space-charge cylinder. Electrons can then make elastic collisions with these rigid cylinders. The scattering by such cylinders is highly anisotropic, being a maximum when the electrons move perpendicular to the cylinders and zero for motion parallel to the cylinders. It was shown that the scattering by dislocations can be described by a relaxation time given by,

$$\tau_d = \frac{3}{8} RNv \tag{6.46}$$

where v is the velocity of the electrons; N is the number of dislocations per unit area and R is the radius of the space-charge cylinder which is related to the spacing between acceptors on dislocations, the spacing between acceptor impurities and the free carrier concentration by the condition of electrical neutrality.

At room temperature dislocation scattering becomes dominant only if the number of dislocations is of the order $10^9 cm^{-2}$. However, at low temperatures dislocation scattering can become significant.

6.6.5 Alloy Scattering

Alloy scattering in a ternary semiconductor is caused by randomness in the distribution of the alloying constituents. An expression for the mobility due to alloying scattering was developed by Brooks [181] as,

$$\mu_A = \frac{\sqrt{2}\pi}{3} \frac{q\hbar^4 N_{al}}{(kT)^{1/2} m^{*5/2} x(1-x)(\Delta E)^2} \tag{6.47}$$

where x and (1-x) are the mole fractions of the binary end compounds, N_{al} is the density of alloying sites and ΔE is assumed to be the bandgap difference between the end compounds.

6.7 Effect of Magnetic Field on Electrons in a Semiconductor

When the applied magnetic field is large such that $h\omega_c > kT$ the classical treatment of electron motion breaks down. At the onset of the quantum limit a number of new phenomena become apparent in the electrical resistance of a semiconductor. The effect of applying a magnetic field to a semiconductor manifests itself in the conversion of the energy bands into a series of energy levels known as Landau levels in which the electron orbits are quantised. This section introduces the concept of magnetic quantisation in both a three-dimensional and a two-dimensional system.

Consider an electron in a semiconductor which has an isotropic and constant effective mass, m^*. In the presence of a magnetic field the Hamiltonian becomes,

$$\hat{\mathcal{H}} = (\hat{p} - eA)^2/2m^* \tag{6.48}$$

where A is the magnetic vector potential given in the Landau gauge by A=(0,Bx,0) representing a magnetic field strength B in the z-direction. The Hamiltonian can then be written as,

$$\begin{aligned} \hat{\mathcal{H}} &= [\hat{p}_x^2 + (\hat{p}_y - eBx)^2 + \hat{p}_z^2)]/2m^* \\ &= \hat{\mathcal{H}}_1 + \hat{\mathcal{H}}_2 \end{aligned} \tag{6.49}$$

with

$$\hat{\mathcal{H}}_1 = [\hat{p}_x^2 + (\hat{p}_y - eBx)^2]/2m^*$$

and

$$\hat{\mathcal{H}}_2 = \hat{p}_z^2/2m^*$$

The Hamiltonian $\hat{\mathcal{H}}_2$ represents the motion of the electron in the z-direction and the solution is exactly the same as for a free electron in this

direction, i.e.

$$E_z = \hbar^2 k_z^{\,2}/2m^* \tag{6.50}$$

Hence with a magnetic field along the z-direction the energy of the electron along this direction remains unchanged.

The Hamiltonian $\hat{\mathcal{H}}_1$ represents the electron motion in the x-y plane. By putting $x = x' - \hbar k_y/eB$, $\mathcal{H}_1$ can be rewritten as,

$$\hat{\mathcal{H}}_1 = (\hat{p}_x^{\,2} + e^2B^2x'^2)/2m^* \tag{6.51}$$

which is no more than the Hamiltonian for a simple harmonic oscillator centred at $x' = \hbar k_y/eB$. Hence the energy of the complete system can be expressed as,

$$E = (n + \tfrac{1}{2})\hbar\omega_c + \hbar^2 k_z^{\,2}/2m^* \tag{6.52}$$

where $\omega_c = eB/m^*$ known as the cyclotron frequency. The energy of the electron states therefore, can be considered to be the sum of a translational energy along the magnetic field together with the quantised energy, into levels known as the Landau levels, of the cyclotron motion in the plane normal to the field. Figure 6.1a shows the Landau levels associated with the presence of the magnetic field. These Landau levels will change the density of states available for the electron.

Suppose the crystal has sides L_x, L_y, L_z then the centre of the harmonic oscillator of equation (6.52) must lie in the crystal, and so

$$0 < \hbar k_y/eB < L_x$$

Therefore

$$0 < k_y < eBL_x/\hbar$$

But, due to the periodicity of the Bloch functions the allowed values of k_y is given by $k_y = 2\pi N/L_y$, where N is an integer. Hence the maximum number of allowed values of k_y is given by,

$$N_{max} = L_y/2\pi \,.eBL_x/\hbar = eB/h \text{ per unit area} \tag{6.53}$$

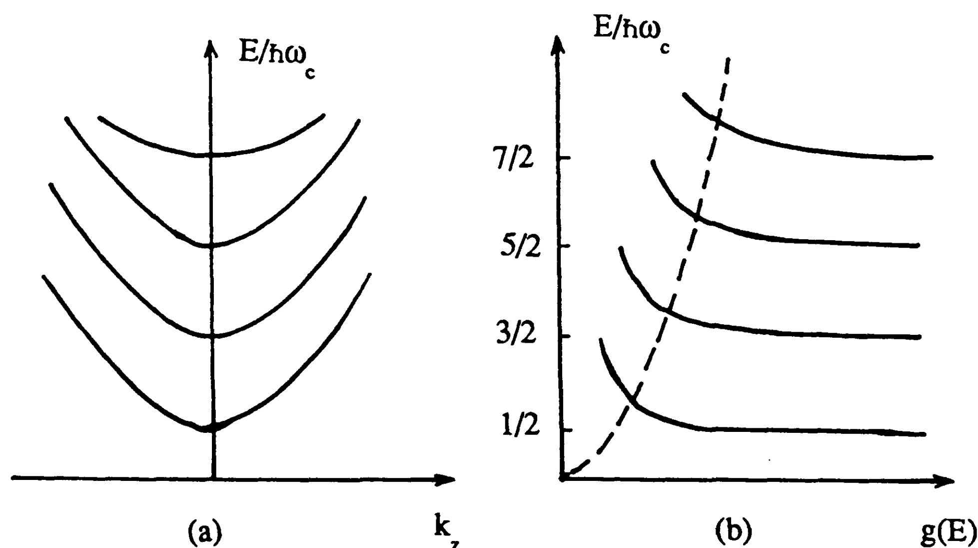

Figure 6.1 Landau levels and the modification of the density of states associated with the presence of a magnetic field in a 3D system.

Therefore the density of states per unit area is given by

$$g(E) = 2eB/h \; D(E) \tag{6.54}$$

where D(E) is the one dimensional density of states due to motion in the z-direction. The factor of 2 is included to take account of spin degeneracy. The density of states in one dimension is inversely proportional to the square root of the energy. Therefore, for a 3-dimensional system in which the magnetic field is along the z-direction, the density of states will be as shown in figure 6.1b.

In a two-dimensional system the electron motion is restricted to two dimensions by a confining potential as in a quantum well or an accumulation layer. The eigenstates for electron motion perpendicular to the well consist of a set of discrete levels known as electric subbands, but the motion in the plane of the well remains unaffected. The Hamiltonian for such 2-D system will therefore include an additional term due to the confining

potential V(z) in equation (6.49), that is

$$\hat{\mathcal{H}} = [\hat{p}_x^{\,2} + (\hat{p}_y\text{-}eBx)^2 + \hat{p}_z^{\,2}]/2m^* + V(z) \tag{6.55}$$

For the potential well,

$$\hat{\mathcal{H}}_{well} = \frac{\hat{p}_z^{\,2}}{2m^*} + V(z) \tag{6.56}$$

The solution of the Schrodinger equation for the well will give a set of discrete eigenstates with energies E_i, i= 0,1,....etc. The motion in the x-y plane will be quantised into Landau levels as before. The total eigenenergies of the 2-dimensional system can therefore be written as,

$$E = (n + \tfrac{1}{2})\hbar\omega_c + E_i \tag{6.57}$$

For a free electron in 2-dimensions, the density of states can be expressed as,

$$g(E)\, dE = (m^*/\pi\hbar^2)\, dE \tag{6.58}$$

However the presence of the magnetic field introduces an infinite set of Landau levels which are associated with each electronic subband, characterised by E_i. In the presence of a magnetic field therefore, the density of states of a 2D system will ideally consist of a series of Dirac delta functions at energies given by $E - E_i = (n + \frac{1}{2})\hbar\omega_c$. In the presence of scattering the Landau levels will be broadened as shown in figure 6.2.

6.8 The Shubnikov-de Haas Effect

We have seen in the previous section that the presence of a magnetic field has changed the quantisation scheme for free electrons. These electrons are now quantised into cyclotron orbits in a plane perpendicular to the magnetic field and the electron energies are quantised into Landau levels.

If the magnetic field is now varied, the Landau levels will pass through the Fermi level, which is high in the conduction band for degenerate semiconductor and is almost independent of field. Since only electrons near the Fermi level contribute to the conductivity, there will be a sudden change in the density of states for scattering involving elastic processes

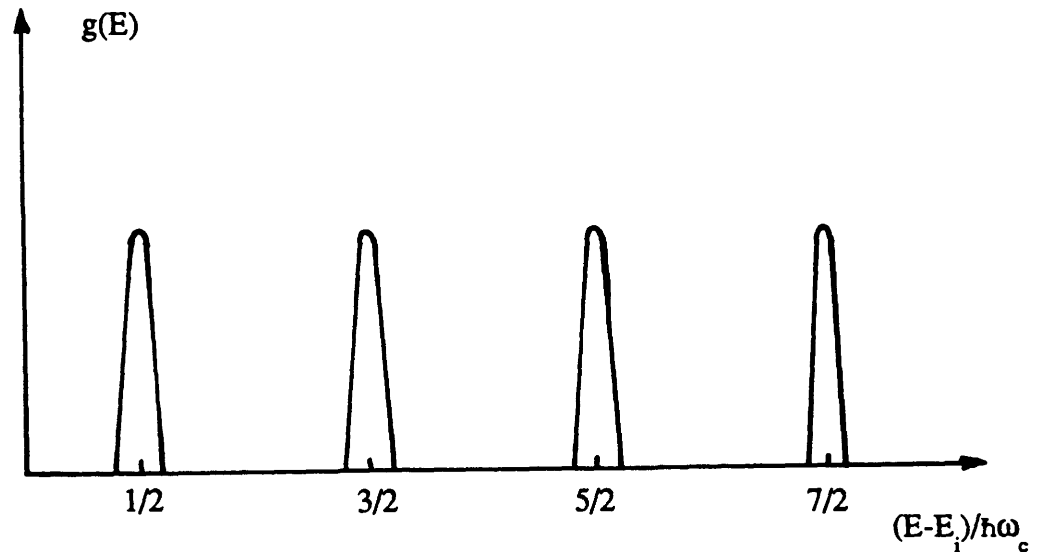

Figure 6.2 Density of states of a 2D system in the presence of a magnetic field.

as the bottom of a Landau level coincides with the Fermi level. As a result there will an oscillatory behaviour in the magnetoresistance as the magnetic field is varied. The period of these Shubnikov-de Haas oscillations can be used to calculate the free carrier concentration.

For Shubnikov-de Haas oscillations to be observed μB (in SI units) should be greater than unity and the temperature of the sample should be low, i.e. $kT \ll \hbar\omega_c$. The requirement that $\mu B = \omega_c \tau \gg 1$ arises from the fact that the lifetime, τ is limited by the scattering of the carriers. The observation of Landau quantisation of the energy states is possible only if the carrier moves through a significant part of its magnetic orbit before it is scattered into another state. Low temperature is necessary to reduce the deviation of the carriers from the Fermi surface. This would ensure that the separation, $\hbar\omega_c$ between Landau levels is greater than the energy spread associated with the Fermi surface.

The oscillations occur when the Landau subbands coincide with the Fermi Level, i.e.

$$E_f = (n + \tfrac{1}{2})\hbar\omega_c = (n + \tfrac{1}{2})\hbar eB/m^* \qquad (6.59)$$

If B_1 and B_2 ($B_1 > B_2$) are the magnetic fields corresponding to two successive peaks then,

$$1/B_1 = (n + \tfrac{1}{2})\hbar e/m^*.1/E_f$$

$$1/B_2 = (n - \tfrac{1}{2})\hbar e/m^*.1/E_f$$

Therefore,

$$1/B_2 - 1/B_1 = \Delta(1/B) = \hbar e/m^*.1/E_f \qquad (6.60)$$

Equation 6.48 indicates that the oscillations are periodic in reciprocal magnetic field with a characteristic period of $\Delta(1/B)$.

For heavily doped semiconductors in 3-dimensions and in the absence of a magnetic field, the number of available electronic states below the Fermi level is given by,

$$n_o = \int g(E)\, dE$$

where g(E) is the 3-dimensional density of states.

$$n_o = \int_o^{E_f} \frac{1}{2\pi^2} \left(\frac{2m^*}{\hbar^2}\right)^{3/2} E^{1/2}\, dE \qquad (6.61)$$

or

$$E_f = (3\pi^2 n_o)^{2/3}\, \hbar^2/2m^* \qquad (6.62)$$

which is the familiar result for the free electron model of a metal. Using equations (6.60) and (6.62) the carrier concentration can be calculated from,

$$n_o = 1/3\pi^2\, [\hbar/2e\ .\ \Delta(1/B)]^{-3/2} \qquad (6.63)$$

The above relation assumes that spin splitting is not resolved in the Shubnikov-de Haas oscillations. It should also be noted that the period $\Delta(1/B)$ is independent of the effective mass. In the case of a 2-dimensional system in which more than one electronic subbands are occupied, each subband

will contribute to a well-defined series of oscillations periodic in 1/B. For each subband , i, provided spin splitting is unresolved the period of the oscillations is given by,

$$\Delta(1/B)_i = e/(n_i \pi \hbar) \tag{6.64}$$

where n_i is the carrier concentration for the ith subband.

6.9 Experimental

Hall measurements at 300K and 77K were performed using a magnetic field strength of ~0.05 Tesla obtained from an electromagnet. In addition continuous temperature measurements in the range 77K to 300K were obtained using an automated pulsed field Hall system developed by the Solid State group at Imperial College. Shubnikov-de Haas experiments were performed using either a 8T or a 14T superconducting magnet.

Figure 6.3a shows a van der Pauw [182] clover-leaf pattern, eroded by sand blasting on the semiconductor samples for the purpose of performing Hall measurements. The use of a clover-leaf shaped specimen eliminates any errors which may be due to the position and size of the contacts [183]. The contacts comprise of In dots annealed in an atmosphere of hydrogen and nitrogen.

Resistivity is measured by passing a known current (I) through two adjacent contacts and measuring the voltage (V) developed across the remaining two contacts. The current is then reversed to eliminate any errors introduced by electrothermal or thermoelectric effects. The combination of the contacts is changed and the measured voltages are averaged and used to calculate the resistivity. The resistivity for a sample of thickness, d is determined using the following expression,

$$\rho = \frac{\pi d}{\ln 2} \left(\frac{V}{I} \right) \tag{6.65}$$

The Hall coefficient is determined by passing the current through a pair of opposite contacts and measuring the Hall voltage between the remaining contacts when the magnetic field is applied perpendicular to the sample plane. Normally the magnetic field is rotated through 180° and the average of the measured values is taken to be the Hall voltage. This technique

eliminates any residual Hall voltage which may be due to mixing of R_{xx} and R_{xy}. In addition the polarity of the current is also reversed. The Hall coefficient is then calculated using the relationship,

$$R_H = d\ \Delta V_H/(IB) \tag{6.66}$$

where ΔV_H is the Hall voltage and B the magnetic field strength. From the Hall coefficient and resistivity measurements the Hall mobility can be deduced from the relationship that $\mu_H = R_H/\rho$.

Shubnikov-de Haas experiments were performed using a Hall bar sample configuration as shown in figure 6.3b. The current is passed through the end contacts and ρ_{xx} measurements are recorded using the contacts from two adjacent arms. ρ_{xy} on the other hand utilises two opposite arms. The data are collected by a computer which is also used to perform electronic differentiation and Fourier transform to determine the period of oscillations, and hence the free carrier concentration of the samples.

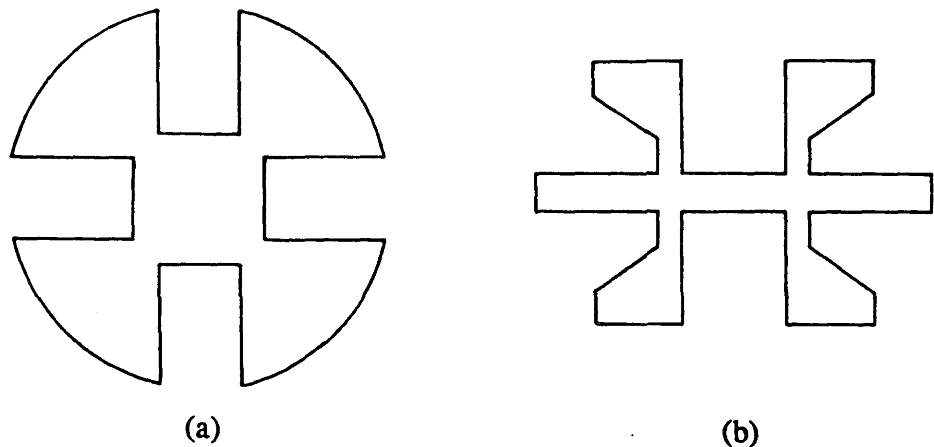

Figure 6.3 (a) Clover leaf and (b) Hall bar configurations etched onto the semiconductor samples for Hall and Shubnikov-de Haas experiments.

CHAPTER 7 RESULTS AND DISCUSSION

This chapter presents the results of the electrical characterisation of InSb, InAs and InAsSb.

7.1 Undoped InSb

Because of its narrow bandgap InSb has no semi-insulating form. As a result homoepitaxial films of InSb are difficult to characterise, even at low temperatures, because the shorting effects of the conducting substrates complicate the results of electrical measurements. In this study, Hall measurements carried out on undoped films grown on p-type substrates indicate n-type conductivity at 77K, with room temperature mobilities very close to the phonon limited value of 70,000 $cm^2V^{-1}s^{-1}$ and a free carrier concentration of the order $\sim 10^{16}cm^{-3}$. Figure 7.1 shows the temperature variation of the mobility and carrier concentration for a 5μm undoped InSb epilayer on a p-type substrate. The apparent 77K mobility and electron concentration are ~5,000 $cm^2V^{-1}s^{-1}$ and $\sim 3x10^{14}cm^{-3}$ respectively. These values represent the combined mobilities and carrier concentrations of both the conducting p-type substrate, the epilayer and any effects due to the interface and surface regions. An I-V measurement, figure 7.2, between contacts on the epilayer and the substrate reveals the existence of a p-n junction at the interface which would reduce, to some extent, the effect of the conducting substrate.

Accurate electrical data on homoepitaxial InSb epilayers requires the removal of the conducting substrates. Noreika and co-workers [53] removed the substrates from homoepitaxial InSb by chemical polishing and demonstrated that films having Hall mobilities and free carrier concentration approaching bulk values can be achieved. Dr. T. Ashley from RSRE carried out Hall measurement on sample IC101 with the substrate removed. The sample was glued onto a sapphire disc and the substrate removed by polishing. He found p-type conduction with hole concentration $\sim 3x10^{14}cm^{-3}$ and 77K mobility of around 10,000 $cm^2V^{-1}s^{-1}$ [184]. These results therefore suggest an n-type region at the interface between the p-type substrate and the epilayer. The substrate cleaning procedure at the time of the growth of the undoped InSb/InSb samples involved argon ion bombardment with an energy of 500eV followed by thermal annealing at 200°C. Subsequent 4K measurements showed strong Shubnikov-de Haas oscillations, figure 7.3, involving a two

dimensional electron gas with a carrier density of $1\times10^{12}cm^{-2}$ arising from the damaged interface. Recently Yuen *et al* [185], during the growth of α-Sn on InSb developed a gentler cleaning procedure involving different etches, lower energy ions (350eV) and shorter annealing periods. Substrates prepared in this way did not show a 2DEG. The Hall data shown in figure 7.1 therefore resulted from the combined effects of the epilayer, the n-type interfacial 2DEG and the p-type substrate.

Heteroepitaxial films of InSb grown on GaAs offer the opportunity to perform electrical characterisation without the need for substrate removal but with the disadvantage of a 14% lattice mismatch between the substrate and epilayer. All undoped InSb epilayers grown on GaAs exhibit n-type behaviour. Table 7.1 lists the electrical properties, obtained from Hall measurements of the undoped layers grown in this study. Figure 7.4 shows a typical temperature variation of the Hall mobility and carrier concentration on a 1.6μm thick InSb film on GaAs. These heteroepitaxial films are intrinsic at room temperature with mobilities of ~45,000 $cm^2V^{-1}s^{-1}$. The apparent mobility falls rapidly as the temperature is reduced from 300K to a value of ~10,000 $cm^2V^{-1}s^{-1}$ at 77K with an electron concentration of around $7\times10^{15}cm^{-3}$ at 77K.

Earlier studies of InSb films grown on GaAs substrates attributed the decrease in mobility with temperature to dislocation scattering at the interface. The heterointerfaces of these structures are known to have

Sample	Thickness (μm)	Growth Temp. (°C)	n_{hall} 300K (cm^{-3})	n_{hall} 77K (cm^{-3})	μ_{hall} 300K (m^2/Vs)	μ_{hall} 77K (m^2/Vs)
86 InSb/InSb	5.0	T_T-30	1×10^{16}	3×10^{14}	7.0	0.5
101 InSb/InSb	5.0	T_T-30	1×10^{16}	5×10^{14}	7.5	0.5
53 InSb/GaAs	1.0	T_T+50	3.7×10^{16}	1.2×10^{16}	4.3	0.9
59 InSb/GaAs	1.6	T_T+50	2.2×10^{16}	7.5×10^{15}	4.5	1.7

Table 7.1 Electrical properties of undoped InSb epilayers.

dislocation densities greater than $10^{11}cm^{-2}$ falling to the order of $10^{7}cm^{-2}$ at a distance of 5μm from the interface [154,186]. Yano *et al* [49] used an "etch-measure" technique to demonstrate that the electrical properties of the InSb films were not homogeneous throughout the layer. The Hall mobility decreases and the carrier concentration increases towards the interface. This was explained by assuming that the high density of dislocations in the vicinity of the interface would lead to a sheet of acceptor-like defects. Noreika and co-workers [53,54] also reported a thickness dependence in the Hall mobility obtained from InSb epilayers grown on GaAs. Their undoped layers were also n-type but the 77K mobility showed a sharp drop from bulk values for layers less than 20μm in thickness. From the mobility-temperature data mixed conductivity (i.e. contributions from both electrons and holes) similar to melt-grown InSb [187] was detected in these layers (i.e. ≤20μm).

These results of Noreika *et al* suggested a p-type interface between the substrate and the epilayer which would lead to parallel conduction causing a reduction in the apparent mobility without dislocation scattering being significant. The rather low mobilities of the undoped heteroepitaxial layers shown in table 7.1 could in part arise from the parallel conduction by this p-type region close to the interface. This p-type region could also be due to a layer of undoped GaSb at the interface as a consequence of the growth procedure. The possibility that some kind of surface exchange mechanism between arsenic and antimony to form GaSb during the initial stages of InSb growth on GaAs cannot be discounted. However, Hall measurements on thin InSb layers on GaAs (≤1μm) indicated n-type conductivity even for thickness down to 1000Å [188], with the Hall mobility decreasing and the apparent carrier concentration increasing as the distance from the interface is reduced. These results therefore suggest that dislocation scattering may be the dominant mechanism limiting the low temperature mobility of the undoped InSb layers on GaAs. However, as will be shown in section 7.2.2 the mobility of a sample with a doping slab 1000Å thick at the interface is only a factor of 2 lower compared with the normal ionised impurity scattering limited mobility for bulk samples at the doping concentration concerned. This is inconsistent with dislocation scattering limiting the low temperature mobility but suggests parallel conduction from a p-type region at the interface. It may be that there are a combination of mechanisms involving both dislocation scattering and parallel conduction which are limiting the low temperature Hall mobility for the undoped InSb/GaAs samples.

7.2 Investigation of Silicon as an n-type Dopant in InSb

This section presents the results on a study of the incorporation of silicon in InSb as a possible n-type dopant which is necessary for the fabrication of device structures. Silicon was chosen as a potentially useful donor impurity because it is known to work well for GaAs and does not have the high vapour pressures of the alternative group VI elements such as tellurium and selenium. During this study semi-insulating GaAs substrates were used since they allow Hall and resistivity measurements to be carried out without the need for substrate removal. As previously mentioned, the large lattice mismatch introduces a high density of dislocations at the InSb-GaAs interface. This was confirmed by cross-sectional TEM studies [53,154,186]. The work reported in this section also addresses the effect of the interface on the electrical properties of the epilayers.

The approach adopted involves the growth of InSb films which are slab-doped, i.e. only a small fraction (1/12th) of the total thickness (~1.5μm) of each epilayer is intentionally doped. In each case the dopant concentration is chosen so that the slab-doped region dominates the electrical properties of the entire epilayer at 77K. In addition, by growing layers in which the doping slabs are positioned at a range of distances (d) from the interface ($0 < d < 1.5\mu m$), it is possible to identify the range of values of d for which the electrical properties are degraded. Table 7.2 summarises the electrical properties of the Si doped samples grown for this study.

7.2.1 Hall Results for samples Grown at Low temperature

With the doping slab thickness chosen to be in the range of 900Å and 1500Å a good compromise is achieved between the need to have a distinct range of slab positions while allowing the electron gas to remain approximately three dimensional. This thickness also ensures that the slab conductance is considerably greater than the undoped regions of the epilayer at the silicon doping levels studied ($n > 10^{17}cm^{-3}$). At lower concentrations, corrections to the measured electrical parameters are required because of parallel conduction from the surrounding undoped regions.

Figure 7.5 shows the temperature dependence of the apparent mobility and carrier concentration for a slab-doped sample (IC69) grown at low temperature. In deriving the carrier concentration shown it is assumed that

Sample Number	Epilayer Thickness (μm)	Slab Thickness (μm)	Slab Position (%)	Growth Temperature (°C)	Silicon Concentration ($/10^{17}cm^{-3}$)	Measured Concentration ($/10^{17}cm^{-3}$)	Mobility 77K (m^2/Vs)	Mobility 300K (m^2/Vs)
43	3.6 Si doped InSb/InSb			T_T+50	1.4	0.81*	-	-
60	1.50 Si doped InSb/GaAs			T_T+50	2.4	0.82	2.8	3.0
55	1.78	0.150	100	T_T+50	2.0	1.3	2.0	3.0
56	1.69	0.140	75	T_T+50	2.1	0.96	1.2	4.2
57	1.60	0.140	25	T_T+50	2.3	1.9	2.7	3.7
58	1.69	0.140	0	T_T+50	2.1	1.8	1.5	4.7
61	1.58	0.130	50	T_T+50	2.3	1.7	3.1	4.4
62	1.55	0.130	50	T_T+10	2.3	2.2	3.4	4.0
64	1.44	0.120	50	T_T-30	2.5	2.7	4.0	3.8
66	1.50	0.130	100	T_T+50	2.4	0.82	1.2	5.0
67	1.12	0.095	25	T_T+50	3.2	1.2	1.3	5.1
69	1.72	0.150	50	T_T-30	1.0	1.3	4.7	5.0
71	1.11	0.094	50	T_T-30	33.0	20.0	2.2	1.4
97	0.87	0.074	50	T_T-30	65.0	52.0	0.87	1.08
98	0.87	0.074	50	T_T-30	130.0	75.0	0.66	0.87
92	Si doped InSb/InSb			T_T+50	20.0	0.8	0.7	7.0
93	Si doped InSb/InSb			T_T-30	20.0	20.0	1.5	4.5

*as deduced from Shubnikov-de Haas

Table 7.2 Growth parameters and electrical properties of slab-doped InSb epilayers.

all the conductivity is arising from the doped slab. This approximation is not true at room temperature since the undoped region will also be intrinsic.

Although Shubnikov-de Haas measurements, discussed in section 7.2.4 show some two dimensional effects, a large number of subbands are occupied for slab thickness of the order of 1000Å. As a result, the mobilities measured for the slabs should to first order be unaffected by two dimensional confinement effects. In delta doped GaAs where confinement effects are large and the electrons occupy only a few subbands the measured mobilities show little change from the mobilities found with the equilavent three dimensional concentrations, e.g. $1\times10^{12}cm^{-2}$ and $1\times10^{18}cm^{-3}$ bulk doped samples both have the mobilities in the 2,500 to 3,000 $cm^2\ V^{-1}s^{-1}$ range [189]. With the slab-doped samples high field Shubnikov-de Haas measurements give the same carrier concentration as the low field Hall measurements to within experimental error. Table 7.3 compares the carrier concentrations deduced from the two methods. The Shubnikov-de Haas oscillations started from low magnetic fields substantiating the measurement of high mobilities in the slab-doped material. The mobilities obtained with the samples grown at low temperatures and having the doping in the centre of the epilayer were virtually identical with bulk values over a range of doping levels from

Sample	$n_{S\text{-}de\,H}$ (cm^{-3})	n_{Hall} (cm^{-3})
60	8.5×10^{16}	8.2×10^{16}
62	1.8×10^{17}	2.2×10^{17}
64	2.34×10^{17}	2.7×10^{17}
69	1.56×10^{17}	1.3×10^{17}
71	2.48×10^{18}	2.0×10^{18}

Table 7.3 Comparison between free carrier concentration obtained from Shubnikov-de Haas measurements and low field Hall measurements.

$1x10^{17}$ to $3x10^{18}cm^{-3}$. The experimental data for the 77K mobilities from both bulk grown and MBE grown InSb samples are compared in figure 7.6 with the theoretical ionised impurity limited mobilities. The solid curve is generated from equation (6.43) by asumming no compensation, an InSb bandgap of 0.23eV, ε = 16.8 and an effective mass at the bottom of the conduction band of $0.0145m_o$. Since the electron concentrations are above the metal-insulator transition then all the impurities will be fully ionised and $N_i = n$. From figure 7.6 the mobilities achieved with the MBE materials grown at nominal temperatures in the range of T_T-20^oC to T_T-40^oC compare favourably with those from bulk grown samples. T_T represents the transition temperature at which the surface reconstruction changes from a c(4x4) to the "(1x3)" during layer growth. All experimental points fall below the theoretical limit predicted by equation (6.43). This however, is not evidence for compensation as no account has been made of other scattering mechanisms. In a detailed analysis, Zawadski and Szymanska [175] took into account other scattering mechanisms as well non-parabolicity to fit accurately experimental data at 300K assuming no compensation. Unfortunately, accurate values for the contributions to the mobility from other scattering mechanisms are not available for 77K. These contributions at 77K are therefore estimated by scaling the 300K values by assuming the appropriate temperature dependences. The results are shown as the dotted curve in figure 7.6. Although the agreement is somewhat better, the experimental points for both the epitaxial and bulk grown samples are still lower than the predicted values. For $n < 10^{17}cm^{-3}$ the MBE slab doped samples will be affected by parallel conduction from the undoped regions. For $n > 10^{17}cm^{-3}$ calculations using equations (6.27) for parallel conduction indicate that the electrical properties of the slab are unaffected by parallel conduction. It should also be noted that the Fermi energy is assumed to be much greater than kT and therefore, the measured Hall mobility is equal to the drift mobility. Nevertheless, the agreement between the experimental results and the theoretical predictions is reasonable and can be used to determine the electrical quality of InSb epilayers.

At doping levels above $3x10^{18}cm^{-3}$ the carrier concentration achieved is below that expected from the incident silicon flux, shown in figure 7.7, and the mobilities are also decreased markedly. This suggest a 3-dimensional solubility limit of $\cong 3x10^{18}cm^{-3}$ for silicon in MBE grown InSb or that silicon is starting to act amphoterically, even at the lower growth temperatures, at these high carrier concentrations.

7.2.2 Hall Results for Samples Grown over a Range of Temperatures

Figure 7.8 shows the results for samples grown at different nominal growth temperatures and with varying doping-slab positions. In all these samples the silicon flux and the growth rate were kept approximately constant and for the magnitude of the silicon flux used each slab is expected to have a silicon atom concentration of around $2.5\times10^{17}cm^{-3}$. The growth rate variation was estimated to be around 5% from sample to sample as a result of the daily fluctuation of the indium flux as monitored by the beam equivalent pressure. During the growth of these samples, epilayer thickness was calibrated *ex-situ* as RHEED oscillations had not as yet been observed for InSb. Consequently the thicknesses for the different samples are spread between values of about 1 and 1.5 µm. In comparison with figure 7.6 a qualitative difference immediately apparent is the decrease in mobility with decreasing carrier concentration. To investigate the effects of growth temperature, for samples IC61, IC62 and IC64, the position of the slab was fixed half way through the epilayer and the growth temperature was decreased in steps of $40^{o}C$ from $T_T+50^{o}C$ for sample IC61 to $T_T-30^{o}C$ for sample IC64. The samples grown at the higher temperatures all have significantly lower carrier concentrations than those grown at the lowest temperatures. However, for reasons explained in the previous chapters it is extremely difficult to accurately measure the substrate temperature especially for these nominal changes. This is thought to explain why some samples grown under apparently identical conditions and with the conducting slab in the same positions have carrier concentrations and mobilities which are different, as is the case for samples IC57 and IC67. Nevertheless, as shown in figure 7.6 samples grown at low temperatures, in the range $T_T-30^{o}C$ to $T_T-40^{o}C$ all show the expected carrier concentrations and corresponding bulk mobilities. In figure 7.8 several samples (IC56, IC66, IC67) grown at higher temperatures of $T_T+50^{o}C$ show a factor of three drop in both mobility and carrier concentration as compared to the values achieved for low temperature growth. Based on the assumption that the carrier concentration achieved is a reliable measure of the growth temperature, a clear dependence of mobility on the carrier concentration emerges. This dependence also enables the effect of the slab position, within the epilayer, on the electrical properties to be determined. Hence the plot of mobility against carrier concentration in figure 7.8 which clearly shows the interdependence.

Since the silicon flux was kept constant during growth, the total concentration of ionised impurities can be considered to be constant irrespective of the growth temperature if silicon is acting amphoterically, provided that the concentration of the residual impurities is negligible and there is no diffusion away from the doping slabs. The solid line in figure 7.8 represents a plot of the theoretical mobility for a constant value of total ionised impurities, $N_i = 3.5 \times 10^{17} cm^{-3}$, using the expression for the mobility due to ionised impurities for InSb given in the previous chapter. The link between mobility and carrier concentration demonstrated by the theoretical curve agrees well with the large changes found experimentally and represents strong evidence that silicon is behaving amphoterically at high growth temperatures. The observations that bulk mobilities are achieved suggest that silicon is acting only as a donor at low growth temperatures and for the carrier concentrations involved, no significant scattering from dislocations occurs at distances beyond ~0.5 μm from the interface.

Figure 7.8 also shows the effect of varying the position of the doping slab on the mobility for the samples grown at $T_T+50^{\circ}C$. For the same carrier concentration the mobility of the samples, with doping slabs in the centre of the layer, is higher than the other samples. In the samples where the slabs are inserted at the InSb-GaAs interface the mobility falls by more than a factor of 2 as compared with the mobility when the slab is at the centre of the epilayer. The reduction in the mobility of the sample with the doping slab at the interface probably arises from scattering from or precipitation at the high density of misfit dislocations. It should be noted that at these high doping density the Fermi velocity is extremely large ($\sim 10^{6} ms^{-1}$). As a result dislocations would not affect the mobility of the conduction electrons as much as in a non-degenerate system. With a carrier distribution of the order $10^{17} cm^{-3}$ classically distributed the corresponding drop in the mobility will be a factor of 5. At a distance of about 0.36μm from the interface the mobility appears to be 20-40% lower than in the centre of the layer. There also appears to be significant reductions for slabs inserted close to the surface. The reduction in the mobility near the interface is not surprising because the 14% lattice mismatch introduces a high density of dislocations close to the interface. The mobility should therefore increase as the position of the doping slab moves away from the interface. On the other hand a loss of carriers amounting to $5 \times 10^{11} cm^{-2}$ to surface states would account for the small drop observed in the apparent

mobility for slabs localised near to the surface.

For slab-doped layers grown under optimum conditions, where compensation is low, the measured carrier concentration agrees to within experimental error with that calculated from the impinging Si flux. At high growth temperatures a simultaneous drop in both the carrier concentration and the mobility is found. This behaviour can be explained by a theoretical analysis based on ionised impurity scattering, using equation (6.43), if it is assumed that silicon is behaving amphoterically. Indeed strong amphoteric behaviour was reported by Glazov and Smirnova [190] who investigated the range of existence of solid solutions of Si in InSb. These workers found predominantly p-type behaviour with a silicon solid solubility limit of $4x10^{19}cm^{-3}$ at $490^{o}C$ and $9x10^{17}cm^{-3}$ at between $350^{o}C$ and $400^{o}C$. Based on the assumption that silicon was only present as an isolated donor (group III site) or acceptor (group V site) the electron concentration measured amounted to only 25% of the silicon concentration. This assumption of isolated impurities may not be valid especially close to the solubility limit since other mechanisms for silicon incorporation close to the solubility limit may be present. For example, in GaAs Si-Si pairing and at least one silicon related defect have been identified [191]. Nevertheless, this study demonstrates that silicon behaves differently in MBE growth and donor concentrations which exceed the apparent solubility limit in solution growth can be achieved.

Although the model for amphoteric behaviour explains well the trend of decreasing carrier concentration and falling mobility with increasing growth temperature and constant silicon flux, the possibility of other mechanisms contributing to the loss of carriers must be considered. Firstly, the sticking coefficient for silicon might decrease from unity as the growth temperature increases. However, a loss of silicon by itself would increase rather than decrease the mobility in the slabs. In this case the drop in mobility would then have to occur from other temperature induced defects. There is no evidence for any temperature induced defects in undoped samples. Secondly, thermally activated diffusion of the silicon might occur along the high density of threading dislocations. However, if the scattering from dislocations become important with decreasing carrier concentration, the observed mobility would decrease. In homoepitaxial material the dislocation density is extremely low so that the dislocations cannot act as rapid diffusion paths for the silicon or as sources for scattering. Samples IC92

and IC93 were homogeneously-doped homoepitaxial InSb grown under identical conditions with the exception of the substrate temperature; IC92 was grown at T_T+50°C and IC93 at T_T-30°C. The silicon flux was chosen to give a silicon concentration of $2x10^{18}cm^{-3}$. With the substrates being p-type it is expected that the conduction of the substrate would be only a few percent of the doped layer and there would also be some isolation provided by the p-n junction at the interface. Nevertheless, there will be some contribution from parallel conduction. The sample grown at low temperature (IC93) showed the carrier concentration expected but the sample grown at a nominal temperature of T_T+50°C showed reductions in both the carrier concentration and the mobility. These results therefore, suggest that niether diffusion of silicon down dislocations nor a decrease in the sticking coefficient of silicon with increasing temperature is significant or can explain the main features of figure 7.8. The amphoteric model does however explain the observed behaviour quite well.

7.2.3 Low Field Magnetoresistance

Low field magnetoresistance measurements on slab-doped InSb samples were performed to investigate the electrical quality of the epilayers. With a homogeneously distributed and completely degenerate electron gas occupying a single band with spherical constant energy surfaces, both the longitudinal and transverse magnetoresistance are zero to first order. In InSb, anisotropic terms in the conduction band are small until $n \gg 10^{18}cm^{-3}$ [192] and the Fermi temperature is large for $n \geq 10^{17}cm^{-3}$. Consequently any observation *of* magnetoresistance can be related to electrical inhomogenieties within the sample. In particular, parallel conduction can give rise to a large transverse magnetoresistance with associated errors in the determination of mobility and carrier concentration. In the longitudinal configuration any local variation in the conductivity which causes the current lines to diverge will result in a non-zero magnetoresistance. This provides a sensitive test for macroscopic inclusions of differing conductivity but in a layered system there will be no magnetoresistance because there will be no current flow perpendicular to the magnetic field.

Table 7.4 lists the results taken at 77K with samples in the form of Hall bars as shown in figure 6.3b. These measurements were performed by J Laverty as part of his MSc project [193]. The resistance changes in the longitudinal orientation represent the maximum change observed up to 0.25T. The changes

in the transverse orientation are for a field corresponding to a Hall angle $\mu B = 0.25$ where the transverse magnetoresistance is to a good approximation quadratically dependent on the magnetic field.

These results show an extremely small longitudinal magnetoresistance indicating essentially zero fluctuation in the conductivity within the plane of the layers. This means that any stacking faults and twins are having negligible distorting effect on the current lines. A negative longitudinal magnetoresistance whose magnitude decreases with increasing carrier concentration is observed at extremely low fields. Such a negative component could arise from spin-dependent scattering or from localisation effects. Alternatively scattering from dislocations could play a role as suggested by Broom [194].

The transverse magnetoresistance which to a good accuracy is proportional to μ^2B^2 is observed to decrease with increasing carrier concentration from approximately 0.7% for $1x10^{17}cm^{-3}$ to 0.1% for $2x10^{18}cm^{-3}$. This trend could arise from the greater influence of parallel conduction from the undoped

Sample	Carrier Conc. ($10^{17}cm^{-3}$)	Mobility (77K) (m/Vs)	Slab Position	Growth Temp. (^{o}C)	Magnetoresistance (%) Transverse (μB=0.25)	Magnetoresistance (%) Longitudinal (0.25T)
69	1.3	4.68	1/2	T_T-30	0.6	-0.08
61	1.7	3.13	1/2	T_T-50	0.8	-0.052
64	2.7	4.04	1/2	T_T-30	0.5	+0.54
71	20.0	2.2	1/2	T_T-40	0.1	+0.03
67	1.2	1.34	1/4	T_T+50	1.4	-0.089
57	1.9	2.66	1/4	T_T+50	1.1	-0.09
56	0.96	1.18	3/4	T_T+50	4.3	-0.15
66	0.82	1.17	1	T_T+40	2.1	-0.66

Table 7.4 Values of the transverse and longitudinal magnetoresistance for some Si slab-doped InSb/GaAs samples.

regions, a surface accumulation region or the highly dislocated interface in the more lightly doped samples as opposed to the heavily doped layers. The transverse magnetoresistance is small in the slab-doped samples when the slabs are positioned at the centre of the layer and larger when the slab is closer to the interface between the InSb epilayer and the GaAs substrate. Near to the interface the mobility falls significantly and parallel conduction from the undoped region of the layer may give rise to the observed increase in the magnetoresistance of these samples. These results suggest that there should be some correction to the mobility due to parallel conduction even when the slab is at the centre of the epilayer for $n < 2x10^{18}cm^{-3}$. For $n > 2x10^{18}cm^{-3}$ the corrections will be small.

7.2.4 The Shubnikov-de Haas Effect in Slab Doped and Homogeneously doped InSb

Figure 7.9 shows very pronounced Shubnikov-de Haas oscillations observed when the magnetic field is applied perpendicular to the slab-doped sample with a high carrier concentration ($n \cong 3x10^{18}cm^{-3}$ or $3.6x10^{13}cm^{-2}$). Because of the low electron effective mass and the relatively thick slabs, many subbands will be occupied. On a parabolic model it is estimated that approximately ten subbands will be occupied. Above 6T the diameter of the cyclotron orbits becomes less than the slab thickness and hence the system effectively becomes three dimensional. The carrier concentration deduced from the period of the peaks above 6T agrees well with the carrier concentration deduced from low field Hall measurements. Figure 7.10 shows an expansion of the oscillations in the low field region. This shows the presence of several series of peaks as would be expected from a system in which a large number of subbands are occupied.

The results of applying the magnetic field parallel to the sample is shown in figure 7.11. Again the peaks above 6T form a continuous series similar to those found in the perpendicular orientation. Indeed, the positions of these peaks are almost identical. However, the low field peaks are radically different in character and extend to remarkably low fields with oscillatory behaviour starting at about 0.2T. Instead of having the familiar 1/B dependence, the separation of the peaks increases only slowly with field. Qualitatively the same differences between peaks were observed with B in the two orientations for samples with lower carrier concentrations.

The most likely explanation for this behaviour lies in the diamagnetic emptying of the higher order subbands with increasing magnetic field [195]. The seven peaks at low field would therefore correspond to the emptying of seven subbands. These oscillations may also be complicated by the modification of the density of states by skipping orbits formed at the edge of the well (the mean free path is more than an order of magnitude greater than the well width) and possible size effects leading to a jump in the scattering time when the diameter of the cyclotron orbits become less than the thickness of the slab. These would depend on the smoothness of the effective potential at the edge of the well.

Figure 7.12 shows the Shubnikov-de Haas oscillations for a homogeneously doped InSb/InSb sample (IC43) with the magnetic field perpendicular to the sample. The peaks form a distinct series periodic in reciprocal B as can be seen from the associated Fourier transform. Using equation (6.63) a free carrier concentration of $8.1\times10^{16}cm^{-3}$ can be deduced as compared with an expected carrier density of $1.4\times10^{17}cm^{-3}$ and an apparent Hall carrier concentration at 77K of $3.1\times10^{16}cm^{-3}$. This is not surprising since the sample was grown at a nominally high temperature of $T_T+50^{o}C$ and from the results above, silicon would be incorporated both as donors and acceptors. The Hall carrier density includes the effect of parallel conduction involving the p-type substrate. Shubnikov-de Haas oscillations were also observed for homogeneously doped InSb grown on GaAs (IC60). As shown in figure 7.13. spin splitting can clearly be observed. The carrier concentration derived from these oscillations ($8.5\times10^{16}cm^{-3}$) agrees well with that measured from low field Hall measurement ($8.2\times10^{16}cm^{-3}$). However, as with IC43 the carrier density is lower than expected and again this can be explained by the amphoteric behaviour of silicon.

7.3 P-type Doping in InSb

Beryllium doping was used to produce p-type epilayers. With InSb, hole concentration up to $2\times10^{19}cm^{-3}$ was achieved with mobility in the region of 500 $cm^{2}V^{-1}s^{-1}$, identical to bulk mobility with the same hole concentration.

7.4 Electrical Properties of InAs grown on GaAs

In spite of the 7% lattice mismatch between InAs and GaAs, high quality InAs epilayers have been grown on GaAs substrates. The use of semi-insulating

substrates allows for easy electrical assessment of the epilayers since, like InSb, InAs is not available in an insulating form. This section presents the results of Hall measurements on InAs epilayers of varying thicknesses grown on GaAs. During this study, the growth of InAs was carried out as an initial step towards the growth of its alloy with InSb, i.e. InAsSb.

As a result of the high dislocation densities that exist at the interface of such a lattice-mismatched system, the electrical conductivity may depend strongly on the distance from the interface as in the case of heteroepitaxial films of InSb on GaAs [49]. In addition a two-dimensional electron gas (2DEG) can also form at the interface [196] resulting in parallel conduction within the epitaxial layer. The presence of surface accumulation or depletion resulting from surface states can also affect the electrical conductivity of the sample. Surface accumulation is known to exist in InAs [72] and as a result, the electrical parameters deduced from Hall measurements have to be corrected to take account of these effects.

The apparent Hall mobility and carrier concentrations are listed in table 7.5 for three InAs samples having thicknesses of 2, 3 and 5μm together with

Sample Number	Epilayer Thickness (μm)	Silicon Conc. (cm^{-3})	n_{hall} 300K (cm^{-3})	n_{hall} 77K (cm^{-3})	μ_{hall} 300K (m^2/Vs)	μ_{hall} 77K (m^2/Vs)
100	2	-	$1x10^{16}$	$4x10^{15}$	1.25	3.7
99	3	-	$1x10^{16}$	$3.5x10^{15}$	1.4	5.7
106	5	-	$5x10^{15}$	$1.7x10^{15}$	1.7	8.0
122	2.6	$1x10^{18}$	$9.5x10^{17}$	$9.5x10^{17}$	1.0	1.1
123	3.5	$1.7x10^{19}$	$1x10^{19}$	$1x10^{19}$	0.3	0.3
127	2.4	$5x10^{19}$	$4x10^{19}$	$4x10^{19}$	0.17	0.17

Table 7.5 Hall mobilities and carrier concentrations of undoped and homogeneously doped InAs.

the electrical properties of homogeneously doped InAs samples. These values were obtained using a magnetic field of 0.01T, sufficiently low to assume the condition μB (SI units)« 1. Figure 7.14 shows the temperature variation of the mobility and carrier concentration for the 3μm sample. The 2 and 5μm samples follow the same trend. These results indicate that the apparent room temperature mobility is decreasing with decreasing thickness and more important the values are very much less than the bulk phonon limited value of 24,000 $cm^2V^{-1}s^{-1}$. In addition, the apparent 77K Hall mobility falls from 85,000 $cm^2V^{-1}s^{-1}$ for the 5μm sample to 35,000 $cm^2V^{-1}s^{-1}$ for the 2μm thick sample.

It has been known for some time that InAs suffers from a high concentration of surface states which produce a low-mobility electron accumulation layer. Unless corrections are applied to account for the resulting parallel conduction, electrical measurements will produce erroneous values of carrier concentration, a bulk mobility which apparently decreases with decreasing sample thickness and a very high transverse magnetoresistance. Wieder [72], applying parallel conduction to the analysis of electrical data, showed that even for relatively thick (17μm) InAs films grown on GaAs by vapour phase epitaxy, corrections as large as 30% and 11% have to be applied to the Hall carrier concentration and mobility respectively. It can therefore be concluded that large corrections for surface conduction must be applied to the figures quoted in table 7.5 which are taken for relatively thin films.

Far-infrared magneto-optical studies on these samples revealed the existence of both a low mobility electron accumulation layer and a high mobility bulk region [73]. However these studies cannot provide evidence as to whether the accumulation layer is at the InAs-GaAs interface or at the surface. Analysis of the cyclotron resonance linewidths have shown that the bulk carriers possess mobilities in the range of 200,000 $cm^2V^{-1}s^{-1}$ and 350,000 $cm^2V^{-1}s^{-1}$ and the 2DEG mobility of around 20,000 $cm^2V^{-1}s^{-1}$. The fall in the apparent Hall mobility with decreasing layer thickness can therefore be explained by the increasing dominance of parallel conduction of carriers in the 2DEG.

Silicon in InAs appears to act only as a donor and a free carrier concentration as high as $4x10^{19}cm^{-3}$ have been obtained with 77K mobilities of 2,000 $cm^2V^{-1}s^{-1}$. This already represents an order of magnitude greater than the solubility limit for Si in InSb.

7.5 Hall Results of InAsSb

Table 7.6 lists the results of the electrical properties of $InAs_xSb_{1-x}$ for various samples having different alloy composition. These results indicate a trend between apparent carrier concentration and mobility with composition. The carrier concentration appears to increase with composition, goes through a maximum then decreases again. This trend is similar to that deduced by Rogalski *et al* [197] for the intrinsic carrier concentration of $InAs_xSb_{1-x}$. However, the values at 300K shown in table 7.6 appear to be higher than those calculated by these workers; in some cases by as much as 2 orders of magnitude. The mobility also is lower than expected for such narrow bandgap materials.

These low mobilities may be a result of the growth conditions used for layer growth. It should be noted that these layers represent the first attempt at growing alloys of InAs and InSb. As a result the growth conditions have not been optimised in terms of the electrical properties. These samples were grown at a substrate temperature of 370°C chosen to be a compromise between the growth temperatures of InAs and InSb. One possibility that could account for the low mobilities and high carrier concentrations is parallel

Sample	Composition (x) (%As)	n_{hall} (300K) (cm^{-3})	μ_{hall} (300K) (m^2/Vs)	n_{hall} (77K) (cm^{-3})	μ_{hall} (77K) (m^2/Vs)
121	20	$7x10^{16}$	0.85	$4x10^{16}$	0.25
118	40	$4.1x10^{17}$	0.2	$3.3x10^{17}$	0.1
124	60	$1.4x10^{18}$	0.1	$1x10^{18}$	0.08
119	80	$2.1x10^{17}$	0.45	$1.5x10^{17}$	0.27

Table 7.6 Electrical properties, obtained from low field Hall measurements, for $InAs_xSb_{1-x}$ layers grown using a substrate temperature of 370°C.

conduction, either with a surface accumulation region similar to InAs and/or with the 1/2 μm undoped InAs buffer layer at the interface between the substrate and epilayer. Another possibility is that alloy ordering which has been reported in TEM diffraction studies [198] is affecting the mobility.

Although the growth of InAsSb has been reported in various publications (see chapter 2) no systematic study has been carried on the electrical properties of this material over the complete compositional range. As a result, it is difficult to say whether these results represent bad quality material. Nevertheless, these results are encouraging and with growth optimisation the electrical quality of these materials may be improve still further.

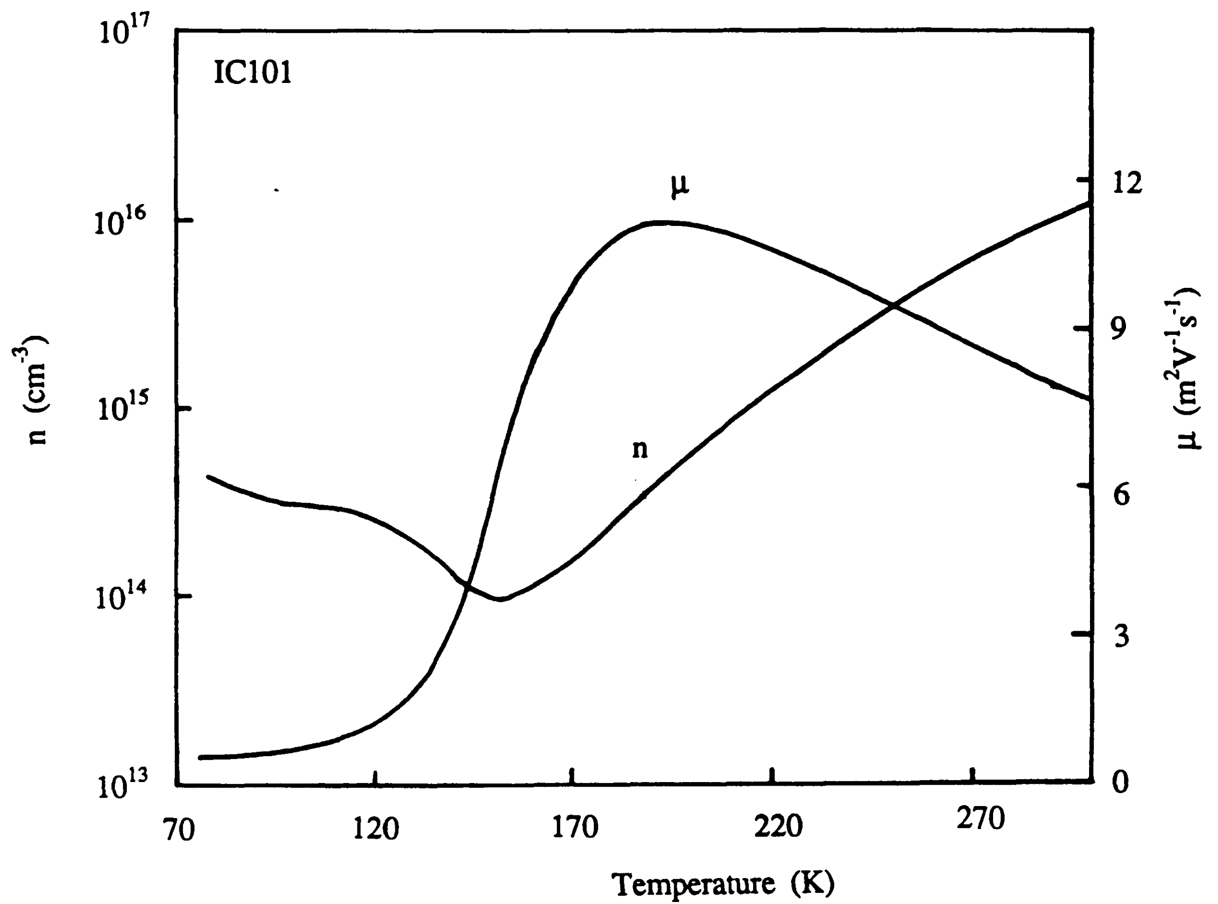

Figure 7.1 Apparent mobility and free carrier concentration as a function of temperature for a 5μm undoped InSb/InSb sample.

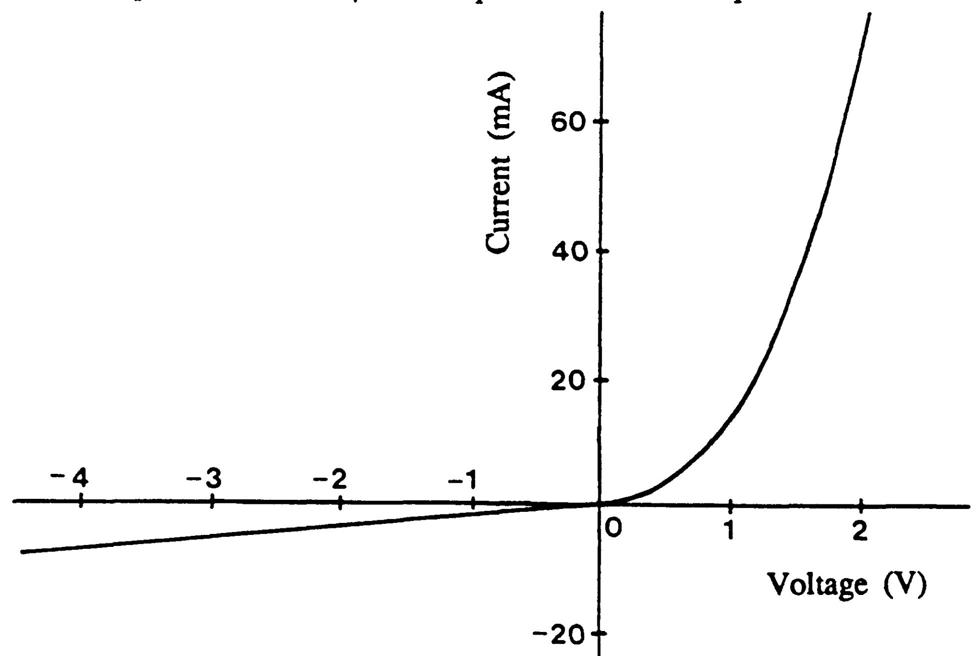

Figure 7.2 A typical I-V plot at 77K showing the existence of a p-n junction between a 5μm undoped epilayer and a p-type substrate.

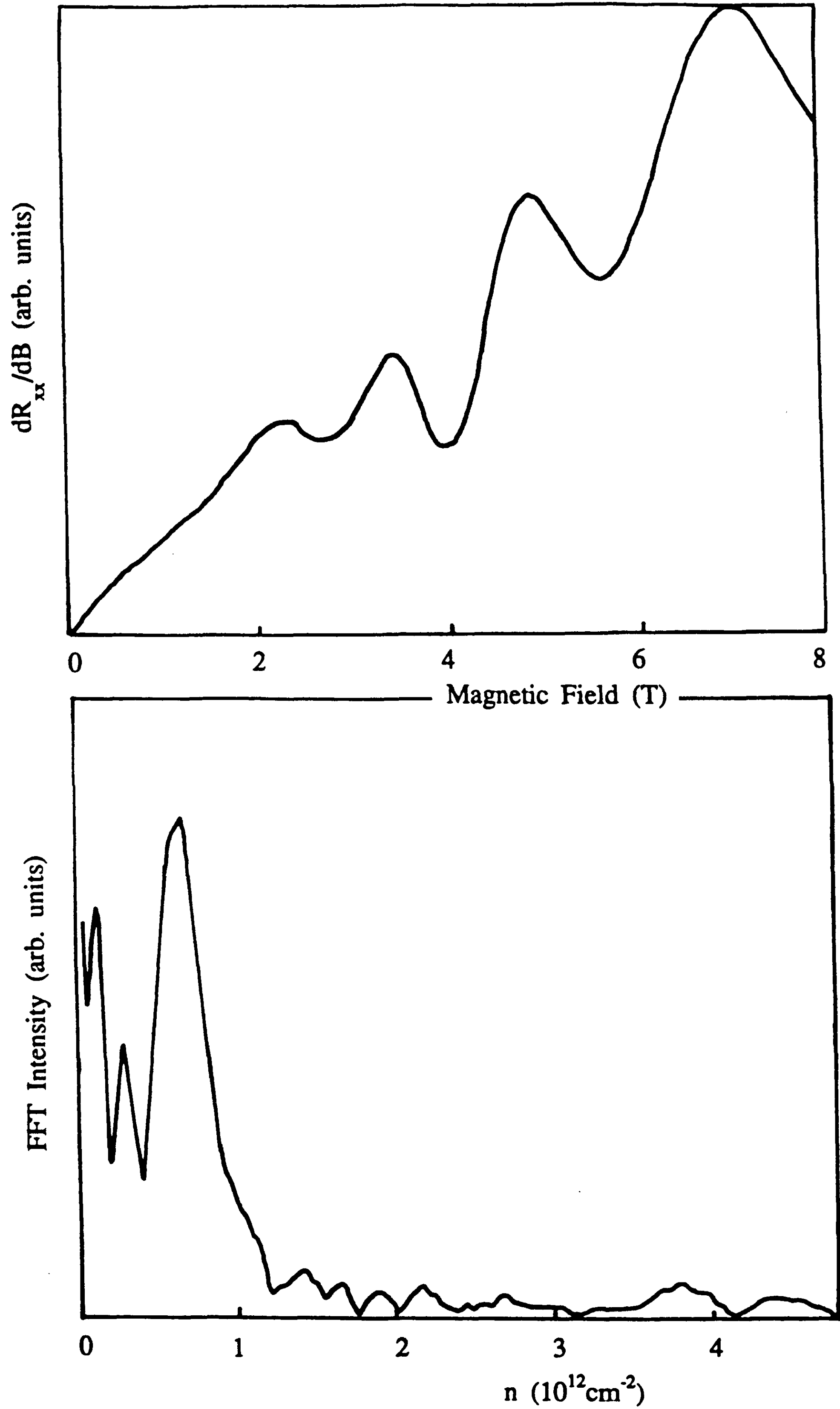

Figure 7.3 First derivative of the magnetoresistance and the associated Fourier transform obtained from a 5μm undoped InSb/InSb sample showing a quasi-2DEG at the interface due to pregrowth argon ion cleaning.

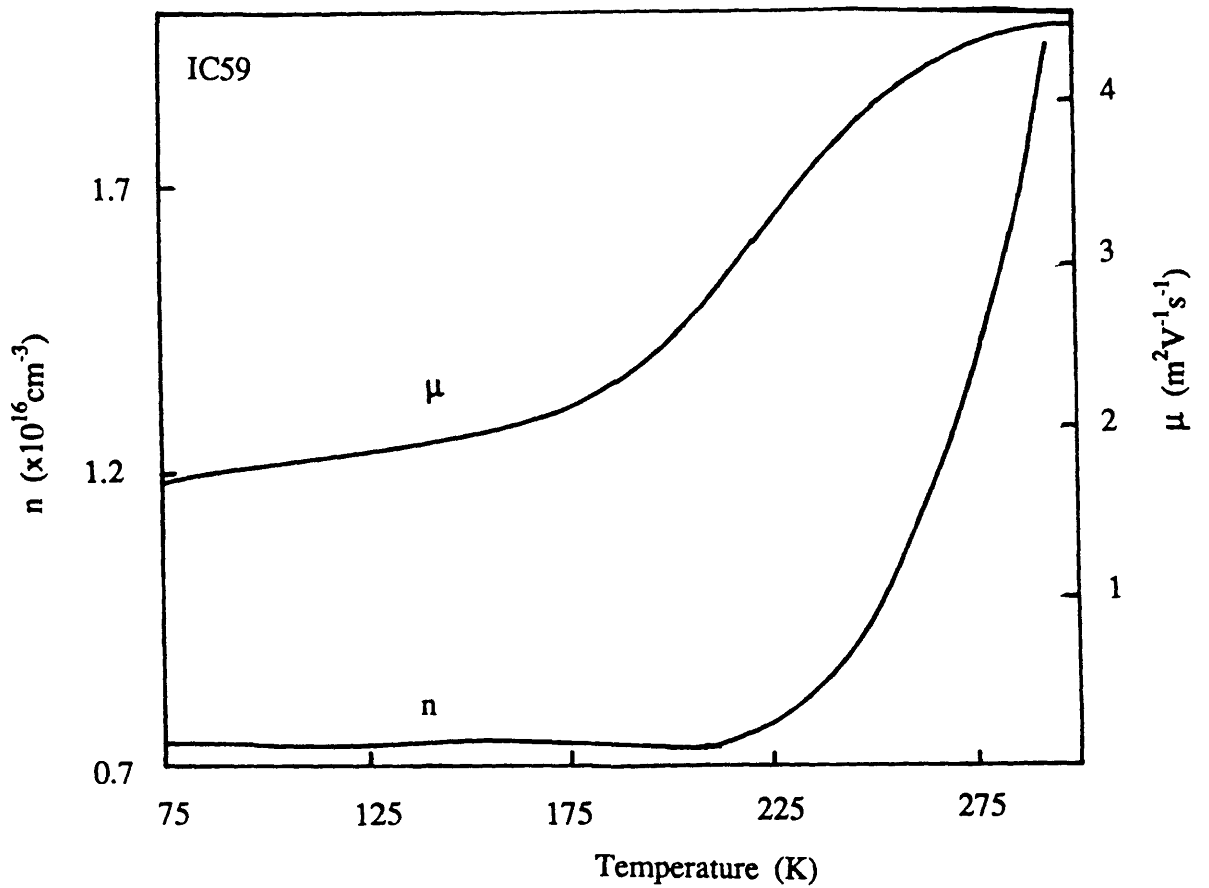

Figure 7.4 Temperature variation of the Hall mobility and free carrier concentration obtained from a 1μm thick undoped InSb/GaAs.

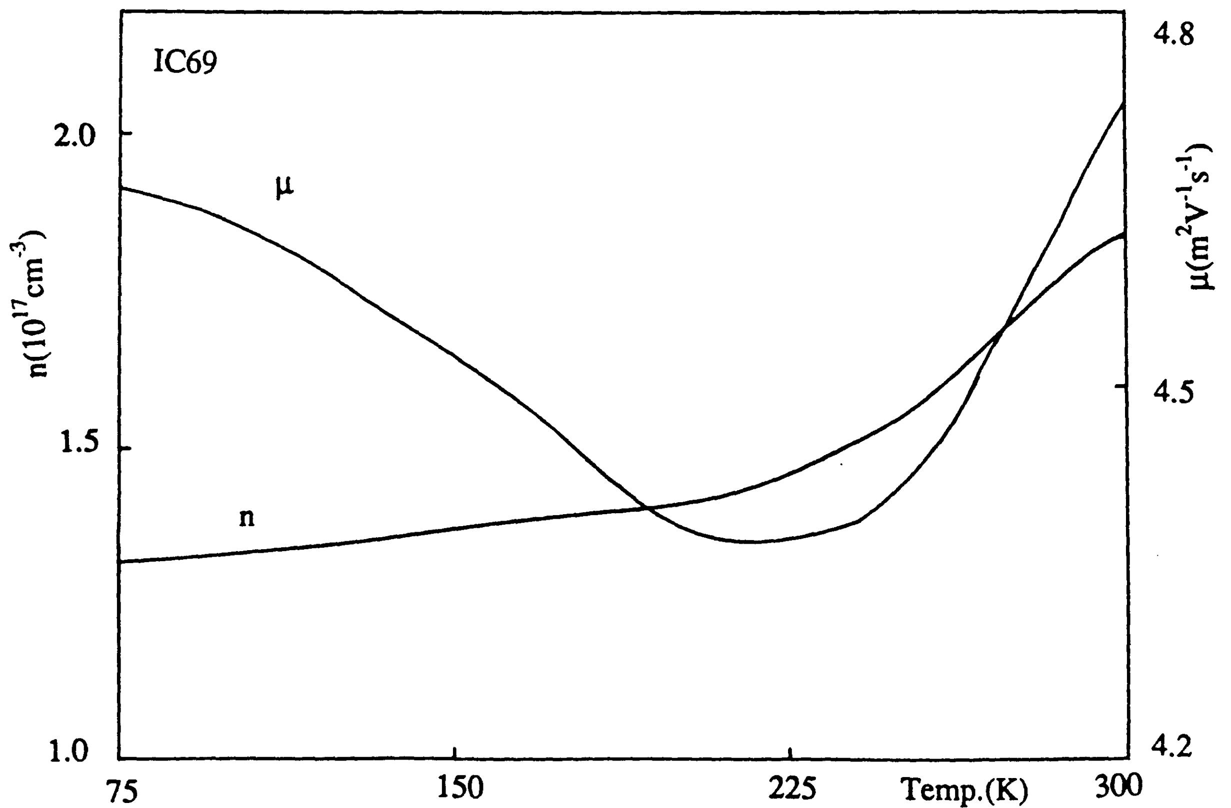

Figure 7.5 Temperature dependence of the Hall mobility and carrier concentration for a Si slab-doped InSb/GaAs sample (IC69).

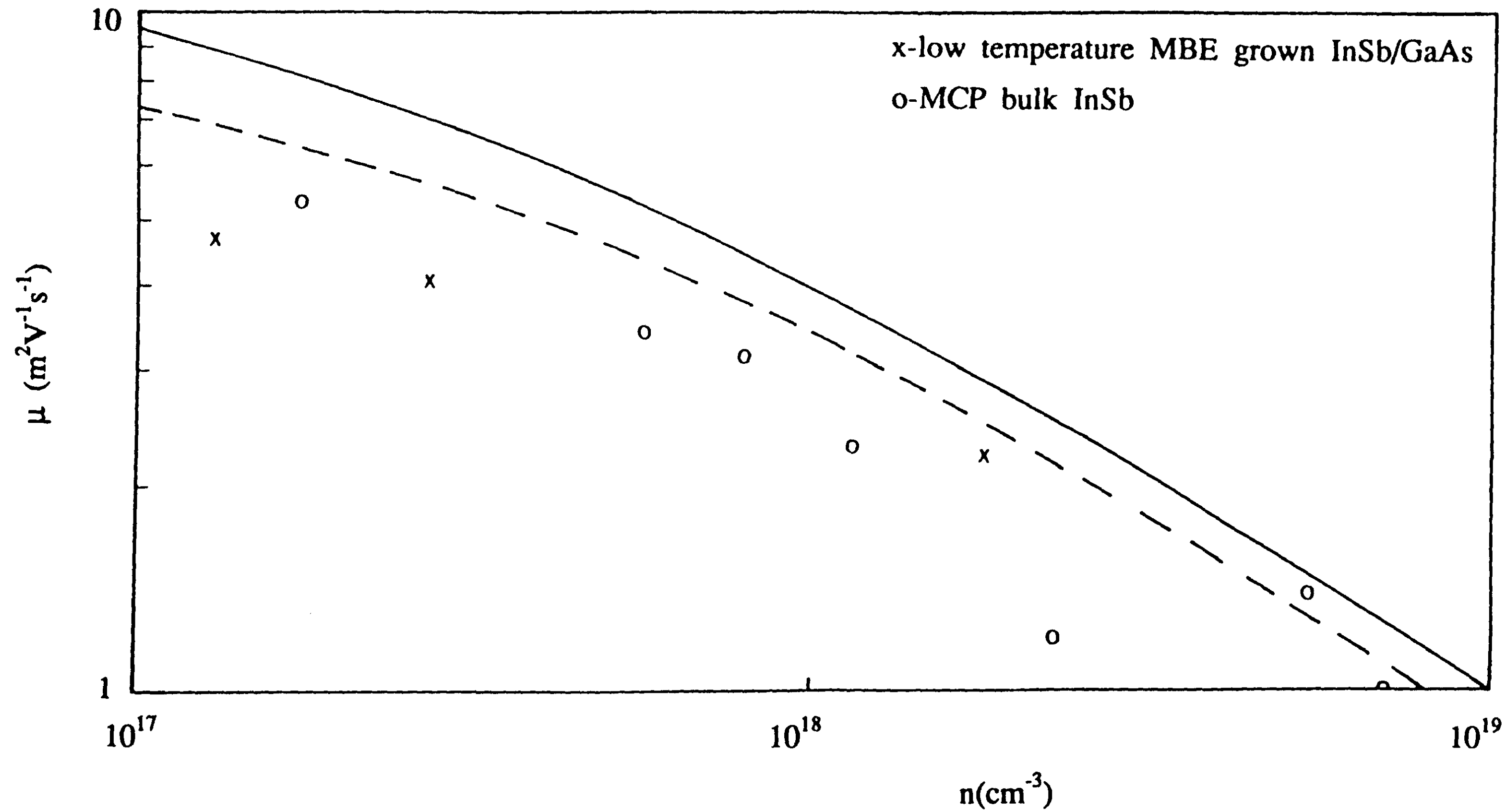

Figure 7.6 Comparison between the mobility data from bulk grown (O) InSb and epitaxial (X) InSb samples grown at low temperatures. The solid curve represents the theoretical dependence of mobility on free carrier concentration calculated using equation (6.43) assuming zero compensation. The broken curve is also calculated using equation (6.43) but includes corrections for phonon scattering.

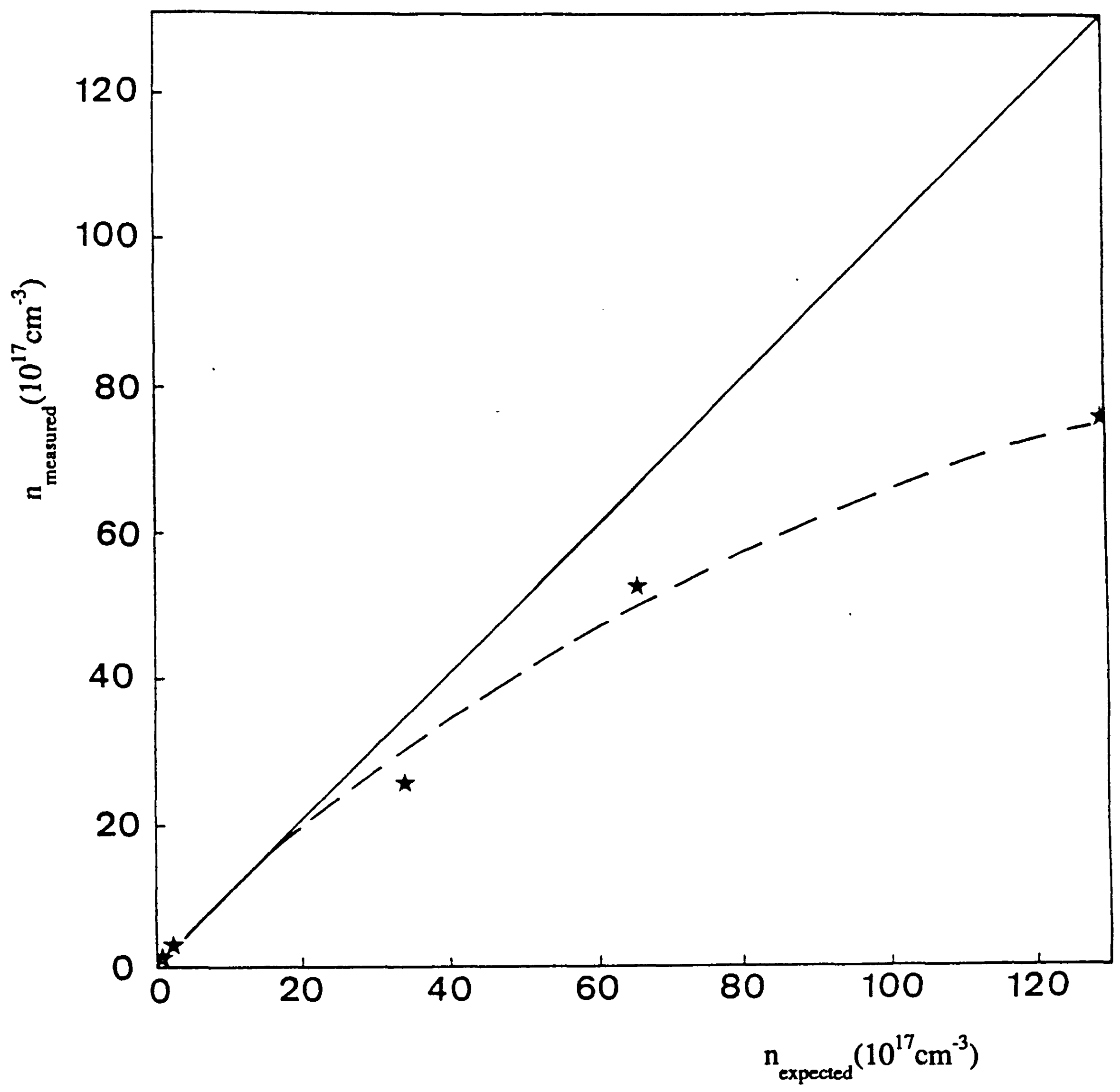

Figure 7.7 Measured carrier concentration against expected carrier concentration for various InSb samples grown at low temperatures.

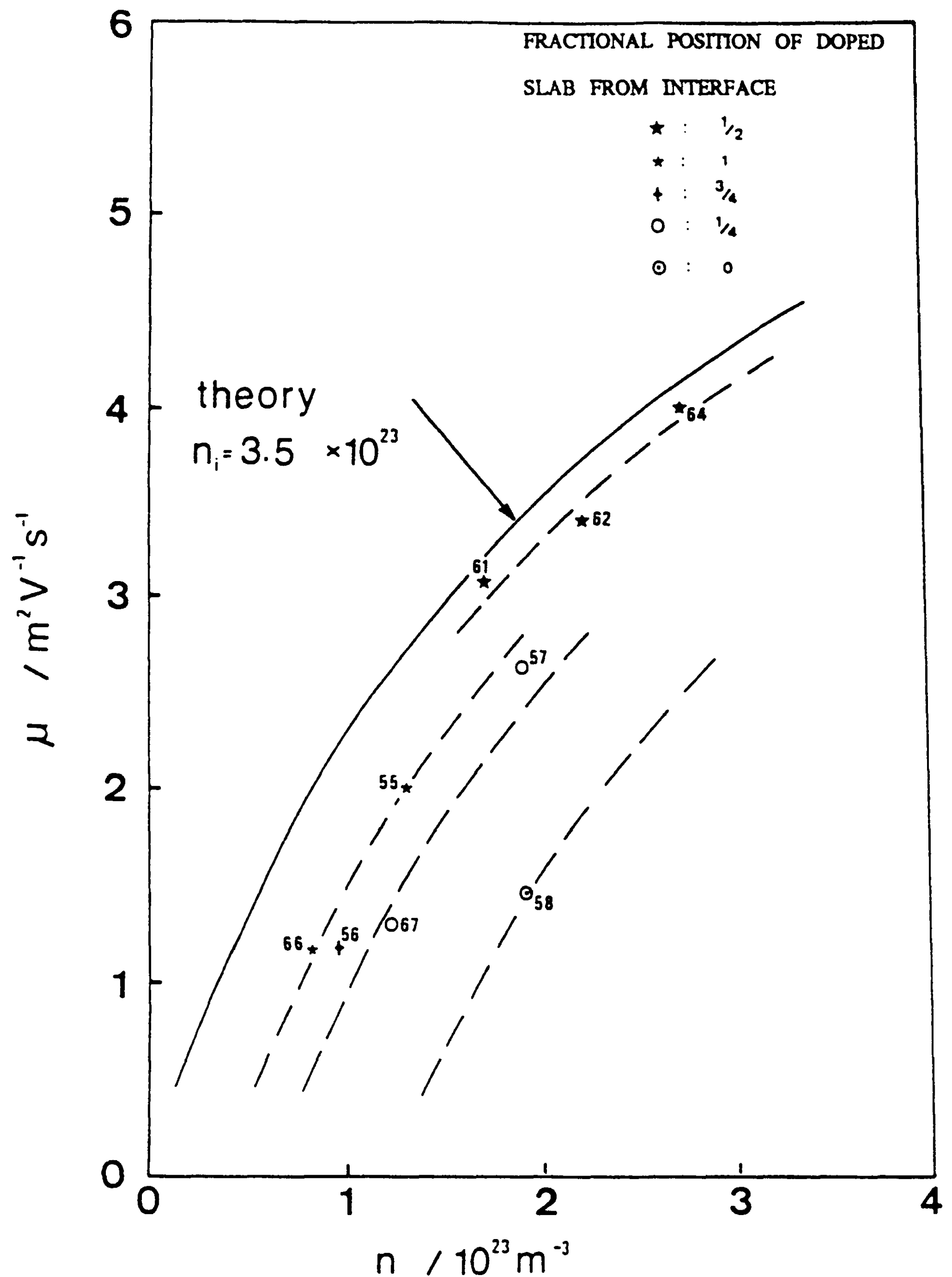

Figure 7.8 Comparison of the theoretical mobility limited by ionised impurity scattering with experimental data from layers grown with a constant silicon flux at different nominal temperatures and with a range of slab positions. The theoretical mobility is calculated by maintaining the total density of scatterers at a constant level in equation (6.43) and allowing the compensation ratio to change. The theoretical curve assumes a slightly higher value for the concentration of scatterers than the flux of silicon to account for discrepancy between theory and experiment. The broken curves are not theoretical curves but are drawn to distinguish the results for doping slabs located at different depth.

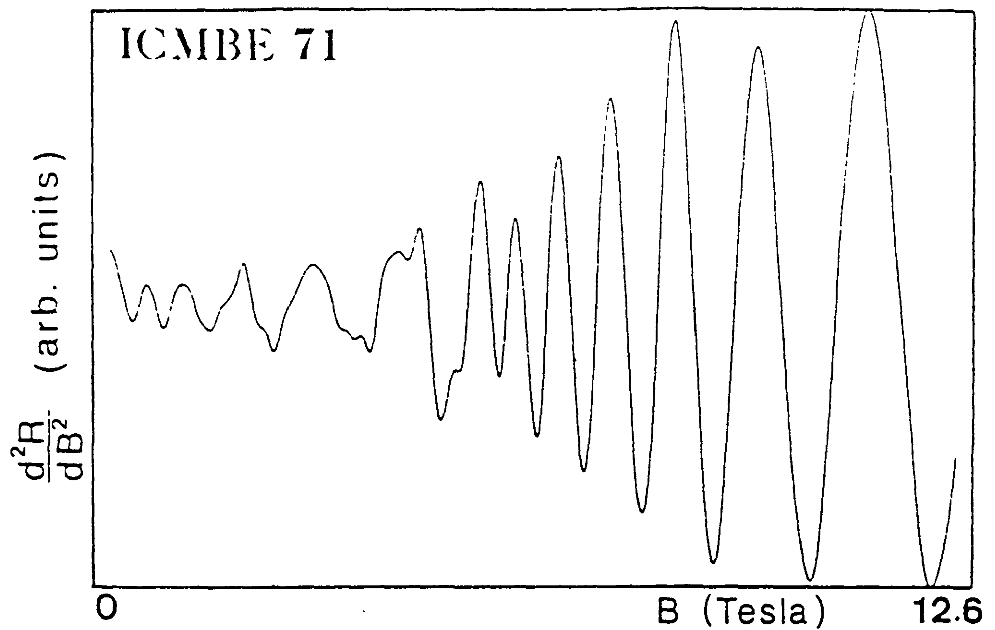

Figure 7.9 Second derivative of the magnetoresistance against magnetic field for a heavily doped slab, 900Å wide ($n = 3X10^{18}cm^{-3}$) within InSb with the magnetic field perpendicular to the slab showing quasi-3D Shubnikov-de Haas oscillations above 6T and 2D behaviour below this field.

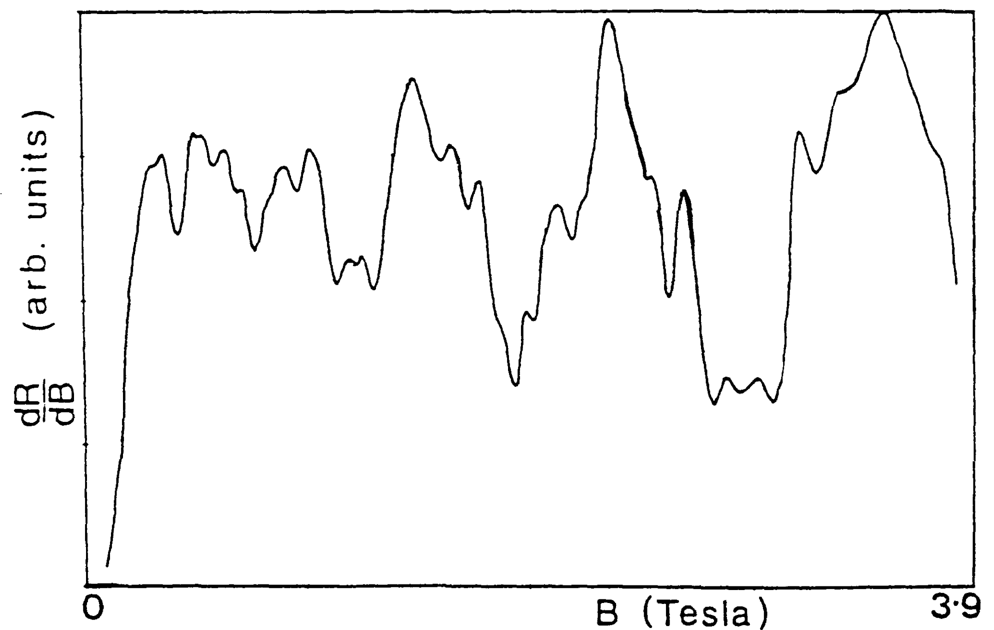

Figure 7.10 An expanded low field plot of the first derivative of the magnetoresistance showing complicated structures due to the occupancy of many subbands obtained for the same heavily doped sample of figure 7.9.

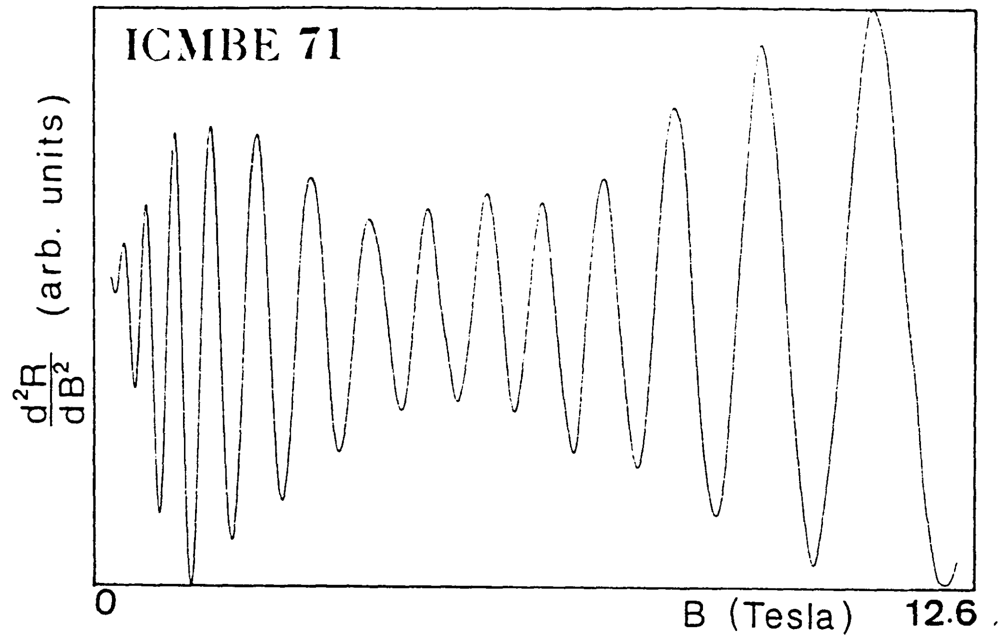

Figure 7.11 The second derivative of the magnetoresistance against magnetic field for the InSb sample used in figure 7.9 with the magnetic field parallel to the plane of the slab. Again quasi-3D behaviour is observed above 6T.

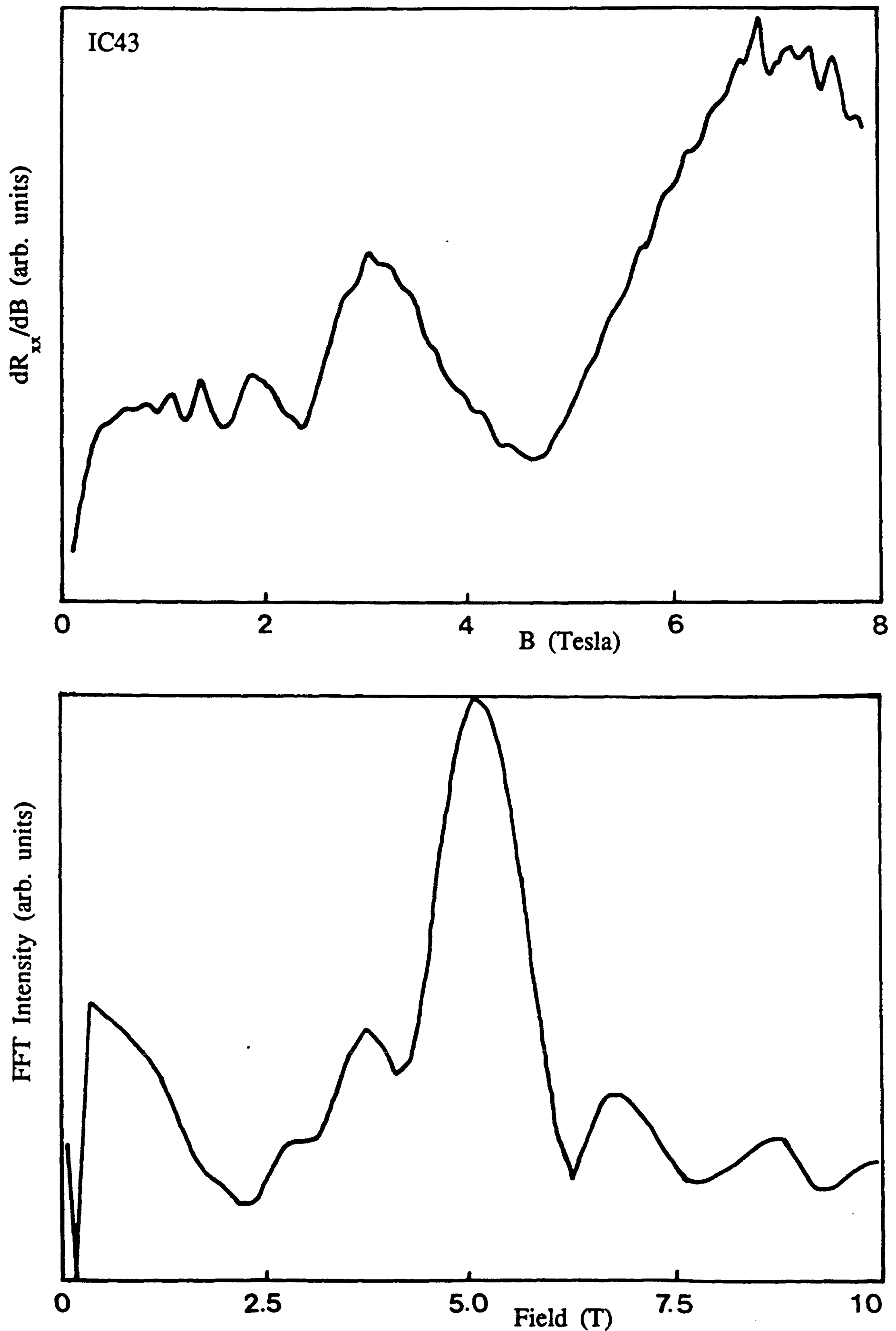

Figure 7.12 The first derivative of the magnetoresistance against magnetic field and the associated Fourier transform for a homogeneously doped InSb/InSb sample.

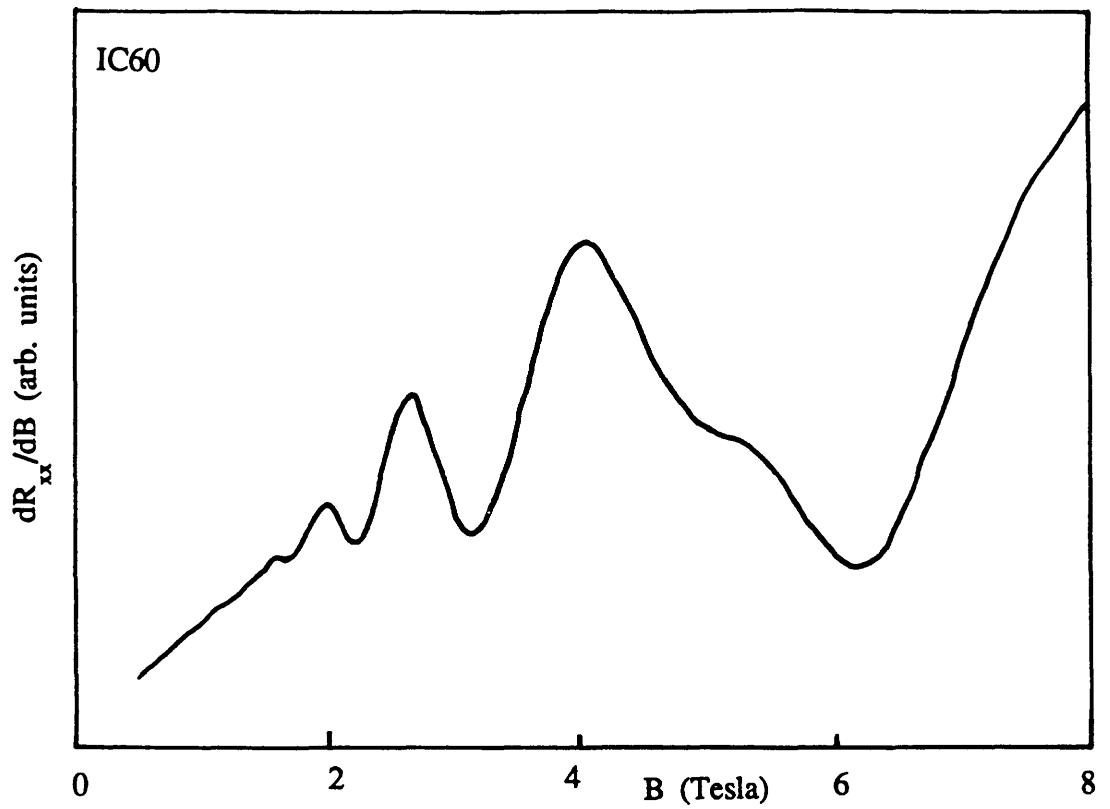

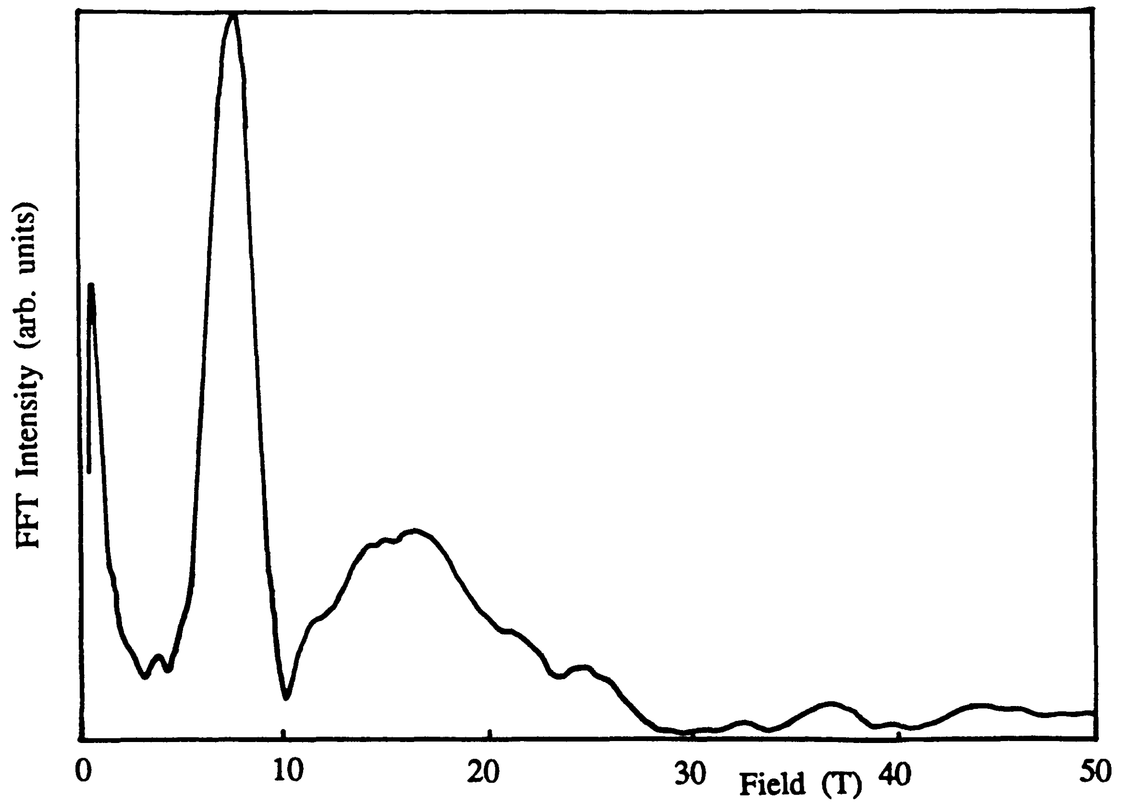

Figure 7.13 The first derivative of the magnetoresistance against magnetic field and the Fourier transform for a homogeneously doped InSb/GaAs sample. For this sample spin splitting can clearly be observed.

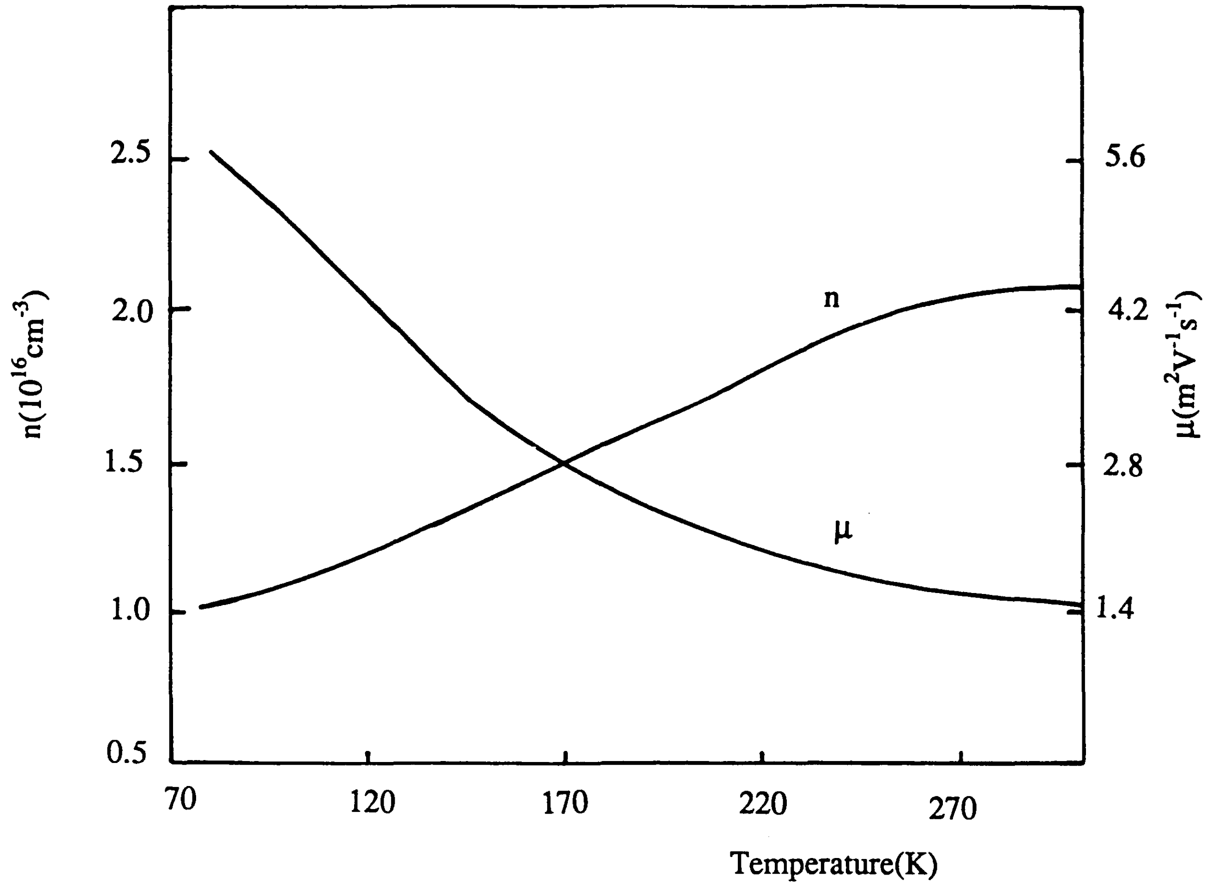

Figure 7.14 Apparent mobility and free carrier concentration against temperature for a 3μm thick undoped InAs epilayer grown on GaAs.

CHAPTER 8 DELTA DOPING AND DOPING SUPERLATTICES

8.1 Introduction

With the development of MBE as an advanced thin film semiconductor growth technology a wide range of doping and composition profiles can now be realised. Because MBE can essentially be a layer-by-layer growth process, doping profiles and heterojunction interfaces as narrow as one atomic layer can in theory, be achieved. One such profile is spike or delta (δ) doping in which the dopant atoms are deposited on a plane of one monolayer in thickness perpendicular to the growth direction. Recently a number of applications have emerged using this doping technique. These include high electron mobility transistors (HEMTs), Schottky gate δ-doped field effect transistor (δ-FET) with improved device characteristics [199,200] and d-i-d-i devices in which the effective bandgap can be reduced and large electrical and optical nonlinearities exist.

Much of the work on delta doping has so far concentrated on Si doped GaAs in which two-dimensional carrier densities as high as $2x10^{13}cm^{-2}$ have been achieved, corresponding to an effective three-dimensional donor concentration nearly an order of magnitude higher than achieved in bulk [201], if it is assumed that there is no diffusion of silicon atoms away from the dopant plane. It was also suggested that highly delta doped GaAs can have a 300K mobility which is about 4 times greater than in bulk material of equivalent 3-dimensional doping density. However, this factor of four enhancement also assumed that there is no diffusion. SIMS measurements performed by Harris *et al* showed conclusively that a concentration dependent diffusion mechanism occurs for Si in GaAs [27]. In particular, when silicon is deposited on a single plane above the solubility limit it can diffuse by as much as 200Å depending on the growth temperature. In comparison, there have been very little studies on delta doping in narrow gap III-V semiconductors such as InSb and InAs. The results so far presented in this study have shown that Si can be used in delta doped InSb in much the same way as it is for GaAs. Although Si acts as an amphoteric dopant in InSb, the results of the previous chapter demonstrate that by suitable choice of growth conditions donor concentration of the order $3x10^{18}cm^{-3}$ can be obtained with virtually zero compensation in homogeneously doped material. Unlike InSb, Si behaves predominantly as a donor in InAs and carrier densities up to $4x10^{19}cm^{-3}$ have been achieved in this study. Delta doping is

usually carried out under suspended growth conditions whereby the group III cell is shuttered off and the surface is left to anneal in the beam of the group V flux. As a result, the dopant can be incorporated solely on the group III sites, enabling, at least in theory, the 3-dimensional solubility limit to be exceeded.

One of the problems associated with δ-doped GaAs grown at normal growth temperatures (~550°C) has been the anomalously high diffusion of silicon resulting in a doping profile which deviates from a true delta function. This tends to limit the maximum achievable free carrier density [202,203]. Silicon diffusion may be less of a problem in δ-doped InSb however, since the growth temperature for InSb is significantly lower (≤340°C).

Delta doping in narrow bandgap semiconductors is potentially useful for the development of novel photodetectors operating in the infrared region. However, for these systems to be fully exploited, fundamental studies on the transport properties of doping wells and superlattices need to be carried out. In this chapter the growth of single wells and superlattices based on delta doping in InAs and InSb will be described. Some of the results obtained from quantum transport studies will also be presented.

8.2 Some Basic Ideas on Delta Doping

Delta doping represents the deposition of dopant atoms during crystal growth to a 2-dimensional plane which ideally would be one atomic layer in thickness. This doping concept was originally proposed, as atomic-plane doping, to eliminate the effects of the temperature variation of the dopant cell so as to improve the doping profiles in n-type GaAs [204]. Atomic-plane doping was achieved by opening the dopant shutter while growth was suspended, under arsenic stabilised conditions. Germanium was used as the dopant and was found to incorporate exclusively on the Ga sites thereby producing n-type material. Sheet carrier densities of $1\times10^{12}cm^{-2}$ was obtained with some evidence for autocompensation. However no attempt was made to study the transport properties of a single dopant sheet of atoms.

Döhler [205] in 1978, originally proposed a system in which an ultrathin doping layer is surrounded by a semiconductor of opposite doping type to study the dynamics of a 2-D electron gas (2DEG) system. The concept of this δ-doping technique in GaAs is illustrated in figure 8.1a. The silicon

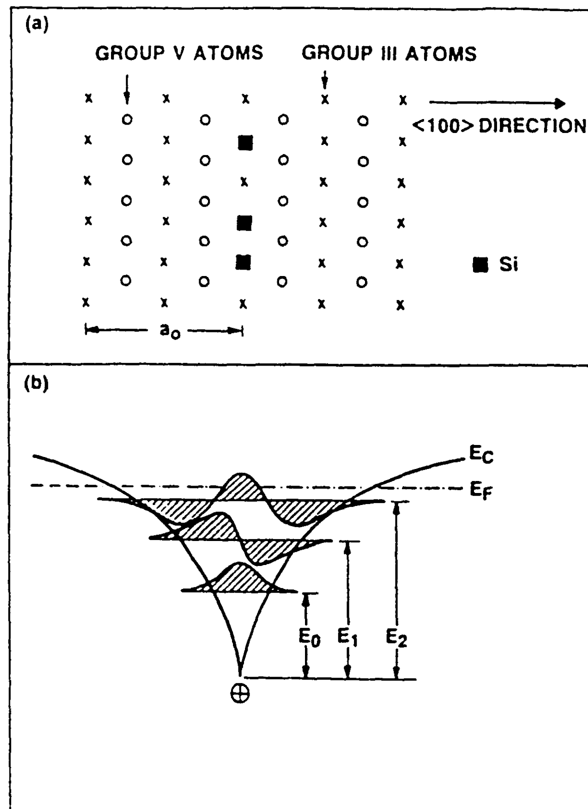

Figure 8.1 (a) Schematic illustration of delta doping in a III-V semiconductor, (b) Energy band diagram of the V-shaped potential due to a sheet of ionised donors. Also shown are the three lowest subbands populated. (after ref. 201)

impurity atoms are located in an atomic monolayer of the (001) oriented host material. The resulting positive sheet of ionised donors form a V-shaped potential well, figure 8.1b, in which a quasi-2DEG exists. In this narrow potential well the electron energies for motion perpendicular to the [001] direction are quantised into 2-dimensional subbands. The first direct evidence for the formation of such subbands in δ-doped GaAs was observed in Shubnikov-de Haas oscillations obtained during magnetotransport measurements with the magnetic field perpendicular to the doping plane [206].

Delta doping has significant advantages over the familiar metal oxide semiconductor (MOS) system in that there is complete confinement of the 2-dimensional gas away from the interface and surface. This eliminates interfacial and surface problems such as the trapping of 2-dimensional charges by interface states and the loss of mobility due to surface roughness scattering. In delta doping the greater confinement of electrons

in the i = 0 subband manifests itself in the electron mobility which can be up to an order of magnitude lower in the lowest subband as compared with higher order subbands. This large difference in the carrier mobility between the lowest, i = 0 subband and the first excited, i = 1 subband can be exploited in device structures based on delta doping.

8.3 Delta doping Studies in InSb and InAs

δ-doping studies in InSb were carried out on 1μm thick samples in which the doping layers were situated midway through the epilayers. The quantum transport experiments were carried out by R.L.Williams and E.Skuras here at Imperial College using one of two superconducting magnets (8T or 13.6T). Semi-insulating GaAs substrates were used. Prior to the growth of the InSb layer, a buffer consisting of a 1/2 μm thick undoped GaAs layer was grown. Doping was achieved by closing the In shutter, annealing for 60 seconds, doping with silicon and annealing for a further 60 seconds before recommencing growth. The silicon cell was kept at a constant temperature of 1165°C, corresponding to a flux of $6.1 \times 10^{10} cm^2 sec^{-1}$ and variations in the doping density were achieved by changing the duration of the doping period during the suspension of growth. The electrical transport properties of these δ-doped layers were investigated using high field Shubnikov-de Haas experiments.

Figure 8.2 shows the perpendicular field Shubnikov-de Haas oscillations and corresponding Fourier transform for sample IC132 having an intended carrier density of $8.2 \times 10^{11} cm^{-2}$. Large oscillations in the magnetoresistance are observed and the structure indicates the occupation of a large number of electronic subbands. Indeed this is shown in the number of peaks present in the Fourier transform. The carrier density for each subbands can be calculated using equation (6.64). If each Fourier peak is to be associated with an occupied subband then the calculated carrier density for sample IC132 is found to be greater than the design doping level by a factor of 3. The first peak (a) is in fact the first harmonic of the i = 0 fundamental. The second peak (b) is a combination of the i = 0 fundamental and the first harmonic of the i = 1 fundamental. Peaks (c) and (d) are the fundamentals of the i = 2 and i = 3 subbands respectively. Using this interpretation the free carrier densities derived for various delta doped InSb samples are shown in Table 8.1. Also shown is the ratio of $N_{i=0}/N_{i=1}$. From these results this ratio is smallest for sample IC126 suggesting the presence of

significant diffusion of silicon away from the doping plane at the growth temperature used. Further evidence for silicon diffusion in this sample is obtained by comparing the Fourier transforms for IC126 with those of IC150, grown at a lower temperature, in figure 8.3. These results suggest that a reduction in the growth temperature from 340 °C to 240 °C has produced a significant increase in the 2-dimensional carrier density and an increase in the intensity of the peak (b) corresponding to the i = 0 fundamental/ i =1 harmonic. This latter observation provides strong evidence for diffusion in IC126 since the increase in intensity indicates an increase in mobility in the i = 1 subband consistent with a reduction in the width of the doping region.

The free carrier densities computed in Table 8.1 are confirmed from the diamagnetic Shubnikov-de Haas oscillations observed when the magnetic field is applied parallel to the sample [195]. These oscillations may be interpreted as a progressive depopulation of subband levels as the parallel magnetic field is increased, due to a diamagnetic energy shift given by,

$$\Delta E(B_{parr}) = e^2/2m^*.\langle z_i^2\rangle B_{parr}^2 \qquad (8.1)$$

where $\langle z_i^2\rangle$ is the average square of the extent of the wavefunction in the z-direction for the ith subband. This diamagnetic shift causes the bands to rise above the Fermi energy, emptying their carriers and redistributing them among the remaining states.

Sample	$N_{intended}$ ($10^{12}cm^{-2}$)	Growth Temperature (°C)	$\Sigma(N_i)$ ($10^{12}cm^{-2}$)	N_0/N_1
126	2.47	340	1.91	1.64
132	0.82	340	0.69	1.96
136	0.41	340	0.38	1.82
145	1.65	340	1.35	2.08
150	2.47	240	2.12	1.80

Table 8.1 Growth parameters and electrical properties of delta doped InSb samples.

The complete depopulation of an electronic subband is accompanied by a reduction in intersubband scattering and a corresponding change in the gradient of the magnetoresistance. Therefore complete subband depopulation is indicated by the minima in the $d\rho/dB$ plot with B applied parallel to the sample. Figure 8.4 shows the diamagnetic Shubnikov-de Haas oscillations obtained for sample IC132. Three depopulation peaks are clearly observed, with a doubling of the structure being observed for the i = 1 subband due to resolved spin splitting. The indexing of the peaks is achieved by comparison of the depopulated fields with the universal predictions of Reisinger and Koch [195] shown in figure 8.5. In their calculations the variation of the depopulated field with free carrier density is predicted to be independent of the material system provided the cyclotron energies are scaled to the effective Rydberg (Ryd^*) and free carrier densities are scaled to the effective Bohr radius (a^*). In figure 8.5, $\gamma=\hbar\omega_c/Ryd^*$ and $\hat{N}_s=N_s a^{*2}$. For InSb $Ryd^*= 0.7meV$ and $a^*= 614\mathring{A}$.

Shubnikov-de Haas oscillations in the perpendicular field configuration obtained from a heavily delta doped InAs sample is shown in figure 8.6 together with the associated Fourier transform. Five subbands are occupied with the sum of the occupancies amounting to $4.5x10^{12}cm^{-2}$ as compared to the intended doping concentration of $\sim 4.9x10^{12}cm^{-2}$.

8.4 Doping Superlattices

Doping superlattices were first proposed by Döhler [13] in 1972 as structures in which the basic electronic properties such as the band gap and carrier concentration can be tuned externally. Such superlattices may consist of periodic regions of n- and p-type doping with the possibility of separation by intrinsic regions (n-i-p-i). In a n-i-p-i superlattice recombination of electrons from donors with holes on the acceptors produces a periodic space charge which modulates the band structure in the host material. The electron and hole states formed are quantised within the n- and p-type regions so that the effective bandgap, that is the energy separation between the highest hole state and the lowest electron state can be varied by the appropriate choice of doping level and superlattice period. The tunability of the electronic properties of a n-i-p-i superlattice is a consequence of this indirect bandgap in real space resulting from the modulation of the conduction and valence band edges by the periodic impurity space charge potential. Because of the spatial separation between the

electrons and holes the electron-hole recombination lifetimes may exceed the corresponding values of unmodulated bulk material. The predictions of the tunability of the electrical properties of n-i-p-i superlattices have been confirmed experimentally by Ploog *et al* [207] on a n-i-p-i structure in GaAs with Be and Si as a p-type and n-type dopant respectively.

During this study various doping superlattice structures were grown on InSb to investigate the possibility of producing high sensitivity 10μm detectors. One of these structures is shown in figure 8.7. After argon ion sputtering and thermal annealing the InSb substrate is transferred into the growth chamber as described in chapter 5 for the growth of homoepitaxial InSb epilayers. During buffer layer growth the substrate temperature is calibrated and the growth rate and antimony flux are measured using RHEED intensity oscillations. Using the growth rate and the calibration curves for the dopant cells (figure 5.3b), the Si and Be cell temperatures are determined to give the required dopant concentrations. For the doping densities given in figure 8.7 the temperatures are 1145 $^{\circ}$C and 777 $^{\circ}$C for the Si and Be cells respectively. The growth of the superlattice structure is then initiated, and subsequently controlled by the resident computer using a set of parameters programmed into the growth recipe.

The results of photoconductivity and optical absorption experiments on the sample shown in figure 8.7 indicate that there is a bandgap reduction of ~60meV (corresponding to a reduction of 25% at 77K) with enhanced carrier lifetimes [208].

Although n-i-p-i structures described above are useful for bandgap tuning and enhanced carrier lifetimes, rapid band modulation can be achieved by employing delta doped planes in place of the n- and p-type regions to produce a d-i-d-i superlattice. Although rapid band modulation can be realised with delta doping, the large real space overlap of adjacent electron and hole wavefunctions would lead to a reduction in the carrier lifetimes. It was shown however, that such rapid band modulation and lower carrier lifetime can result in an effective bandgap that is stable over a wide range of luminescent excitation intensities [200].

Following on from the studies on delta doping in InSb, d-i-d-i superlattice structures were grown. Although the aim was to achieve 100% compensation, the results of Shubnikov-de Haas measurements indicate that there are more

n-type carriers than there are p-type in nearly all of these superlattices grown. Whether this is due to unequal doping densities or some other mechanism producing excess n-type carriers is still to be investigated.

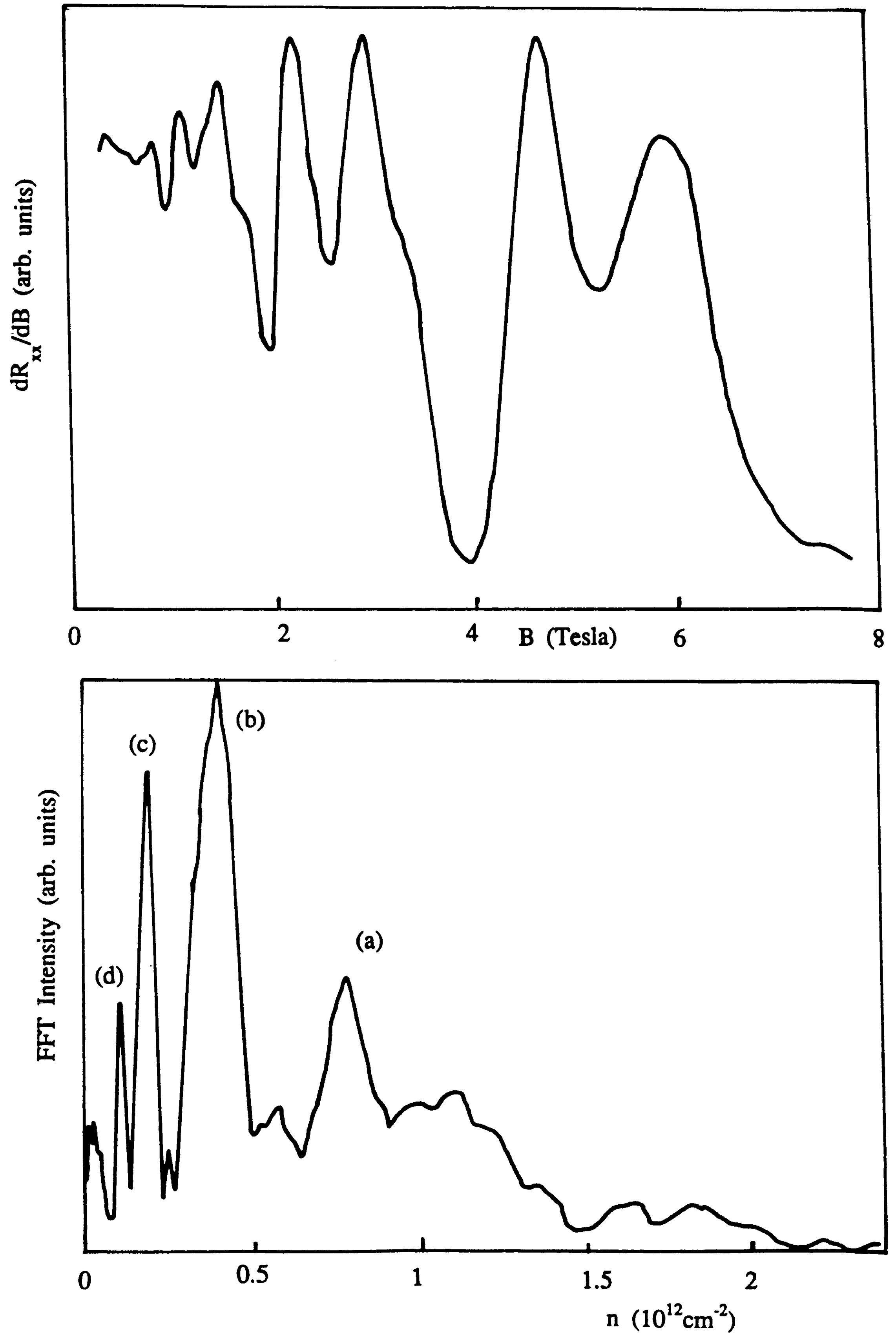

Figure 8.2 First derivative of the magnetoresistance in the perpendicular orientation together with the Fourier spectrum for sample IC132 grown with a nominal Si concentration of 8.2×10^{11}cm^{-2}.

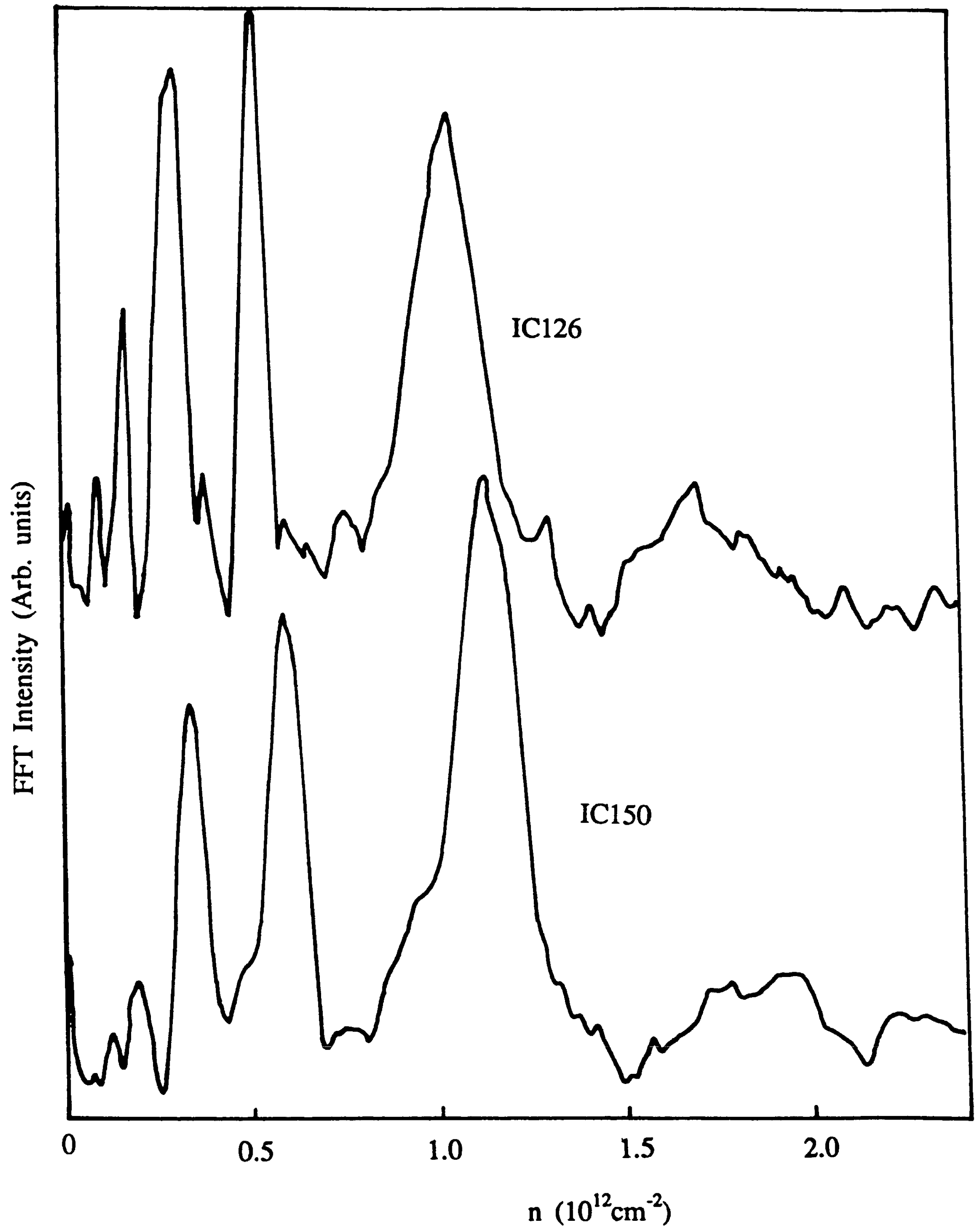

Figure 8.3 Comparison of the Fourier spectra for samples IC126 and IC150 grown with the same nominal silicon concentration (2.5×10^{12}cm^{-2}) but at different temperatures. The sample grown at the lower temperature (IC150 at 240°C) show a significant increase in the carrier densities in the lower subbands as compared to IC126 grown at 340°C.

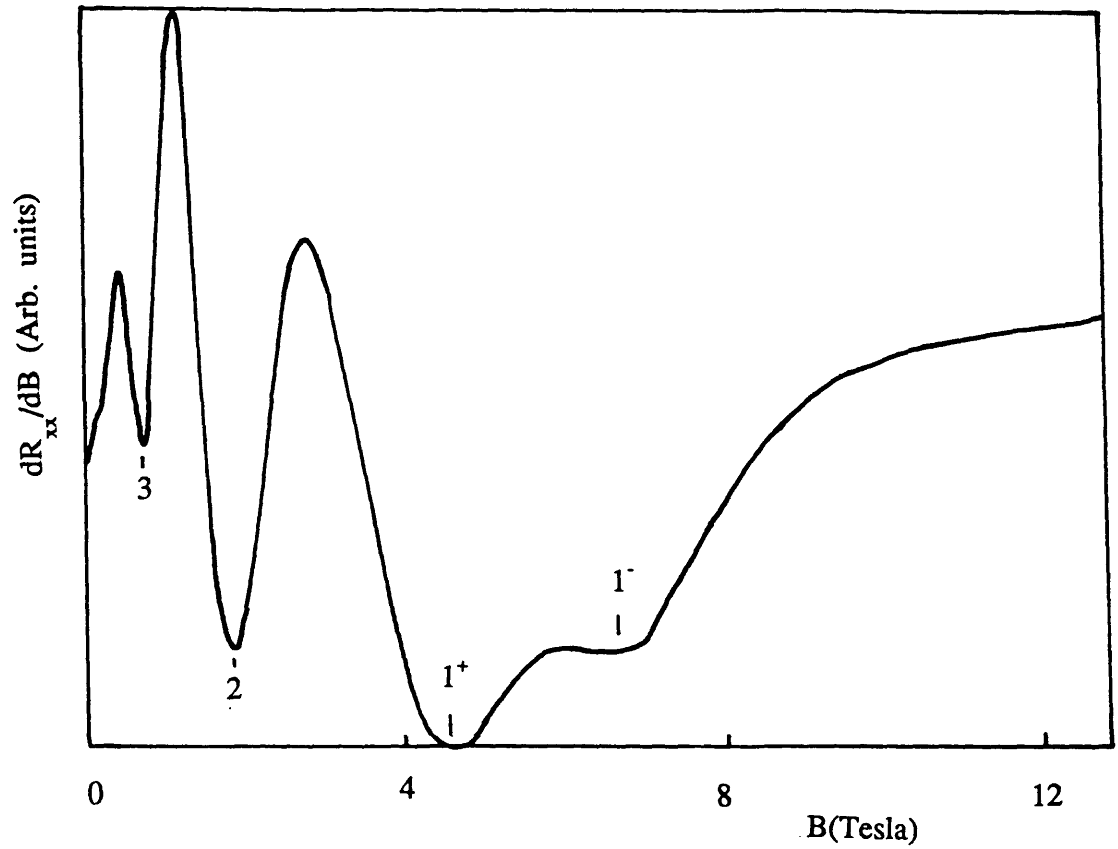

Figure 8.4 Shubnikov-de Haas oscillations obtained from sample IC132 with the magnetic field parallel to the sample plane showing subband depopulation.

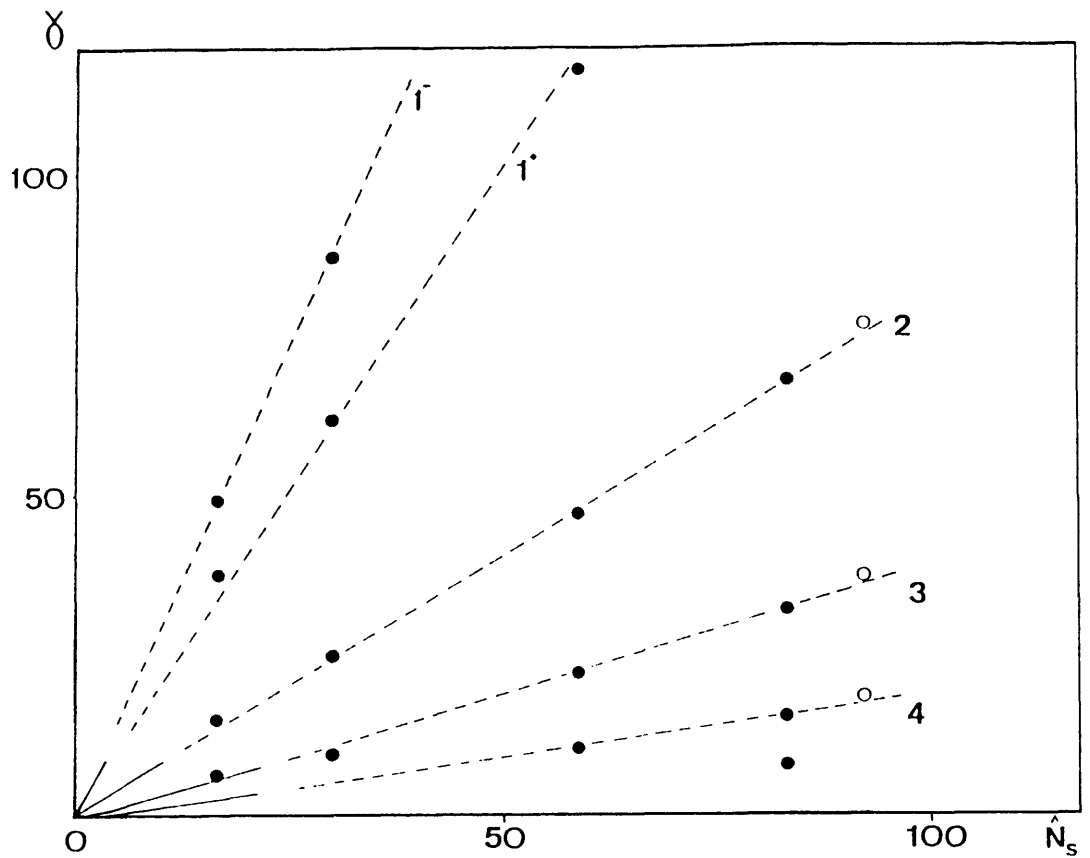

Figure 8.5 Dimensionless plot of the positions of the diamagnetic resonances observed in the parallel field orientation against total subband occupancies. The full lines near the origin are the "universal curves" of Reisenger and Koch [195] deduced for other material systems.

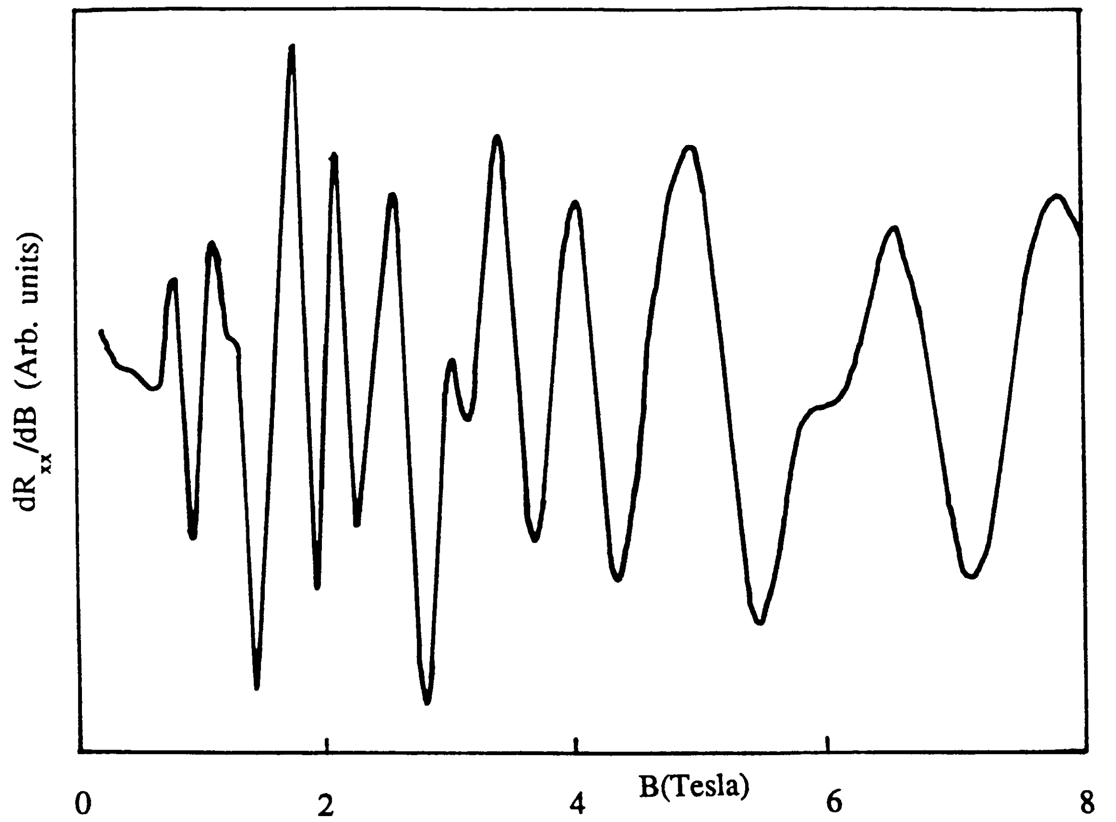

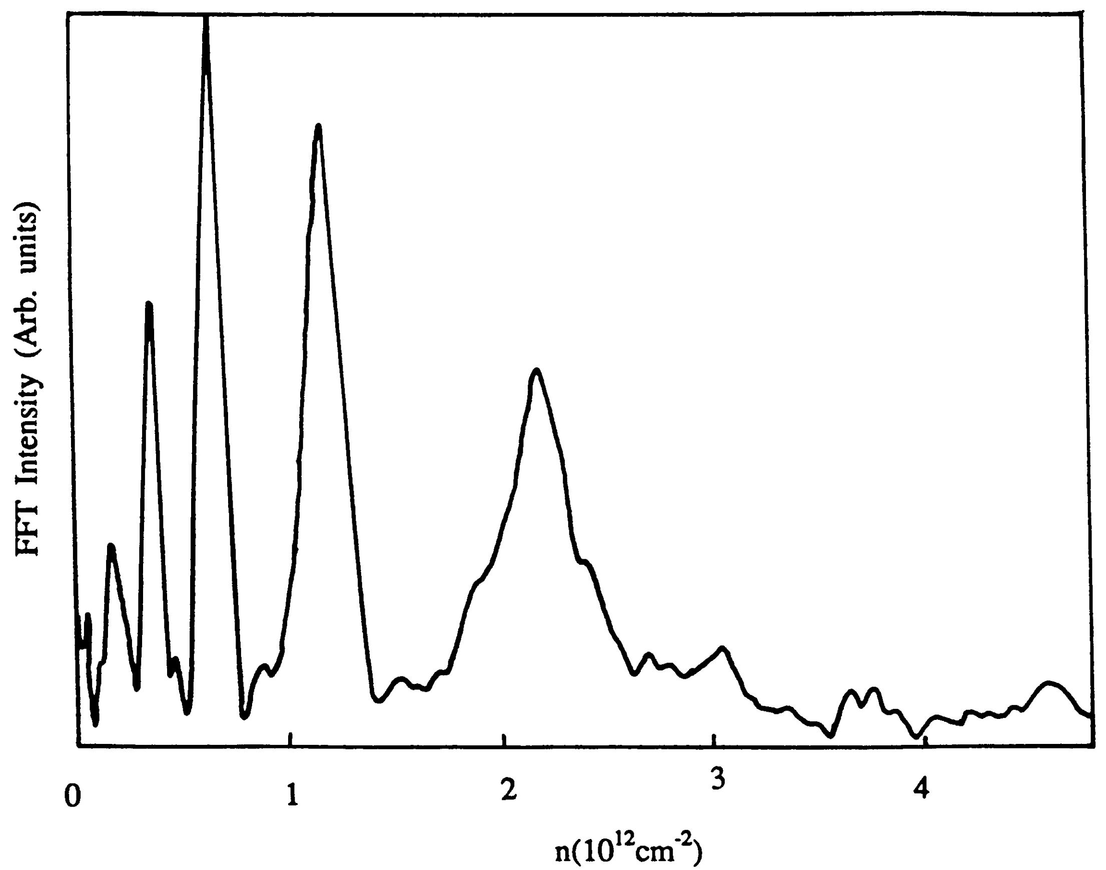

Figure 8.6 perpendicular field Shubnikov-de Haas oscillations and Fourier transform for a heavily delta doped (~5x$10^{12}cm^{-2}$) InAs sample showing the occupation of 5 subbands.

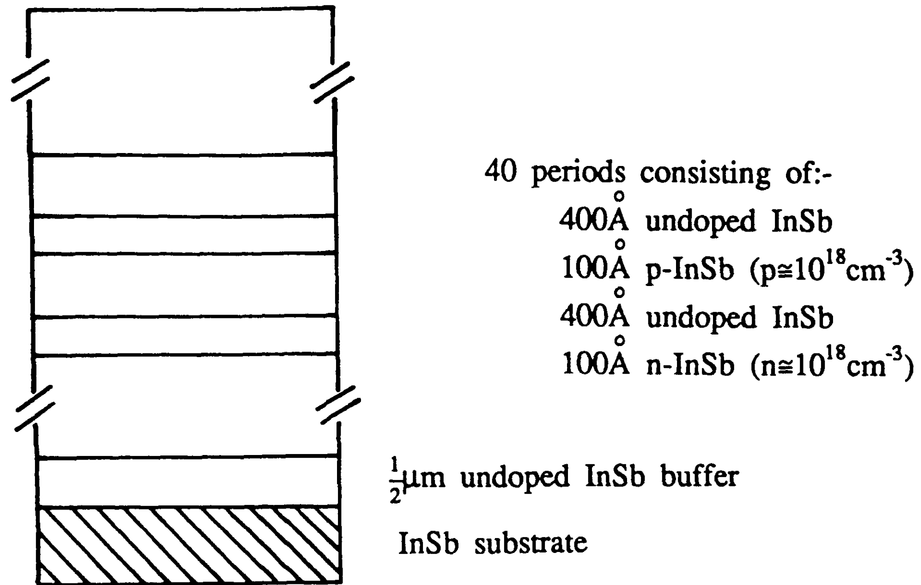

Figure 8.7 A typical n-i-p-i structure.

CHAPTER 9 SUMMARY AND CONCLUSIONS

The work presented in this thesis were oriented towards the growth and electrical characterisation of narrow gap III-V semiconductors. Because of their small bandgaps, InAs, InSb and In(AsSb) are especially useful for device applications for operation in the infrared region of the electromagnetic spectrum. However, before device structures can be made it is essential that the growth and electrical properties of these materials be studied and understood.

During the MBE growth of InSb, the observation of RHEED intensity oscillations proved to be extremely useful in optimising the growth conditions. It was shown that these oscillations were critically dependent on the group V/group III flux ratio and the substrate temperature. RHEED oscillations were easily observed at a flux ratio close to unity and a temperature of around 370°C. This technique also allowed for the *in-situ* calibration of beam fluxes and growth rate bringing it on par with GaAs.

The initial stages of MBE growth of InSb on GaAs(001) was studied by RHEED and indicated a Volmer-Weber growth mode characterised by islands as opposed to a Stranski-Krastanov growth mode. The InSb islands tend to have flat tops and sloping sides with facets predominantly parallel to the $(\bar{1}11)$, $(1\bar{1}1)$, (113 and $(\bar{1}\bar{1}3)$ planes. After the deposition of 36 monolayers of InSb the islands were beginning to coalesce. TEM however, showed that the substrate is completely covered after the deposition of about 300 MLs. These results suggested that for opto-electronic device applications based on InSb/GaAs, an InSb buffer layer of at least 1000Å must be grown on the substrate.

By using optimum growth conditions it was demonstrated that InSb and InAs epilayers with good surface morphology can be grown both homoepitaxially and heteroepitaxially on GaAs substrates by MBE. The quality of the $InAs_xSb_{1-x}$ surfaces were found to be dependent on on the composition when a substrate temperature of 370°C was used. This however, represented the first attempt at growing these ternary alloys and as such the growth conditions were not optimised.

Although Hall measurements indicated n-type conductivity for undoped homoepitaxial InSb layers, removal of the substrate suggest the epilayer to be high quality p-type material. It was shown that the measured n-type

conductivity arises from a quasi-2DEG at the interface between the epilayer and the substrate resulting from the pregrowth ion cleaning procedure for InSb substrates. Heteroepitaxial InSb layers on the other hand, were n-type even for layers ≤ 1 μm in thickness. The sharp drop in the 77K mobility for the 1μm thick InSb layers on GaAs was therefore attributed to the dominance of dislocation scattering.

An investigation of silicon as a possible n-type donor in InSb was carried out by growing slab-doped epilayers on GaAs and using Hall and Shubnikov-de Haas measurements to determine the electrical properties. These results indicated that Si behaves amphoterically at high growth temperatures. However, by controlling the growth conditions silicon in InSb can produce electron concentrations up to $3 \times 10^{18} cm^{-3}$ without autocompensation. The effect on the electrical properties of the interface between InSb and GaAs (lattice mismatch of 14%) has also been studied by introducing the doping slabs at varying distances between the interface and the epilayer surface. When the slab is situated at the interface the mobility was found to degrade by more than a factor of 2 whereas deviations from the bulk mobility were small when the slabs were located at distances ≥ 0.3μm from the interface and low growth temperatures were used. The results of Shubnikov-de Haas experiments on these slab-doped samples showed quasi-3D behaviour at high magnetic fields. At low magnetic fields a series of peaks not periodic in reciprocal field were observed with B parallel to the plane of the slab. These were interpreted as arising from the diamagnetic depopulation of the large number of subbands occupied as a result of the considerable thickness of the slabs. P-type doping with hole concentration of $2 \times 10^{19} cm^{-3}$ and a mobility corresponding to the bulk value was achieved using beryllium.

The surface morphology of InAs epilayers grown on GaAs was found to be dependent on the substrate temperature for the flux ratios used. Nevertheless, smooth and mirror shiny surfaces were obtained on InAs layers grown at a temperature of $475^{o}C$ under As-stabilised conditions. The apparent 300K and 77K mobilities of undoped InAs/GaAs layers were found to decrease with decreasing layer thickness. This was shown to be due to the increasing dominance of a low mobility electron accumulation layer as the epilayer thickness was reduced. The mobility for the bulk of the sample was found to be of the order 2.5×10^{5} $cm^{2}V^{-1}s^{-1}$ as deduced from cyclotron resonance linewidths.

The electrical properties of the ternary alloy $InAs_xSb_{1-x}$ were investigated for the complete range of composition 0<x<1. These samples were grown on GaAs substrates at 370°C and represented the first attempt at growing ternary group $IIIV_AV_B$ semiconductor alloys. The results of Hall measurements indicated rather high carrier concentrations and low mobilities. A possible reason, apart from growth optimisation, for the low mobility in these layers could be alloy ordering effects which have been reported in TEM diffractions studies carried out on these layers. In terms of future experiments on this system, it is hoped that the growth conditions can be optimised to improve the electrical properties. Following on this, the growth of strained layer superlattices involving InAsSb could be attempted with the aim of reducing the effective bandgap such that the operating wavelength can be extended to 10μm.

In conclusion therefore, the work presented in this thesis has demonstrated that MBE can produce narrow gap III-V semiconductors with extremely high electrical quality. As a result of the study on Si doping in InSb, devices can now be fabricated to operate at wavelengths in the infrared region.

The majority of the work presented in this thesis has been reported in a number of publications. A list of the relevant publications is given in Appendix A.

APPENDIX A LIST OF PUBLICATIONS

"RHEED Intensity Oscillations observed during MBE Growth of InSb(001)", R Droopad, R L Williams, S D Parker *Semicond Sci Tech* **4** (1989) 111

"Magneto-optical and Transport Studies of Ultrahigh Mobility Films of InAs grown by Molecular Beam Epitaxy on GaAs", S N Holmes, R A Stradling, P D Wang, R Droopad, S D Parker, R L Williams *Semicond Sci Tech* **4** (1989) 303

"Observation and Control of the Amphoteric Behaviour of Si-doped InSb Grown on GaAs by MBE", S D Parker, R L Williams, R Droopad, R A Stradling, K W J Barnham, S N Holmes, J Laverty, C C Phillips, E Skuras, R Thomas, X.Zhang, A Staton-Bevan, D W Pashley *Semicond Sci Tech* **4** (1989) 663

"Parallel and Perpendicular Field Magnetotransport Studies of MBE Grown GaAs Doping Superlattices and Slab Doped InSb formed by Selective Doping with Silicon", R Droopad, S D Parker, E Skuras, R L Williams, R A Stradling, R B Beall, J J Harris *Proc Int Conf on High Magnetic Fields Applied to Semiconductor Physics* (Wurzburg) 1988

"MBE Growth and Quantum Transport Measurements of Spike Doped InSb and InAs" R L Williams, E Skuras, R A Stradling, R Droopad, S N Holmes, S D Parker *Proc Int Conf on Narrow Gap Semiconductors* (1989)

"Nipi Superlattices in InSb: an Alternative Approach to 10μm Detector Fabrication", C C Phillips, C Hodge, R Thomas, S D Parker, R L Williams, R Droopad *Proc Int Conf on Narrow Gap Semiconductors* (1989)

"A TEM and RHEED Study of the Initial Stages of Heteroepitaxial Growth of InSb on GaAs", X Zhang, A E Staton-Bevan, D W Pashley, S D Parker, R Droopad, R L Williams, R C Newman *J Appl Physics* - to be published

ACKNOWLEDGEMENT

I would like to thank my supervisor, Prof. R. A. Stradling for his encouragement and supervision throughout the past three years. I am especially grateful to Steve Parker for his guidance and the knowledge of MBE which he is always willing to share. I would also like to thank Prof. B. A. Joyce for some stimulating discussions on MBE growth and RHEED, Robin Williams for the many discussions on quantum transport, Dr. Yuen for useful discussions and S.Nathan for various technical assistance.

I would like to mention my wife and daughter whose love and support throughout this past three years are very much appreciated.

Finally, I would like to thank the Association of Commonwealth Universities for the provision of a Commonwealth Academic Staff Scholarship.

REFERENCES

1 A M Jean-Louis, C Hanlon *Phys Status Solidi* **34** (1969) 329

2 K Chow, J P Rode, D H Seib, J D Blackwell *IEEE Trans Electron Devices* **ED-29** (1982) 3

3 P G Kornreich, L Walsh, J Flattery, S Isa *Solid State Electronics* **29** (1986) 421

4 R G van Welzenis, B K Ridley *Solid State Electronics* **27** (1984) 113

5 W A Harrison *J Vac Sci Tech* **A1** (1983) 1672

6 A Sher, A B Chen, W E Spicer, C K Shik *J Vac Sci Tech* **A3** (1985) 105

7 K Mohammed, F Capasso, R A Logan, J P van der Ziel, A L Hutchinson *Electron Lett* **22** (1986) 215

8 Z L Zyskind, A K Srivastava, J C Winter, M A Pollack, J W Sulhoff *J Appl Phys* **61** (1987) 2898

9 E O Kane *J Phys Chem Solids* **1** (1957) 249

10 J R Chelikowsky, M L Cohen *Phys Rev B* **14** (1976) 550

11 These parameters were taken from Landolt-Börnstein *New Series III/22a* Ed by O Madulung (Springer-Verlag) 1987

12 G C Osbourn *J Vac Sci Tech* **B2** (1984) 176

13 G H Döhler *Phys Stat Sol* **53** (1972) 79

14 K G Günther *Z Naturfoch* **3a** (1958) 1081

15 J E Davey, T Pankey *J Appl Phys* **39** (1968) 1941

16 J R Arthur Jr *J Appl Phys* **39** (1968) 4032

17 B A Joyce *Rep Prog Phys* **37** (1974) 363

18 A Y Cho *J Vac Sci Tech* **8** (1971) S31

19 A Y Cho, H Casey Jr *Appl Phys Lett* **35** (1974) 288

20 A Y Cho *Jpn J Appl Phys* **16** Suppl 16-1 (1977) 435

21 J H Neave, B A Joyce *J Cryst Growth* **43** (1978) 204

22 J H Neave, B A Joyce *J Cryst Growth* **44** (1978) 387

23 C E C Wood, J Woodcock, J J Harris *Inst Phys Conf Ser* **45** (1978) 28

24 T Murotani, T Shimanoe, S Mutsui *J Cryst Growth* **45** (1978) 802

25 G Wicks, W I Wang, C E C Wood, L F Eastman, L Rathbun *J Appl Phys* **52** (1981) 5792

26 G M Metze, A R Calawa *Appl Phys Lett* **42** (1983) 820

27 J J Harris, R B Beall, J B Clegg, C T Foxon, S J Battersby, D E Laklison, G Duggan, C M Hellon *Proc 5th Int Conf on MBE* Sapporo (1988) 257

28 For Example J W Christian in *The Theory of Phase Transformation in Metals and Alloys* (Pergamon, Oxford) 1975

29 J A Venables *Thin solid Films* **50** (1978) 378

30 J D Weekes, G H Gilmer *Adv Chem Phys* **40** (1979) 157
31 F C Frank, J H van der Merle *Proc Roy Soc London* **A198** (1949) 205
32 W K Burton, N Cabrera, F C Frank *Proc Royal Soc London* **A243** (1951) 299
33 A Madhukar *Surf Sci* **132** (1983) 344
34 R Heckingbottom, G W Davies, K A Prior *Surf Sci* **132** (1983) 375
35 J Singh, K K Bajaj *J Vac Sci Tech* **B2** (1984) 576
36 J Singh, K K Bajaj *J Vac Sci Tech* **B3** (1985) 520
37 S V Ghaisas, A Madhukar *J Vac Sci Tech* **B3** (1985) 540
38 S V Ghaisas, A Madhukar *Appl Phys Lett* **47** (1985) 247
39 S Clarke, D D Vvedensky *J Appl Phys* **63** (1988) 2272
40 C T Foxon, B A Joyce *Surf Sci* **50** (1975) 434
41 C T Foxon, B A Joyce *Surf Sci* **64** 1977) 293
42 W A Jesser, J W Matthews *Phil Mag* **15** (1967) 1097
43 R F C Farrow, D S Robertson, G M Williams, A G Cullis, C R Jones, I M Young, P N J Dennis *J Crystal Growth* **54** (1981) 507
44 Y G Chai, R Chow *J Appl Phys* **53** (1982) 1229
45 Y Koide, S Zaima, N Ohshima, Y Yasuda *Jpn J Appl Phys* **28** (1989) L690
46 X Zhang, A E Staton-Bevan, D W Pashley, S D Parker, R Droopad, R L Williams, R C Newmann *J Appl Phys* To be published
47 M N Charesse, B Bartenlian, R Bisaro, J Chezelas, J P Hirtz *5th Euro Workshop on MBE*, Grainau, March 1989
48 S Baba, H Horita, A Kinbara *J Appl Phys* **49** (1978) 3632
49 M Yano, T Takase, M Kimata *Phys Stat Sol* **54** (1979) 707
50 M Yano, T Takase, M Kimata *Jpn J Appl Phys* **18** (1979) 387
51 K Oe, S Ando, K Sugiyama *Jpn J Appl Phys* **19** (1980) L417
52 A J Noreika, M H Francombe, C E C Wood *J Appl Phys* **52** (1981) 7416
53 A J Noreika, J Greggi Jr, W J Takei, M H Francombe *J Vac Sci Tech* **A1** (1983) 558
54 A J Noreika, W J Takei, M H Francombe, C E C Wood *Collected Papers of MBE-CST-2*, Tokyo (1982) 161
55 J I Chyi, S Kalem, N S Kumar, C W Litton, H Morkoc *Appl Phys Lett* **53** (1988) 1092
56 J L Davis P E Thompson *Appl Phys Lett* **54** (1989) 2235
57 K Sugiyama *J Cryst Growth* **60** (1982) 450
58 S Wood, J Greggi Jr, R F C Farrow, W J Takei, F A Shirland, A J Noreika *J Appl Phys* **55** (1984) 4225
59 G M Williams, C R Whitehouse, A G Cullis, N G Chew, G W Blackmore *Appl Phys Lett* **53** (1988) 1847
60 J I Chyi, D Biswas, S V Iyer, N S Kumar, H Morkoc, R Bean, K Zanio,

H Y Lee, H Chen *Appl Phys Lett* **54** (1989) 1016
61 N Godinho, A Brunchweiler *Solid State Electronics* **13** (1970) 47
62 K Tateishi, N Naganuma, K Taakahashi *Jpn J Appl Phys* **15** (1976) 785
63 M Yano, M Nogami, Y Matsushima, M Kimata *Jpn J Appl Phys* **16** (1977) 2131
64 B T Meggit, E H C Parker, R M King *Appl Phys Lett* **33** (1978) 528
65 C Chang, C M Serrano, L L Chang, L Esaki *J Vac Sci Tech* **17** (1980) 603
66 C Chang, C M Serrano, L L Chang, L Esaki *Appl Phys Lett* **37** (1980) 538
67 W J Schaffer, M D Lind, S P Kowalczyk, R W Grant *J Vac Sci Tech* **B1** (1983) 688
68 S M Newstead, R A A Kubiak, E H C Parker *Proc 4th Int Conf on MBE* York (1986) 49
69 F Houzay, C Guille, J M Moison, P Henoc, F Barthe *Proc 4th Int Conf on MBE* York (1986) 67
70 R A A Kubiak, E H C Parker, S M Newstead, J J Harris *Appl Phys Lett* **A35** (1984) 61
71 J D Grange, E H C Parker, R M King *J Phys D: Appl Phys* **12** (1979) 1601
72 H H Weider *Appl Phys Lett* **25** (1974) 206
73 S N Holmes, R A Stradling, P D Wang, R Droopad, S D Parker, R L Williams *Semicond Sci Tech* **4** (1989) 303
74 S Kalem, J I Chyi, H Morkoc, R Bean, K Zanio *Appl Phys Lett* **53** (1988) 1647
75 S Kalem, J I Chyi, C W Litton, H Morkoc, S C Kan, A Yariv *Appl Phys Lett* **53** (1988) 562
76 T H Chiu, W T Tsang *J Appl Phys* **57** (1985) 4532
77 G S Lee, Y F Lin, S M Bedair, W D Laidig *Appl Phys Lett* **47** (1985) 1219
78 L R Dawson *J Vac Sci Tech* **B4** (1986) 598
79 J I Chyi, S Kalem, N S Kumar, C W Litton, H Morkoc *Appl Phys Lett* **53** (1988) 1092
80 T H Chiu, W T Tsang, J A Ditzenberger *J Vac Sci Tech* **B4** (1986) 600
81 M Y Yen, B F Levine, C G Bethea, K K Choi, A Y Cho *Appl Phys Lett* **50** (1987) 927
82 M Y Yen, R People, K W Weiht, A Y Cho *Appl Phys Lett* **52** (1988) 489
83 M Y Yen *J Appl Phys* **64** (1988) 3306
84 C G Bethea, M Y Yen, B F Levine, K K Choi, A Y Cho *Appl Phys Lett* **51** (1987) 1431
85 C G Bethea, B F Levine, M Y Yen, A Y Cho *Appl Phys Lett* **53** (1988) 291
86 S R Kurtz, L R Dawson, T E Zipperian, S R Lee *Appl Phys Lett* **52** (1988) 1581
87 S R Kurtz, G C Osbourn, R M Biefeld, L R Dawson, H J Stein *Appl Phys Lett* **52** (1988) 831
88 C Davisson, L H Germer *Phys Rev* **30** (1927) 705

89 L deBroglie *Phil Mag* **47** (1924) 446
90 S Nishikawa, S Kikuchi *Proc Imp Acad Japan* **4** (1928) 475
91 M P Seah, W A Dench *Surf and Interface Analysis* **1**(1) (1979) 2
92 E Bauer in *Techniques of Metal Research* ed by R F Bunshah **2**(2) (Interscience NY) 1961
93 M Henzler in *Dynamical Phenomena at Surface, Interfaces and Superlattices* eds F Nizolli, K -H Reider, R F Willis (Springer-Verlag, 1985) 14
94 G J Russell *Prog Cryst Growth and Charact* **5** (1982) 291
95 L J Giling, W J P van Enckevort *Surf Sci* **161** (1985) 567
96 L Daweritz *Surf Sci* **160** (1985) 171-188
97 D J Chadi *Phys Rev Letters* **43** (1979) 43
98 A Y Cho *J Appl Phys* **47** (1976) 2841
99 A Y Cho *J Appl Phys* **42** (1971) 2074
100 A Kahn *J Vac Sci Tech* **A1** (1983) 684
101 A Kahn *Surf Sci Reports* **3** (1983) 193
102 See for example P K Larsen, J F van der Veen, A Mazur, J Pollmann, J H Neave, B A Joyce *Phys Rev* **B26** (1982) 3227
103 E A Woods *J Appl Phys* **35** (1964) 1306
104 B A Joyce, J H Neave, P J Dobson, P K Larsen *Phys Rev* **B29** (1984) 814
105 A Y Cho, J R Arthur *Prog Solid State Chem* (1975) 157
106 L L Chang, L Esaki, W E Howard, R Ludeke, G Schul *J Vac Sci Tech* **10** (1973) 655
107 S Holloway, J L Beeby *J Phys C* **11** (1978) L247
108 K Ploog, A Fisher *Appl Phys* **13** (1977) 111
109 I Hernández-Calderón, H Höchst *Phys Rev* **B27** (1983) 4961
110 P J Dobson, J H Neave, B A Joyce *Surf Sci* **119** (1982) L339
111 J M Van Hove, P I Cohen *J Vac Sci Tech* **20** (1982) 726
112 J M Van Hove, P I Cohen, C S Lent *J Vac Sci Tech* **A1** (1983) 546
113 P K Larsen, J H Neave, B A Joyce *J Phys C* **14** (1981) 167
114 J H Neave, B A Joyce, P J Dobson, N Norton *Appl Phys* **A31** (1983) 1
115 J M Van Hove, C S Lent, P R Pukite, P I Cohen *J Vac Sci Tech* **B1** (1981) 741
116 J J Harris, B A Joyce, P J Dobson *Surf Sci* **103** (1981) L90
117 R W Vook, Y Namba *Appl Surf Sci* **11/12** (1982) 400
118 K D Gronwald, M Henzler *Surf Sci* **117** (1982) 180
119 V Bostanov, R Roussinova, E Budevski *J Electrochem Soc* **119** (1972) 1346
120 J D Weekes, G H Gilmer *Adv Chem Phys* **40** (1979) 157
121 B A Joyce, P J Dobson, P K Larsen, B Bolger *Surf Sci* **168** (1986) 423
122 T Sakamoto, N J Kawai, T Nakagawa, K Ohta, T Kogima *Appl Phys Letts* **47** (1985) 617

123 T Kawamura, T Sakamoto, K Ohta *Surf Sci* **171** (1986) L409
124 C S Lent, P I Cohen *Surf Sci* **139** (1984) 121
125 P I Cohen, P R Pukite, J M Van Hove, C S Lent *J Vac Sci Tech* **A4** (1986) 1251
126 P A Makysm, J L Beeby *Surf Sci* **110** (1981) 423
127 B A Joyce, P J Dobson, J H Neave, J Zhang *Surf Sci* **178** (1986) 110
128 P K Larsen, P J Dobson, J H Neave, B A Joyce, B Bolger, J Zhang *Surf Sci* **169** (1986) 176
129 J Zhang, J H Neave, P J Dobson, B A Joyce *Appl Phys* **A42** (1987) 317
130 B A Joyce, J Zhang, J H Neave, P J Dobson *Appl Phys* **A45** (1988) 255
131 B F Lewis, R Fernandez, A Madhukar, F J Grunthaner *J Vac Sci Tech* **B4** (1986) 560
132 G J Davies, D Williams in *The Technology and Physics of Molecular Beam Epitaxy* Ed E H C Parker (Plenum) 1985
133 C E C Wood, B A Joyce *J Appl Phys* **49** (1978) 4854
134 C E C Wood, D Desimone, K Singer, G W Wicks *J Appl Phys* **53** (1982) 4230
135 A Y Cho, K Y Cheng *Appl Phys Lett* **38** (1981) 796
136 K Y Cheng, A Y Cho *Appl Phys Lett* **39** (1981) 607
137 J C M Hwang, T M Brennan, A Y Cho *J Electrochem Soc* **130** (1983) 493
138 J W Robinson, M Ilegems *Rev Sci Instrum* **49** (1978) 205
139 W T Tsang *J Crystal Growth* **56** (1982) 464
140 M Ilegems, R Dingle *Int Phys Conf Ser* **24** (1975) 1
141 C E C Wood, J Woodcock, J J Harris *Int Phys Conf Ser* **45** (1979) 28
142 J H Neave, P Blood, B A Joyce *Appl Phys Lett* **36** (1980) 311
143 R A Stall, C E C Wood, P D Kirchner, L F Eastman *Electron Lett* **16** (1980) 171
144 J D Grange in *The Technology and Physics of MBE* Ed E H C Parker (Plenum) 1985
145 H L Henneke *J Appl Phys* **36** (1965) 2967
146 F D Auret *J Electrochem Soc* **129**(12) (1982) 2752
147 R P Vasquez, B F Lewis, F J Grunthaner *J Vac Sci Tech* **B1**(3) (1983) 971
148 S Wood, J Greggi Jr, R F C Farrow, W J Takei, F A Shirland, A J Noreika *J Appl Phys* **55(12)** (1984) 4225
149 F D Auret *J Electrochem Soc* **131**(9) (1984) 2115
150 C R Whitehouse, M T Emeny, L Davies, G M Williams, T Martin *Proc 4th Int Conf on MBE* York (1986)
151 J M Van Hove, P I Cohen *J Vac Sci Tech* **29** (1982) 726
152 C E C Wood, C R Stanley, G W Wicks, M B Esi *J Appl Phys* **54** (1983) 546
153 G M Williams, C R Whitehouse, C F McConville, A G Cullis, T Ashley,

S J Courtney, C T Elliot *Appl Phys Lett* **53** (1988) 1189

154 S D Parker, R L Williams, R Droopad, R A Stradling, K W J Barnham, S N Holmes, J Laverty, C C Phillips, E Skuras, R Thomas, X Zhang, A Staton-Bevan, D W Pashley *Semicond Sci Tech* **4** (1989) 663

155 R Droopad, R L Williams, S D Parker *Semicond Sci Tech* **4** (1989) 111

156 Y Horikoshi, M Kawashima *Proc 5th Int Conf on MBE* Sapporo (1988)

157 C T Foxon *Private Communication*

158 J H Neave, P J Dobson, B A Joyce, J Zhang *Appl Phys Lett* **47** (1985) 100

159 S Clarke, D D Vvedensky *Surf Sci* **189/190** (1987) 1033

160 S Clarke, D D Vvedensky *Phys Rev* **B36** (1987) 9312

161 J F van der Veen, P K Larsen, J H Neave, B A Joyce *Solid State Comm* **49** (1984) 659

162 J W Matthews, A E Blakeslee *J Crystal Growth* **28** (1974) 118

163 B A Joyce, J H Neave, P E Watts *Surf Sci* **15** (1969) 1

164 D A Anderson, N Apsley *Semicond Sci Tech* **1** (1986) 187

165 R A Smith in *Semiconductors* (Cambridge) 1978

166 W Shockley, J Bardeen *Phys Rev* **80** (1950) 72

167 D L Rode *Phys Rev* **B2** (1970) 1012

168 H Ehrenreich *J Phys Chem Solids* **8** (1959) 130

169 G E Stillman, C M Wolfe *Thin Solid Films* **31** (1976) 69

170 W Walukiewicz, L Lagowski, L Jastrzebski, M Lichtensteiger, H C Gatos *J Appl Phys* **50** (1979) 899

171 W Walukiewicz, L Lagowski, H C Gatos *J Appl Phys* **53** (1982) 769

172 W Walukiewicz, L Lagowski, L Jastrzebski, P Rava, M Lichtensteiger, C H Gatos, H C Gatos *J Appl Phys* **51** (1980) 2659

173 E Conwell, V F Weisskoff *Phys Rev* **77** (1950) 388

174 H Brooks in Advances in *Electronics and Electron Physics* ed L Martin *VII* (Academic Press) 85

175 W Zawadski, W Szymanska *J Phys Chem Solids* **32** (1971) 1151

176 W Zawadski *Adv Phys* **23** (1974) 435

177 J Kolodziejczak *Acta Physica Polonica* **20** (1961) 289

178 D L Dexter, F Seitz *Phys Rev* **86** (1952) 964

179 W T Read *Phil Mag* **45** (1954) 775

180 W T Read *Phil Mag* **46** (1954) 111

181 See for example J Tietjen, L R Weisberg *Appl Phys Lett* **7** (1965) 261

182 J van der Pauw *Philips Res Repts* **13** (1958) 1

183 H H Weider in *Laboratory Notes on Electrical and Galvanomagnetic Measurements* (Elsevier) 1979

184 T Ashley *Private communication*

185 W T Yuen, W K Liu, S N Holmes, R A Stradling *Semicond Sci Tech* **4** (1989) 819

186 C F McConville, C R Whitehouse, G M Williams, A G Cullis, T Ashley, M S Skolnick, G T Brown, S J Courtney *J Cryst Growth* **95** (1989) 228

187 W Hanus, M Oszwaldowski *Thin Solid Films* **61** (1979) 235

188 S Patel *MSc Project* (1989) Imperial College

189 K Ploog *J Crystal Growth* **81** (1987) 304

190 V M Glazov, E B Smirnova *Sov Phys Semicond* **17** (1983) 1177

191 J Maguire, R Murray, R C Newman *Appl Phys Lett* To be published

192 G A Antcliffe, R A Stradling *Phys Lett* **29** (1966) 119

193 J Laverty MSc project (1988) Imperial College

194 R F Broom *Proc Roy Soc* **71** (1958) 470

195 H Reisenger, F Koch *Surf Sci* **170** (1986) 397

196 S L Wright, S Tiwari, T N Jackson, H Baratte *Appl Phys Lett* **49** (1986) 1545

197 A Rogalski, K Jozwikowski *Infrared Phys* **29** (1989) 35

198 T Y Seong, A G Norman, G R Booker, R Droopad, S D Parker, R L Williams, R A Stradling *Proc Mat Res Soc Symp* (1989)

199 E F Shubert, A Fisher, K Ploog *IEEE Trans Devices* **ED-33** (1986) 625

200 E F Shubert, K Ploog *Jpn J Appl Phys* **24** (1985) L608

201 E F Shubert, J E Cunningham, W T Tsang *Solid State Comm* **63** (1987) 591

202 J Maguire, R Murray, R C Newman, R B Beall, J J Harris *Appl Phys Lett* **50** (1987) 516

203 A Zrenner, F Koch, R L Williams, R A Stradling, K Ploog, G Weimann *Semicond Sci Tech* **3** (1988) 1203

204 C E C Wood, G Metze, J Berry, L F Eastman *J Appl Phys* **51** (1980) 383

205 G H Döhler *Surf Sci* **73** (1978) 97

206 A Zrenner, H Resinger, F Koch, K Ploog *Proc Int Conf on Physics of Semiconductors* San Francisco 1984 Eds J D Chadi, W A Harrison (Springer Berlin) 325

207 K Ploog, A Fisher, H Künzel *J Electrochem Soc* **128** (1981) 400

208 C C Phillips, C Hodge, R Thomas, S D Parker, R L Williams, R Droopad *Proc Int Conf on Narrow Gap Semiconductors (Semicond Sci Tech)* 1990